Monte Carlo simulations of radiative transport in the atmosphere and ocean

Cand.scient. thesis

Karl Idar Gjerstad

Department of Physics
University of Bergen

October 2001

Contents

Preface

From early childhood I have been fascinated by the occurrence of phenomena in nature and the topics I found most interesting happened to be connected with physics. It was therefore easy for me to choose which way to go when I grew up. When I started studying, I found optics to be one of the most exciting issues and therefore I wanted to write the Cand. Scient. thesis within this topic.

The work of this thesis has been carried out at the Department of Physics at the University of Bergen. During these years I have received valuable help and support that have been of great importance. First, I would like to express my thankfulness to my supervisor Professor Jakob J. Stamnes for guiding me through the whole process. This could never been done without his knowledge and encouragement. I would also like to thank Øyvind Frette and Jon Kåre Lotsberg for helping me out when I started to write the Monte Carlo program. Some of the subroutines used in our program are even taken from Lotsberg's Cand. Scient. thesis. During the work I have cooperated very closely with Børge Hamre who has provided me with results from the DISORT routine and with ideas for my own Monte Carlo routine. This cooperation has been very fruitful and of great benefit to me. I also wish to give credit to Knut Stamnes and Banghua Yan for contributing with creative ideas and feedback on my work.

Finally I would like to thank friends and family for their moral support. Especially I want to thank my parents, Kari and Harald Gjerstad, for stimulating my curiosity when I grew up and encouraging me through the studies.

8th of October 2001, Karl Idar Gjerstad

Introduction

The topics of atmospheric and marine optics are of great interest for marine biology and oceanography. The primary production, which is the source of the food chain and all life in the ocean, depends on the amount of light at different depths. Light reflected back from the ocean provides the signal for the remote sensing of the ocean by satellites. Through remote sensing of coastal water it may be possible to predict invasions of toxic algae, which can cause disease and death among Norwegian fish farms. Absorption of light heat the water in the top layer, and the attenuation of light with depth gives an estimate of the planktonic activity.

In this thesis we model the transport of light in the atmosphere and ocean by using Monte Carlo simulations. The purpose of the thesis is to develop a model that gives a good description of the behavior of light in a three-dimensional coupled atmosphere-ocean system. It should work for situations in which other models fail to give a proper result. For instance the discrete ordinate method (DISORT) program [1] developed by K. Stamnes and co-workers and Hydrolight [2, 3] by C.D. Mobley are one-dimensional models that are based on the assumption of vertical stratification, both in the atmosphere and in the ocean. These models may not work well close to the shore in coastal water and fjords, where fish farms are located.

Chapter 1

Radiometry

When dealing with marine optics, we need a coordinate system in order to define the quantities of radiometry. In this thesis we have chosen to let the Cartesian z axis be normal to the sea surface, while the x axis and the y axis are orthogonal horizontal axes that are parallel to the sea level as shown in fig. 1.1.

In treatments of scattering and energy flow it is better to use a spherical coordinate system r, θ, ϕ, with the unit vector $\hat{\mathbf{e}}_r$ along the direction of propagation, and with $\hat{\mathbf{e}}_\theta$ and $\hat{\mathbf{e}}_\phi$ being perpendicular to the direction of propagation

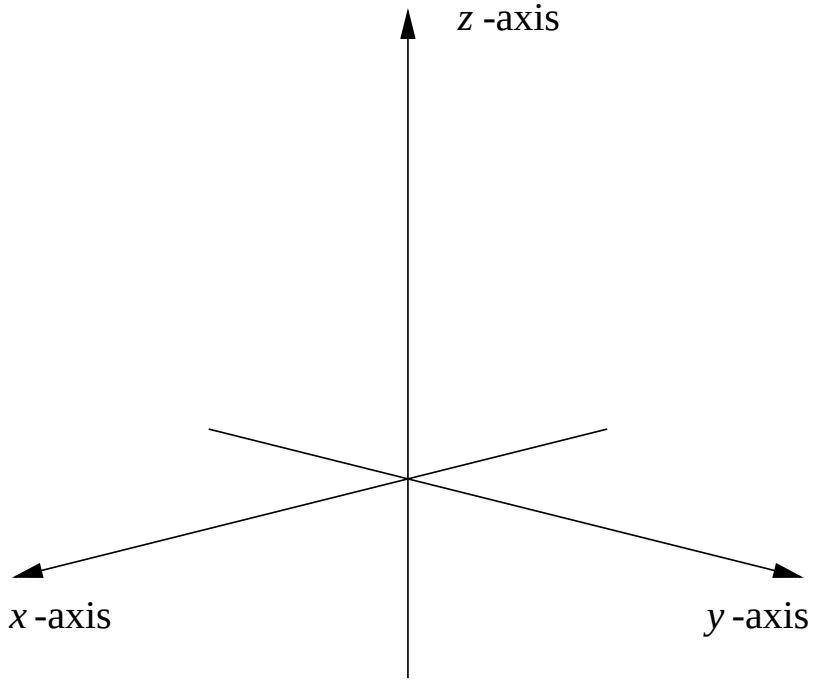

Figure 1.1: Orientation of a Cartesian coordinate system. The altitude is along the z axis, while the xy plane spans the sea surface.

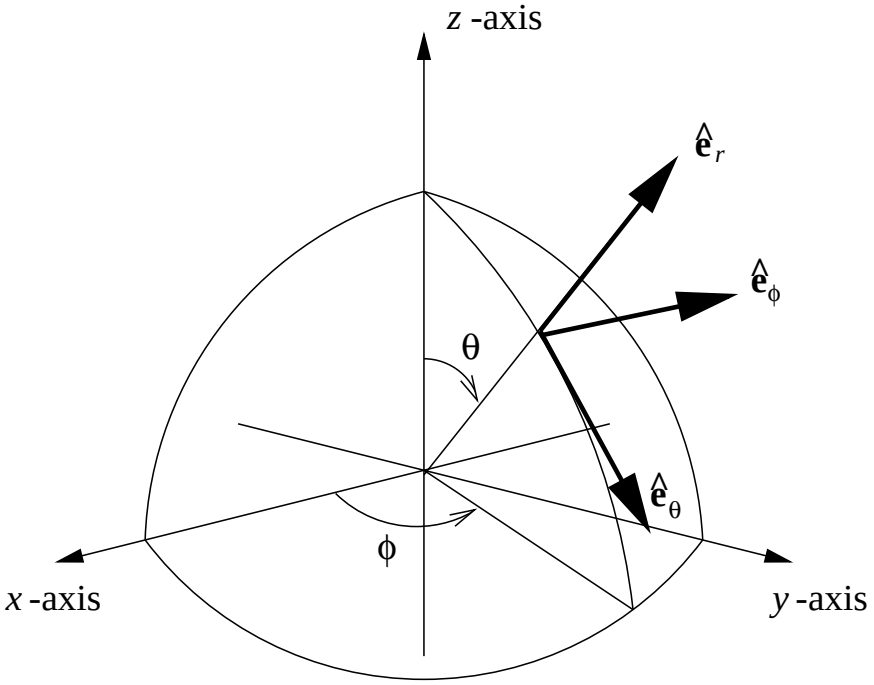

Figure 1.2: Spherical unit vectors $\hat{\mathbf{e}}_r$, $\hat{\mathbf{e}}_\theta$, and $\hat{\mathbf{e}}_\phi$ in the Cartesian coordinate system.

and to each other. In this system θ will be the angle between the direction of propagation and the z axis. Thus, when $0 < \theta < \pi/2$ and $\pi/2 < \theta < \pi$ light is propagating upwards and downwards, respectively. The angle ϕ is the azimuth angle, see fig. 1.2.

1.1 Radiometric quantities

The fundamental quantity in radiometry is the *spectral radiant flux* $\Phi(\lambda)$, also referred to as *the spectral radiant power P(λ)* by Spinrad et al. [4]. In the following we will stick to the term *flux*. Flux is energy per unit of time crossing a given surface and is expressed in Watts $[W]$. For simplicity we consider each wavelength separately so that we can treat light as if it were monochromatic ($\Phi(\lambda) = \Phi$). In radiometry, which is based on incoherent geometrical optics, it suffices to consider the particle nature of light. Thus we view light of wavelength λ as a stream of photons each possessing an energy hc/λ, where h is Planck's constant and c is the speed of light. When a surface is exposed to N photons per second, the *radiant flux* is

$$\Phi = \frac{hc}{\lambda} N. \tag{1.1}$$

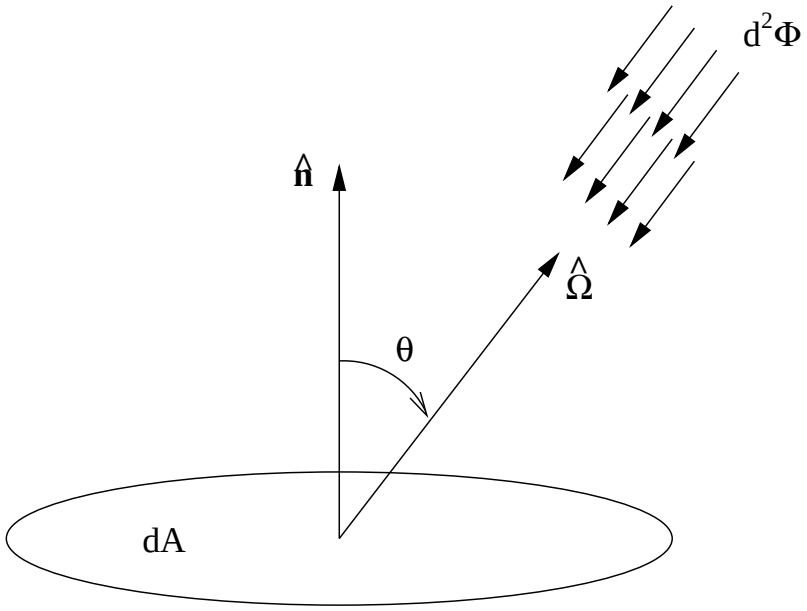

Figure 1.3: The radiance is defined by the ratio of the incoming flux $d^2\Phi$ in direction $\hat{\mathbf{\Omega}}$ to the product of the area dA and cosine of the angle of incidence θ.

The *radiant intensity* is the radiant flux per unit solid angle. In a given direction $\hat{\mathbf{\Omega}}$ with a surrounding solid angle element $d\omega$ the radiant intensity is

$$I(\hat{\mathbf{\Omega}}) = \frac{d\Phi(\hat{\mathbf{\Omega}})}{d\omega}. \tag{1.2}$$

The intensity is measured in $[Wsr^{-1}]$. The *radiance* L is the incident radiant flux per unit solid angle per unit area normal to the direction of propagation. Thus, if a plane surface with area dA and normal vector $\hat{\mathbf{n}}$ is exposed to a flux in the direction $\hat{\mathbf{\Omega}}$, and $\cos\theta = \hat{\mathbf{n}} \cdot \hat{\mathbf{\Omega}}$, then (fig. 1.3)

$$L(\hat{\mathbf{\Omega}}) = \frac{d^2\Phi(\hat{\mathbf{\Omega}})}{dA\,\cos\theta\,d\omega}. \tag{1.3}$$

The unit for radiance is $[Wm^{-2}sr^{-1}]$. Most measurements involve angular integrals of the radiance distribution, such as the *irradiance* defined by

$$E = \int_{4\pi} L(\hat{\mathbf{\Omega}})\cos\theta\,d\omega. \tag{1.4}$$

Here the integration domain 4π indicates that the radiance L times $\cos\theta$ is integrated over all solid angles. The irradiance is the flux per unit area. Thus it can also be expressed as

$$E = \frac{d\Phi}{dA} \tag{1.5}$$

where dA is the area. For the special case in which the flux is constant over the surface, we get

$$E = \frac{\Phi}{A}. \tag{1.6}$$

If the surface dA emits radiation, instead of being exposed to it, this quantity is usually called the *exitance*.

In some parts of scientific literature the flux and the irradiance are both defined in the same way, by Eq. (1.4). Similarly, both the intensity and the radiance are defined by Eq. (1.3). In this thesis, however, we will stick to the definitions given in Eq. (1.1) - (1.4) and mostly use the terms irradiance and radiance.

In marine optics it is conventional to divide the irradiance into *downwelling* irradiance

$$E_d = \int_{\Omega_d} L(\hat{\mathbf{\Omega}}) \cos\theta \, d\omega = \int_0^{2\pi} d\phi \int_{\pi/2}^{\pi} L(\hat{\mathbf{\Omega}}) \cos\theta \sin\theta \, d\theta$$

and *upwelling* irradiance

$$E_u = \int_{\Omega_u} L(\hat{\mathbf{\Omega}}) \cos\theta \, d\omega = \int_0^{2\pi} d\phi \int_0^{\pi/2} L(\hat{\mathbf{\Omega}}) \cos\theta \sin\theta \, d\theta$$

where Ω_d and Ω_u refer to integration over the downward and upward hemisphere, respectively. It may also be useful to consider the *scalar* irradiances E_{0d} and E_{0u} defined by

$$E_{0d} = \int_{\Omega_d} L(\hat{\mathbf{\Omega}}) \, d\omega = \int_0^{2\pi} d\phi \int_{\pi/2}^{\pi} L(\hat{\mathbf{\Omega}}) \sin\theta \, d\theta$$

and

$$E_{0u} = \int_{\Omega_u} L(\hat{\mathbf{\Omega}}) \, d\omega = \int_0^{2\pi} d\phi \int_0^{\pi/2} L(\hat{\mathbf{\Omega}}) \sin\theta \, d\theta.$$

Note that the irradiance is the integral of the product of the radiance and the cosine of the angle of incidence θ, while the scalar irradiance is just the integrated radiance. All irradiances are expressed in $[Wm^{-2}]$.

1.1.1 Inherent optical properties

Inherent optical properties (IOPs) are properties of a medium that do not depend on the incident light field. In descriptions of light propagation, the coefficients of absorption, scattering, and attenuation are examples of important IOPs. Consider a parallel beam that illuminates a small volume dV of length ds with incident flux Φ^i. In the volume element dV, some photons are absorbed, and some

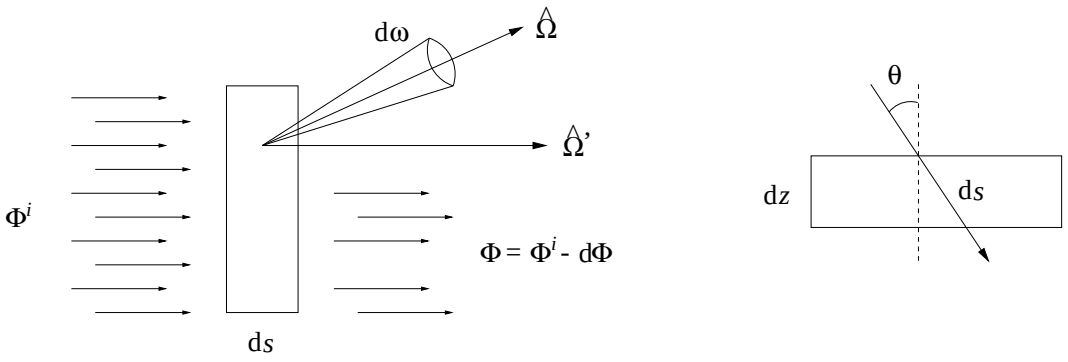

Figure 1.4: Left: Definition of the attenuation coefficient c. The optical thickness is defined as $\tau_s = cs$. Right: The figure shows the difference between the optical thickness ds and the optical depth dz. The relation between the quantities are $dz = ds\cos\theta$.

are scattered away from the incident direction $\hat{\mathbf{\Omega}}'$ into another direction $\hat{\mathbf{\Omega}}$, so that the transmitted flux leaving the volume is $\Phi = \Phi^i - d\Phi$. The attenuation coefficient c is defined by

$$c = -\frac{1}{ds}\frac{d\Phi}{\Phi^i}. \tag{1.7}$$

Thus, the attenuation is the ratio between the lost flux and the product of the incident flux and the thickness of the slab, see fig. 1.4. The minus sign in Eq. (1.7) indicates that we have attenuation and not amplification of the field. Solving Eq. (1.7) for Φ, we get

$$\Phi = \Phi^i e^{-cs}. \tag{1.8}$$

This result is known as the *extinction law*, where the term extinction means the same as attenuation. The dimensionless quantity $\tau_s = cs$ is called the *optical thickness*. It should not be confused with an other dimensionless quantity called the *optical depth*, which is defined as $\tau = cz = cs\cos\theta$, where z is the vertical depth of the medium and θ is the angle of incidence on the slab. The term optical depth is often used in marine optics. As indicated above, attenuation is the result of both absorption and scattering. Hence, the attenuated flux $d\Phi$ may be written $d\Phi = d\Phi^a + d\Phi^s$, where $d\Phi^a$ is attenuation due to absorption only and $d\Phi^s$ is attenuation due to scattering only. Then the absorption coefficient a and the scattering coefficient b can be defined in analogy with Eq. (1.7) as

$$a = -\frac{1}{ds}\frac{d\Phi^a}{\Phi^i} \tag{1.9}$$

and

$$b = -\frac{1}{ds}\frac{d\Phi^s}{\Phi^i}. \tag{1.10}$$

The unit for each of these coefficients is $[m^{-1}]$. The ratio

$$\omega_0 = \frac{b}{c}$$

is known as the *single scattering albedo*. When a photon interacts with a collection of particles, and an extinction or attenuation event occurs, the single scattering albedo is the probability for the photon to be scattered. The probability for the photon to be absorbed is then $(1 - \omega_0)$.

Scattering phase functions

When a collection of photons of flux $d^2\Phi^s$ is scattered from the incident direction $\hat{\mathbf{\Omega}}'$ into the solid angle $d\omega$ centered around the direction $\hat{\mathbf{\Omega}}$, we can define the *volume scattering function* as

$$\beta(\hat{\mathbf{\Omega}}', \hat{\mathbf{\Omega}}) = \frac{1}{ds\, d\omega} \frac{d^2\Phi^s}{\Phi^i}.$$

Here $\beta(\hat{\mathbf{\Omega}}', \hat{\mathbf{\Omega}})$ is the probability for the described scattering to occur within a volume element with thickness ds. The scattering angle Θ is given by $\cos\Theta = \hat{\mathbf{\Omega}}' \cdot \hat{\mathbf{\Omega}}$ and the plane spanned by $\hat{\mathbf{\Omega}}'$ and $\hat{\mathbf{\Omega}}$ is referred to as the *scattering plane*. The unit of the volume scattering function is $[m^{-1}sr^{-1}]$. If we integrate the volume scattering function over the entire sphere surrounding the volume element, we get

$$\int_{4\pi} \beta(\hat{\mathbf{\Omega}}', \hat{\mathbf{\Omega}})\, d\omega = \frac{1}{ds} \frac{d\Phi^s}{\Phi^i}. \tag{1.11}$$

The right hand side of Eq. (1.11) is identical to the absolute value of the right hand side of Eq. (1.10). Thus Eq. (1.11) is another expression for the scattering coefficient b. For the case in which the scattered photons are uniformly distributed over the azimuth angle ϕ' we get

$$\begin{aligned} b &= \int_{4\pi} \beta(\theta', \phi',\, \theta, \phi)\, \sin\theta\, d\theta\, d\phi \\ &= 2\pi \int_0^{\pi} \beta(\theta)\, \sin\theta\, d\theta \end{aligned} \tag{1.12}$$

which gives

$$1 = 2\pi \int_0^{\pi} \frac{\beta(\theta)}{b}\, \sin\theta\, d\theta.$$

Thus, we may define the *normalized volume scattering function*

$$\tilde{\beta} = \frac{\beta(\theta)}{b}.$$

The quantity $\tilde{\beta}$ describes the angular distribution of the scattering while b describes the magnitude of it.

There exist different *phase functions* describing the volume scattering function β. In our model for scattering on algae and particles in the medium we have chosen to use the one-parameter phase function proposed by L. Henyey and J. Greenstein [5]

$$\tilde{\beta}(\Theta) = \frac{1-g^2}{(1+g^2-2g\cos\Theta)^{3/2}}. \tag{1.13}$$

This function has no physical basis, but is found to give a reasonable approximation. Since the function only contains one parameter (g), it is very suitable for simulations. This parameter is known as the *asymmetry factor*, and its properties are discussed later.

Whereas the Henyey-Greenstein (HG) scattering function gives a good description of scattering by particles, it is not suitable for describing molecular scattering. When a molecule interacts with an electromagnetic wave, the molecule starts oscillating due to the force excerted by its electric field. The scattered field will then be the field radiated by the corresponding induced electric dipole. The radiation pattern in the far field is then proportional to $\Pi \sin^2\theta$, where θ is the polar angle measured from the dipole axis and Π is the induced dipole moment along that axis. It is sufficient to consider two linearly polarized incident waves, one with the electric field parallel to the scattering plane and the other with the electric field perpendicular to the scattering plane, as shown in fig. 1.5. These waves induce dipoles with axes along the respective incident fields. From fig. 1.5 we see that if the incident electric field vector is parallel to the scattering plane, the angle between the induced dipole $\Pi_{\|}$ and the direction of scattering $\hat{\mathbf{\Omega}}$ is $\pi/2+\Theta$. Thus, the scattered intensity is

$$I_{\|} \propto \Pi_{\|} \sin^2\left(\frac{\pi}{2}+\Theta\right) = \Pi_{\|}\cos^2\Theta.$$

If the incident electric field vector is normal to the scattering plane, we see that the angle between the induced dipole $\Pi_{\perp}$ and the direction of scattering is always $\pi/2$, thus, the scattered intensity is

$$I_{\perp} \propto \Pi_{\perp}.$$

We are considering natural unpolarized light, which can be treated as a sum of two orthogonal linearly polarized waves that are independent of one another and have equal intensity $I_{\|} = I_{\perp} = I/2$. The Rayleigh scattering phase function for unpolarized light is proportional to the scattered intensity, hence

$$\tilde{\beta}(\Theta) = C(1+\cos^2\Theta) \tag{1.14}$$

where the constant C is the magnitude of the scattering normal to the incident direction. The theory of scattering by a dipole was original developed by

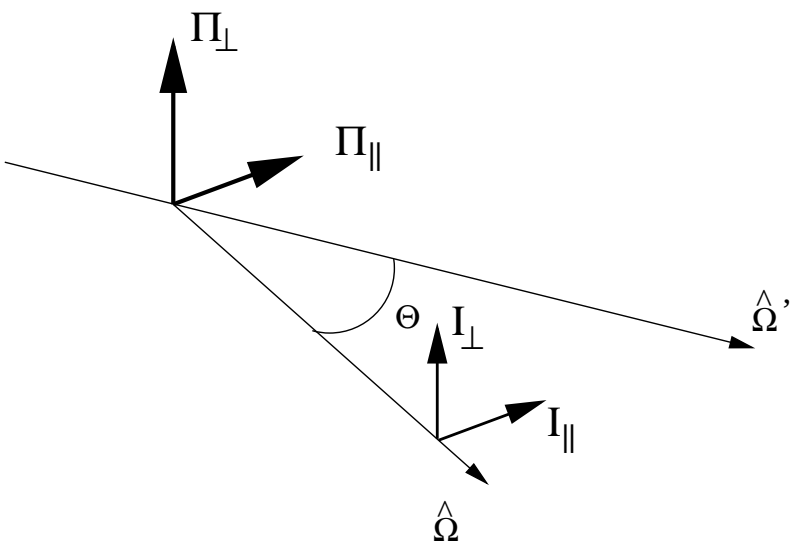

Figure 1.5: Illustration of the two components of Rayleigh scattering. $\hat{\mathbf{\Omega}}'$ and $\hat{\mathbf{\Omega}}$ are units vectors along the incident and scattered propagations vectors, respectively. $\Pi_\perp$ and $\Pi_\parallel$ are the induced dipole moments of the electrical field polarized perpendicular to and parallel with the scattering plane. $I_\perp$ and $I_\parallel$ are the scattered intensities in the direction $\hat{\mathbf{\Omega}}$. The scattered intensities are proportional to their corresponding dipole moments (After Thomas and Stamnes [1]).

Rayleigh [6]. The treatment given here is based on that presented by Thomas and Stamnes [1]. Experiments have shown that the light scattered at 90° is not totally polarized as expected from the analysis. Rayleigh explained the depolarization by anisotropy of molecules [7] and introduced the polarization ratio $\delta = I_\parallel/I_\perp$. Therefore, Eq. (1.14) has been modified by introdousing the *polarization factor* $p = (1-\delta)/(1+\delta) \leq 1$ by Morel and Gentili [8] to obtain

$$\tilde{\beta}(\Theta) = C(1 + p\cos^2\Theta). \tag{1.15}$$

The proportionality constant C follows from

$$\begin{aligned} 4\pi &= \int_{4\pi} C(1 + p\cos^2\Theta)\, d\omega \\ &= 2\pi C \int_0^\pi (1 + p\cos^2\theta)\sin\theta\, d\theta \end{aligned}$$

which gives

$$C = \frac{3}{3+p}.$$

Thus

$$\tilde{\beta}(\Theta) = \frac{3}{3+p}(1 + p\cos^2\Theta). \tag{1.16}$$

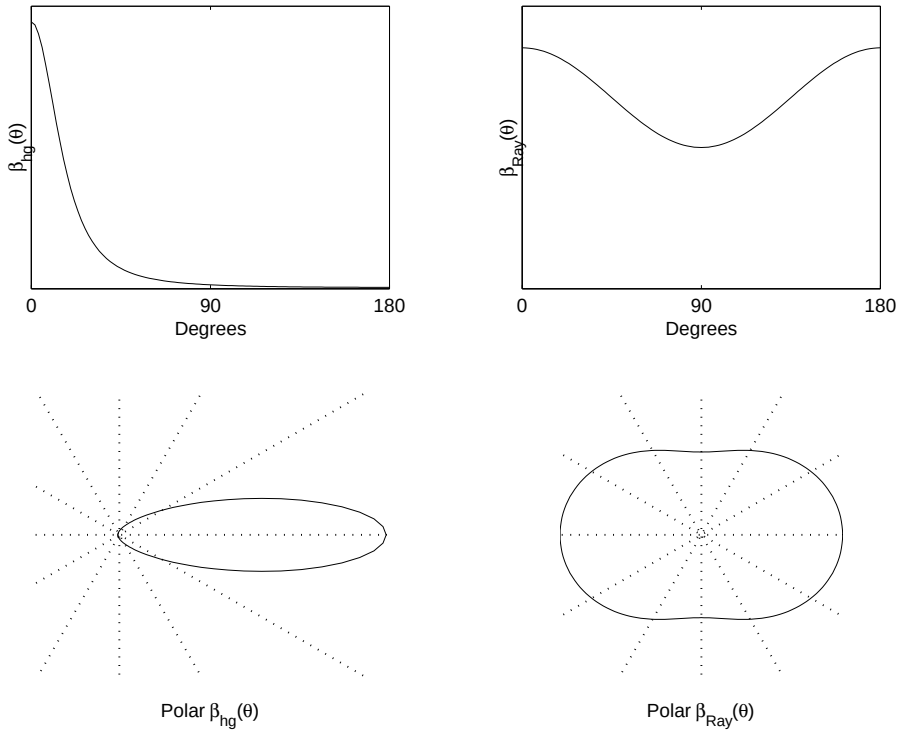

Figure 1.6: Angular distribution of Henyey-Greenstein scattering (upper left) and Rayleigh scattering with $p = 0.84$ (upper right). In the polar representation (lower panels) the incident light propagates in direction 0°.

Fig. 1.6 shows the distributions of Henyey-Greenstein scattering with asymmetry factor $g = 0.7$ and of Rayleigh scattering with polarization factor $p = 0.84$.

The phase functions may be expanded in a finite series of $2N$ *Legendre polynomials* as follows [1]

$$\tilde{\beta}(\Theta) \approx \sum_{l=0}^{2N-1} (2l-1)\,\chi_l\,P_l(\cos\Theta),$$

where $P_l(\cos\Theta)$ is the lth *Legendre polynomial* and χ_l the lth phase function moment. The first five Legendre polynomials are

$$\begin{aligned} P_0(\mu) &= 1, \\ P_1(\mu) &= \mu, \\ P_2(\mu) &= \frac{1}{2}(3\mu^2 - 1), \end{aligned}$$

$$P_3(\mu) = \frac{1}{2}(5\mu^3 - 3\mu),$$
$$P_4(\mu) = \frac{1}{2}(35\mu^4 - 30\mu^2 + 3)$$

where $\mu = \cos\theta$. Normalization of the phase function gives $\chi_0 = 1$. The next phase moment is the asymmetry factor, as mentioned before, and it is often denoted by the symbol $g \equiv \chi_1$. When $g = 0$ we have symmetric scattering about $\cos\Theta = 0$, when $g = -1$ we have complete backscattering, and when $g = 1$ we have complete forward scattering. The HG scattering function has the feature that all phase moments can be expressed in powers of the asymmetry factor

$$\chi_l = (g)^l, \ \forall\, l.$$

This property makes the HG-function very suitable for calculations in which the Legendre polynomials are used because only one phase moment must be specified. From Eq. (1.16) we see that the Rayleigh scattering function can be expressed in terms of only the first three polynomials. As above, normalization gives $\chi_0 = 1$, and since the function is symmetric about $\cos\Theta = 0$, we get $\chi_1 = 0$. It is also easy to show that

$$\chi_2 = \frac{2p}{5(3+p)} \iff p = \frac{15\chi_2}{2 - 5\chi_2}.$$

We have now seen how analytical formulas or series can be used to describe scattering functions. Alternatively they could be described by given tables. The advantage of using tables is that scattering functions of any shape can be included into the model. It is also convenient to use tables for cases in which we want to define a scattering function based on measurements.

IOPs of atmosphere

Light is absorbed and scattered by molecules and aerosols in the atmosphere. The total absorption and scattering coefficients a and b for the atmosphere are then the sum of the absorption coefficients and the scattering coefficients for the aerosols and the atmospheric molecules, i. e. $a = a_{mol} + a_{aer}$ and $b = b_{mol} + b_{aer}$. Atmospheric molecular scattering is assumed to be perfect Rayleigh scattering, i. e. the polarization factor $p = 1$ in Eq. (1.15). Scattering by aerosols can be treated as HG scattering.

IOPs of sea ice

In sea ice light is attenuated due to brine pockets, air bubbles, the ice itself, and sometimes also due to algae distributed throughout the bottom few centimeters of the ice. The total absorption and scattering coefficients a and b for the ice are then the sum of the absorption and scattering coefficients of each spiecies, i. e.

$a = a_{br} + a_{bub} + a_{ice} + a_{alg}$ and $b = b_{br} + b_{bub} + b_{ice} + b_{alg}$. We assume scattering from pure ice and algae to be negligible compared to scattering from brine pockets and air bubbles. Mie calculations [9, 10] give the scattering functions for brine pockets and air bubbles. The asymmetry factor for brine pockets is $g_{br} \approx 0.99$. The asymmetry factor is so large because the brine pockets are much larger than the wave length of the light and their index of refraction is very close to that of the surrounding ice [11]. The asymmetry factor for the bubbles is $g_{bub} \approx 0.85$. Even though air bubbles are larger than brine pockets, their asymmetry factor is smaller due to the larger index of refraction difference between air and ice. We assume that the scattering phase function of the sea ice can be described by a HG scattering function. The effective asymmetry factor is given by

$$g = \frac{g_{br} b_{br} + g_{bub} b_{bub}}{b_{br} + b_{bub}}.$$

The salinity distribution through the ice has a typical c-shaped profile, ranging from ~0.8% near the surface via ~0.4% in the bulk of the interior to 1% near the bottom. Note that the salinity is smaller than the brine volume (5-12%) in the sea ice. The air volume is about 4% in the upper 10 cm of the ice, but is less than 1% in the remainder of the ice [11, 12]. Due to the air content in the upper layer of the ice the asymmetry factor g is lower there than in the rest of the ice. Hence, the asymmetry factor increases from ~ 0.90 at the surface to ~ 0.99 in the core and and near the bottom. Because of air bubbles and brine pockets of the ice the magnitude of the scattering coefficient b is much larger for the sea ice than for the ocean. For sea ice the magnitude of b can be greater than $200\ m^{-1}$ while in the ocean it is less than $0.1\ m^{-1}$. The absorption coefficient a, however, is approximately two times greater in the ice than in the ocean. Hence, the single scattering albedo is close to one in sea ice.

IOPs of sea water

Light is absorbed and scattered by molecules and algae in the ocean. The total absorption and scattering coefficients a and b for the ocean are then the sum of the absorption and scattering coefficients of the algae and the molecules, i. e. $a = a_{alg} + a_{mol}$ and $b = b_{alg} + b_{mol}$. For pure sea water Morel [13] found $p \approx 0.84$ in Eq. (1.15) to give a good agreement between the theoretical formula and the experimental measurements. Further, we make the assumption that scattering by algae may be treated as HG scattering.

1.1.2 Apparent optical properties

In contrast to an inherent optical property, which only depends on the medium, an apparent optical property (AOP) also depends on the incident light field. Thus, in marine optics AOPs also depend on factors such as the sun angle, the

ratio of the direct sun light to the scattered light from the sky and the roughness of the sea surface. Some of the AOPs are associated with the irradiance. Thus, the *reflectance* is defined as the ratio between the upwelling and the downwelling plane irradiances, i. e.

$$R = \frac{E_u}{E_d} \tag{1.17}$$

while the *remote-sensing reflectance* R_{rs} is defined by

$$R_{rs} = \frac{L(\hat{\mathbf{\Omega}})}{E_d}.$$

The reflectance is dimensionless and is usually measured just below the sea surface, while the remote-sensing reflectance has dimension $[sr^{-1}]$ and is evaluated in the air just above the sea surface. R_{rs} is a measure of how much light that is returned into the direction $\hat{\mathbf{\Omega}}$, in the atmosphere. Both R and R_{rs} are important for calculations in marine optics. The *average downwelling cosine* is defined by

$$\overline{\mu}_d = \frac{\int_{\Omega_d} L(\Omega)\cos\theta\, d\omega}{\int_{\Omega_d} L(\Omega)\, d\omega} = \frac{E_d}{E_{0d}}.$$

In the same way we can define the *average upwelling cosine* by

$$\overline{\mu}_u = \frac{\int_{\Omega_u} L(\Omega)\cos\theta\, d\omega}{\int_{\Omega_u} L(\Omega)\, d\omega} = \frac{E_u}{E_{0u}}$$

and the *average cosine* by

$$\overline{\mu} = \frac{\int_{4\pi} L(\Omega)\cos\theta\, d\omega}{\int_{4\pi} L(\Omega)\, d\omega} = \frac{E_d - E_u}{E_0}. \tag{1.18}$$

Some authors refer to *distribution functions* D_d and D_u rather than average cosines. The distribution functions are defined by

$$D_d = \frac{1}{\overline{\mu}_d} \text{ and } D_u = \frac{1}{\overline{\mu}_u}.$$

Since the irradiance decays approximately exponentially with depth, it is useful to define the diffuse attenuation coefficients, K_u, K_d, K_E and K_0 for the upwelling, downwelling, net downwelling and scalar irradiance, respectively. In the same way as we defined the attenuation coefficient c in Eq. (1.7), we have

$$K_d = -\frac{1}{dz}\frac{dE_d}{E_d} \tag{1.19}$$

$$K_u = -\frac{1}{dz}\frac{dE_u}{E_u} \tag{1.20}$$

$$K_E = -\frac{1}{dz}\frac{d(E_d - E_u)}{(E_d - E_u)} \tag{1.21}$$

$$K_0 = -\frac{1}{dz}\frac{dE_0}{E_0}. \tag{1.22}$$

Solving Eq. (1.19), we get

$$E_d = E_d^i e^{-K_d z}. \tag{1.23}$$

There are several reasons why the diffuse attenuation coefficients are useful. For instance there is a correlation between them and the concentration of phytoplankton and chlorophyll in the ocean. Hence the K-functions provide a connection between biology and optics. About 90% of the light that is returned to the atmosphere from the ocean comes from a top layer with a depth of $1/K_d$. Thus, K_d is important in remote sensing. Note that in contrast to the IOPs, the AOPs cannot be obtained by performing measurements on water samples since they depend on the incident light field, and while the IOPs are additive, the AOPs are not.

1.1.3 The Gershun relationship

Consider a slab in a medium with thickness dz (fig. 1.7). The total irradiance entering the slab is then $E_d + E_u + dE_u$ while the total outgoing irradiance is $E_d + dE_d + E_u$. Thus, the difference is $dE_u - dE_d$. The energy loss of the light within volume element is then

$$d\Phi^a = (dE_u - dE_d)dA$$

where dA is the area of the slab. The energy loss per unit of volume becomes

$$\begin{aligned} \frac{d\Phi^a}{dA\,dz} &= -\frac{d}{dz}(E_d - E_u) \\ &= K_E E_{tot} \end{aligned} \tag{1.24}$$

where $E_{tot} = (E_d - E_u)$ is the total irradiance. The last result (Eq. (1.24)) follows from Eq. (1.21).

The absorbed energy in the volume element can be calculated by using Eq. (1.4) in differential form, i. e.

$$dE = L(\hat{\mathbf{\Omega}}) \cos\theta \, d\omega$$

which on using Eq. (1.5), gives

$$d^2\Phi = dE\,dA = L(\hat{\mathbf{\Omega}}) \cos\theta \, d\omega \, dA.$$

The fraction of $d^2\Phi$ that is absorbed follows from Eq. (1.9), i. e.

$$\begin{aligned} d^2\Phi^a &= a\, d^2\Phi \frac{dz}{\cos\theta} \\ &= a\, dA\, dz\, L(\hat{\mathbf{\Omega}})\, d\omega. \end{aligned}$$

By integrating over all solid angles we find

$$\begin{aligned} d\Phi^a &= a\, dA\, dz \int_{4\pi} L(\hat{\mathbf{\Omega}})\, d\omega \\ &= a\, dA\, dz\, E_0 \end{aligned}$$

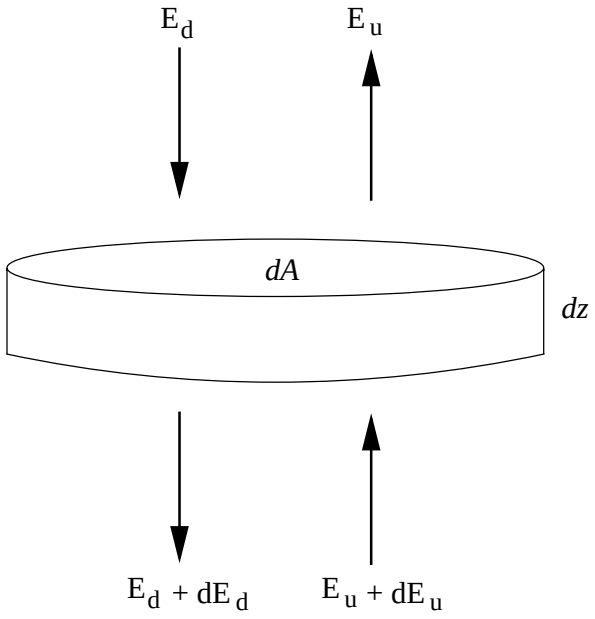

Figure 1.7: A slab of thickness dz and area dA. The input irradiance is $E_d + E_u + dE_u$, and the output irradiance is $E_d + dE_d + E_u$.

or

$$\frac{d\Phi^a}{dA\,dz} = aE_0 \tag{1.25}$$

where $E_0 = E_{0d} + E_{0u}$ is the total scalar irradiance. The left hand sides of Eq. (1.24) and Eq. (1.25) are identical, which means that the energy loss of the light in the slab is equal to the absorbed energy. This is known as Gershun's law [14, 2, 4], and it implies conservation of energy in the volume element $dV = dz\,dA$, i. e.

$$K_E E_{tot} = aE_0. \tag{1.26}$$

By using Eq. (1.18), we can rewrite Eq. (1.26) as

$$K_E = \frac{a}{\overline{\mu}} = \frac{a}{\overline{\cos\theta}}. \tag{1.27}$$

1.1.4 The radiative transfer equation and the DISORT algorithm

The radiated field in the atmosphere and the ocean may be separated into two different components. The first one is the direct or *solar* component L_{sol}, which is the part of incident radiation that has survived the extinction (see Eq. (1.8)), i. e.

$$L_{sol}(\tau, \mu, \phi) = F_0 \delta(\mu - \mu_0) e^{-\tau/\mu_0}$$

Here $\mu = \cos\theta$, $\mu_0 = \cos\theta_0$, and θ_0 is the zenith angle. F_0 is the solar irradiance, normal to the solar beam, at the top of the atmosphere in direction (μ_0, ϕ_0) and $\tau = \tau(z)$ is the vertical optical depth of the medium. The dimensionless differential optical depth is defined as

$$d\tau = -\sum_i (a_i + b_i)\, dz = -(a+b)\, dz,$$

where a_i and b_i are the absorption and scattering coefficients of the ith radiatively active species, and a and b are the total absorption and scattering coefficients.

We now consider a medium in which the IOPs only vary in the vertical direction. The radiance distribution can then be described by the *radiative transfer equation (RTE)*

$$\begin{aligned} \mu \frac{dL}{d\tau} = & - L + (1-\omega_0) B(T) \\ & + \frac{\omega_0}{4\pi} \int_{4\pi} \tilde{\beta}(\hat{\mathbf{\Omega}}', \hat{\mathbf{\Omega}}) L(\hat{\mathbf{\Omega}}') d\omega'. \end{aligned} \tag{1.28}$$

The first term on the right hand side of Eq. (1.28) follows from the extinction law, as mentioned before (Eq. (1.8)). The second term is the contribution to the radiance due to thermal emission in the medium. The factor $B(T)$ is the isotropic radiance emitted by a blackbody. $B(T)$ is known, and it varies only with the temperature T. But the temperature itself may vary along the path thus, $B(T) = B(\,T(\tau)\,)$. The third term in Eq. (1.28) is the gain of radiance due to photons scattered from any direction $\hat{\mathbf{\Omega}}'$ into the direction $\hat{\mathbf{\Omega}}$. In the following we ignore the thermal emission since its contribution in the short wave part of the spectrum is not significant compared to the extinguished solar beam and the scattered light. It is also convenient to separate the third term in Eq. (1.28) into a single-scattering term S^*, which is the source due to scattering of solar radiation, and a multiple scattering term. Hence we rewrite Eq. (1.28) as

$$\begin{aligned} \mu \frac{dL(\tau,\mu,\phi)}{d\tau} = & - L(\tau,\mu,\phi) \\ & + \frac{\omega_0}{4\pi} \int_{4\pi} \tilde{\beta}(\hat{\mathbf{\Omega}}', \hat{\mathbf{\Omega}}) L(\hat{\mathbf{\Omega}}') d\omega' + S^*(\tau,\mu',\phi'). \end{aligned} \tag{1.29}$$

Note that the single-scattering term is different in the atmosphere and in the ocean. In the atmosphere we have

$$\begin{aligned} S^*_{atm}(\tau,\mu,\phi) = & \frac{\omega_0(\tau) F_0}{4\pi} \tilde{\beta}(\tau, -\mu_0, \phi_0; \mu, \phi) e^{-\tau/\mu_0} \\ & + \frac{\omega_0(\tau) F_0}{4\pi} \rho_s(-\mu_0; n_{rel}) \tilde{\beta}(\tau, \mu_0, \phi_0; \mu, \phi) e^{-(2\tau_a - \tau)/\mu_0} \end{aligned}$$

where $n_{rel} = n_{ocn}/n_{atm}$ is the index of refraction in the ocean relative to the index of refraction in the atmosphere, τ_a is the vertical optical depth of the

atmosphere, and $\rho_s(-\mu_0; n_{rel})$ is the specular reflection by the atmosphere-ocean interface. The first term is due to first order scattering of the solar beam while the second term is due to first order scattering of the reflected beam from the ocean surface. The source term in the ocean consist of the attenuated solar beam refracted through the surface, i. e.

$$\begin{aligned} S^*_{ocn}(\tau,\mu,\phi) &= \frac{\omega_0(\tau)F_0}{4\pi}\frac{\mu_0}{\mu_{0n}}\mathcal{T}(-\mu_0; n_{rel}) \\ &\times \tilde{\beta}(\tau,-\mu_{0n},\phi_0;\mu,\phi)e^{-\tau_a/\mu_0}e^{-(\tau-\tau_a)/\mu_{0n}} \end{aligned}$$

where $\mathcal{T}(-\mu_0; n_{rel})$ is the transmittance through the interface, and μ_{0n} is the cosine of the zenith angle in the ocean, related to μ_0 by Snell's law (see section 3.2.2). In the DISORT routine we assume a calm surface between the atmosphere and the ocean. Thus, the angle of incidence is identical to the zenith angle, i. e. $\theta_i = \theta_0$, and the angle of refraction into the ocean is the same regardless of wind speed.

The algorithm of the DISORT program, is based on solving Eq. (1.29). To that end, one first isolat the azimuth dependence by expanding the phase function β in *Legendre polynomials*. For the atmosphere-ocean case this was first done by Jin and Stamnes [15], see also Thomas and Stamnes [1] and Frette et al. [16]

$$\tilde{\beta}(\hat{\mathbf{\Omega}}', \hat{\mathbf{\Omega}}) = \sum_{m=0}^{2N-1}(2-\delta_{0,m})\tilde{\beta}^m(\mu',\mu)\cos m(\phi'-\phi)$$

where $\delta_{0,m}$ is the Kronecker delta function, $\delta_{0,m} = 1$ for $m = 0$ and $\delta_{0,m} = 0$ for $m \neq 0$, and

$$\tilde{\beta}^m(\mu',\mu) = \sum_{l=m}^{2N-1}(2l+1)\chi_l\Lambda_l^m(\mu')\Lambda_l^m(\mu). \tag{1.30}$$

Here

$$\Lambda_l^m(\mu) \equiv \sqrt{\frac{(l-m)!}{(l+m)!}}P_l^m(\mu),$$

$P_l^m(\mu)$ is the associated Legendre polynomial, and χ_l is the expansion coefficient. Expanding the radiance in the same way we get

$$L(\mu,\phi) = \sum_{m=0}^{2N-1}L^m(\mu)\cos m(\phi-\phi_0).$$

where ϕ_0 is the incident azimuth angle. We find that each Fourier component satisfies the RTE, i. e.

$$\begin{aligned} \frac{dL^m(\tau,\mu)}{d\tau} &= -L^m(\tau,\mu) + S^{*m}(\tau,\mu) \\ &+ \frac{\omega_0(\tau)}{2}\int_{-1}^{1}\beta^m(\tau,\mu',\mu)\,L^m(\tau,\mu)\,d\mu \end{aligned} \tag{1.31}$$

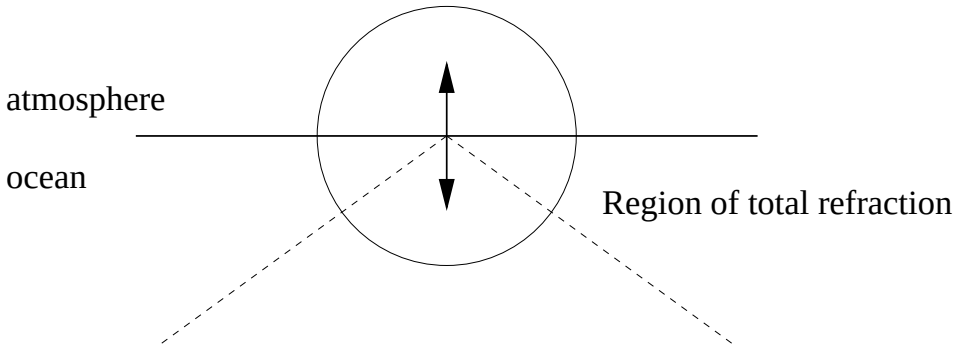

Figure 1.8: The region of total refraction.

where $m = 0, 1, 2, \ldots, 2N-1$ and $\tilde{\beta}^m(\mu', \mu)$ is given by Eq. (1.30). To solve this equation we need to take into account the boundary conditions at the top of the atmosphere and at the bottom of the ocean and also the reflection and transmission at the atmosphere-ocean interface. In addition there are continuity conditions that must be satisfied at each interface between horizontal layers with different optical properties in the atmosphere and the ocean. Further we approximate the integral in Eq. (1.31) by a quadrature sum consisting of $2N_1$ terms in the atmosphere and $2N_2$ terms in the ocean, where N_1 terms are used to represent the radiance in the downward hemisphere in the atmosphere that refracts through the interface into the ocean. It is necessary that $N_2 > N_1$ because we need additional terms in the ocean to represent the region of total reflection, see fig. 1.8. The relation between N_1 and N_2 is given by $N_2 = 2n_{ocn}N_1$. There are also N_1 and N_2 streams in the upward direction in the atmosphere and ocean, respectively. Using the discrete ordinate approximation to Eq. (1.31) we can solve it to obtain the radiance at different vertical positions both in the atmosphere and in the ocean. The solution in the pth layer in the atmosphere becomes

$$L_p(\tau, \pm\mu_i^a) = \sum_{j=1}^{N_1} C_{-jp} g_{-jp}(\pm\mu_i^a) e^{k_{jp}^a \tau} + C_{jp} g_{jp}(\pm\mu_i^a) e^{-k_{jp}^a \tau} + U_p(\tau, \pm\mu_i^a)$$

where $i = 1, \ldots, N_1$ and p is less than or equal to the numbers of layers in the atmosphere. The solution in the qth layer in the ocean becomes

$$L_q(\tau, \pm\mu_i^o) = \sum_{j=1}^{N_2} C_{-jq} g_{-jq}(\pm\mu_i^o) e^{k_{jq}^o \tau} + C_{jq} g_{jq}(\pm\mu_i^o) e^{-k_{jq}^o \tau} + U_q(\tau, \pm\mu_i^o)$$

where $i = 1, \ldots, N_2$ and q is greater than the numbers of layers in the atmosphere and less than or equal to the total numbers of layers in the atmosphere and ocean. The subscripts a and o is used to denote atmospheric and oceanic parameters, respectively, the plus (minus) sign is for radiance streaming upwards (downwards)

and $k^a_{jp}, g_{jp}, k^o_{jq}$, and g_{jq} are eigenvalues and eigenvectors determined by solution of an algebraic eigenvalue problem that results when we seek a solution to the homogeneous version ($S^{*m}(\mu) = 0$) of Eq. (1.31). The terms $U_p(\pm\mu^a_i)$ and $U_q(\pm\mu^o_i)$ are the specific solutions. The coefficients C_{jp} and C_{jq} are determined by the boundary conditions, the continuity of the radiance at each interface between the layers, and Fresnel's equations. As mentioned previously, this method is only suitable for layers with no horizontal variations.

Chapter 2

Monte Carlo

The principle of Monte Carlo simulations is that in a given situation in which more than one possible event may occur, a random number is generated that decides the outcome. The random numbers are uniformly distributed in the interval [0,1]. Monte Carlo methods have been used for centuries, but only in the past several decades has the technique gained the status of a full-fledged numerical method capable of addressing the most complex applications. It may seem wrong to use a computer to produce random numbers, since computers are the most deterministic machines created by man. In fact any program will produce an output that is entirely predictable, and hence not truly random.

But the algorithm described by Press et al. [17] generates numbers that are not correlated and thus adequate for all practical Monte Carlo simulations. Hence, the result obtained by using this algorithm is statistically acceptable for our purpose.

2.1 Monte Carlo in marine optics

When dealing with atmospheric and marine optics, we are interested in the irradiance and the scalar irradiance crossing finite horizontal or tilted surfaces at different depths and different horizontal positions. However, when using a Monte Carlo model, we do not deal with irradiances. Instead we are dealing with photons. Therefore, it is necessary to calculate the irradiances from the detected photons in the Monte Carlo routine. The irradiance is the flux crossing a given finite horizontal or tilted surface divided by the area of the surface. By assuming that the area A is of fixed size and that the photons are uniformly distributed over it, we find the irradiance E by using Eq. (1.1) and Eq. (1.6), i. e.

$$E_p = \frac{d\Phi}{dA} = \frac{\Phi}{A} = \frac{hc}{A\lambda} N.$$

Here the subscript $p = u,\ d,$ and N is the number of photons per second. Thus, the irradiance is proportional to the number of photons crossing the finite surface.

The scalar irradiance is proportional to the energy density associated with the light field at a given location. By using Eq. (1.1) and Eq. (1.6) and making the same assumptions as above, we get

$$\begin{aligned} E_{0p} &= \int_{\Omega_p} L(\hat{\mathbf{\Omega}})\, d\omega \\ &= \int_{\Omega_p} \frac{d^2\Phi}{dA\, \cos\theta\, d\omega}\, d\omega \\ &\approx \sum_{i=1}^{N} \frac{\Phi}{A\, \cos\theta_i} \\ &= \frac{hc}{\lambda A} \sum_{i=1}^{N} \frac{1}{\cos\theta_i} \end{aligned} \tag{2.1}$$

where $p = u,\ d$, and θ_i is the angle of incidence for photon number i relative to the normal of the detecting surface. Hence, the scalar irradiance is proportional to the weighted sum of photons crossing the finite surface, where each photon has been weighted by the factor $(\cos\theta_i)^{-1}$. Note that these equations are valid both when the detecting surface is horizontal and when it is tilted. For the special case in which θ_i is equal to $\pi/2$, the direction of the photon is parallel to the detecting surface, so the photon will not be detected. Therefore Eq. (2.1) never becomes an expression with zero in the denominator.

2.2 Advantages and drawbacks of Monte Carlo simulations

Monte Carlo simulation is a powerful tool to solve physical problems in many different fields. Because the fundamentals of a Monte Carlo routine are very simple, it is easy to create a model that is able to describe complex problems. In order to have full flexibility when simulating photons that pass through the atmosphere and the ocean, we have chosen to make the model three-dimensional (3D). This gives us the opportunity to include many vital physical details like clouds, algae blooms, edges of ice or a three-dimensional topography like coast lines and mountains in fjords and coastal water. The flexibility of the Monte Carlo method offers a great advantage compared to other methods, such as e.g. the DISORT which is limited to the treatment of one-dimensional (1D) geometries. Hence, the advantage of the Monte Carlo method is that fewer restrictions are required to run the program and therefore its ability to adapt to specific geometries is much better than with any other method.

However, even though the Monte Carlo method is very flexible, it has some drawbacks that make it less suitable for regular use. The main drawback is

that a Monte Carlo routine puts very heavy demands on the CPU time. As more geometrical details are included in the program, more photons must be employed to get an acceptable accuracy and the number of calculations required for each photon increases as well, and therefore the CPU time grows rapidly. For this reason, the use of a Monte Carlo (MC) model requires that the user has access to a supercomputer. Otherwise the MC code might run for days or weeks, depending on how complex the system is. The MC algorithm is well suited for parallel processing, since all photons are totally independent.

Chapter 3

Algorithm of the Monte Carlo program

In this chapter we will discuss the algorithm we have developed for doing Monte Carlo (MC) simulations. As mentioned earlier, our aim was to create a flexible three-dimensional model that is able to handle variations of the physical properties, both vertically and horizontally. Here we will take a closer look at how this is done.

3.1 Structure of program

To allow for three-dimensional variations it is necessary to split up both the atmosphere and the ocean into cells rather than using a one-dimensional stratification. Each cell has its own individual Inherent Optical Properties (IOPs), i. e. it has its own individual index of refraction n, absorption coefficient a, scattering coefficient b, asymmetry parameter g for the Henyey-Greenstein scattering function, polarization factor p for the Rayleigh scattering function, and probability η for a given scattering event to be Rayleigh scattering. Here η is given by

$$\eta = \frac{b_{Ray}}{b_{hg} + b_{Ray}} = \frac{b_{Ray}}{b}$$

where the the scattering coefficient $b = b_{hg} + b_{Ray}$ consists of both HG scattering and Rayleigh scattering.

When calculating the path of a photon through the system, the routine does one cell at the time, see fig. 3.1. An initial path length is first calculated, see section 3.2.1, and the path from the entrance point to the exit point of each cell is calculated. Before the remaining path length in the next cell is evaluated, new values for n, a, b, η, p, and g are given. This process continues until the path length is totally "consumed". Then there are two possible outcomes, either the photon is scattered into a new direction with a new initial path length or it is

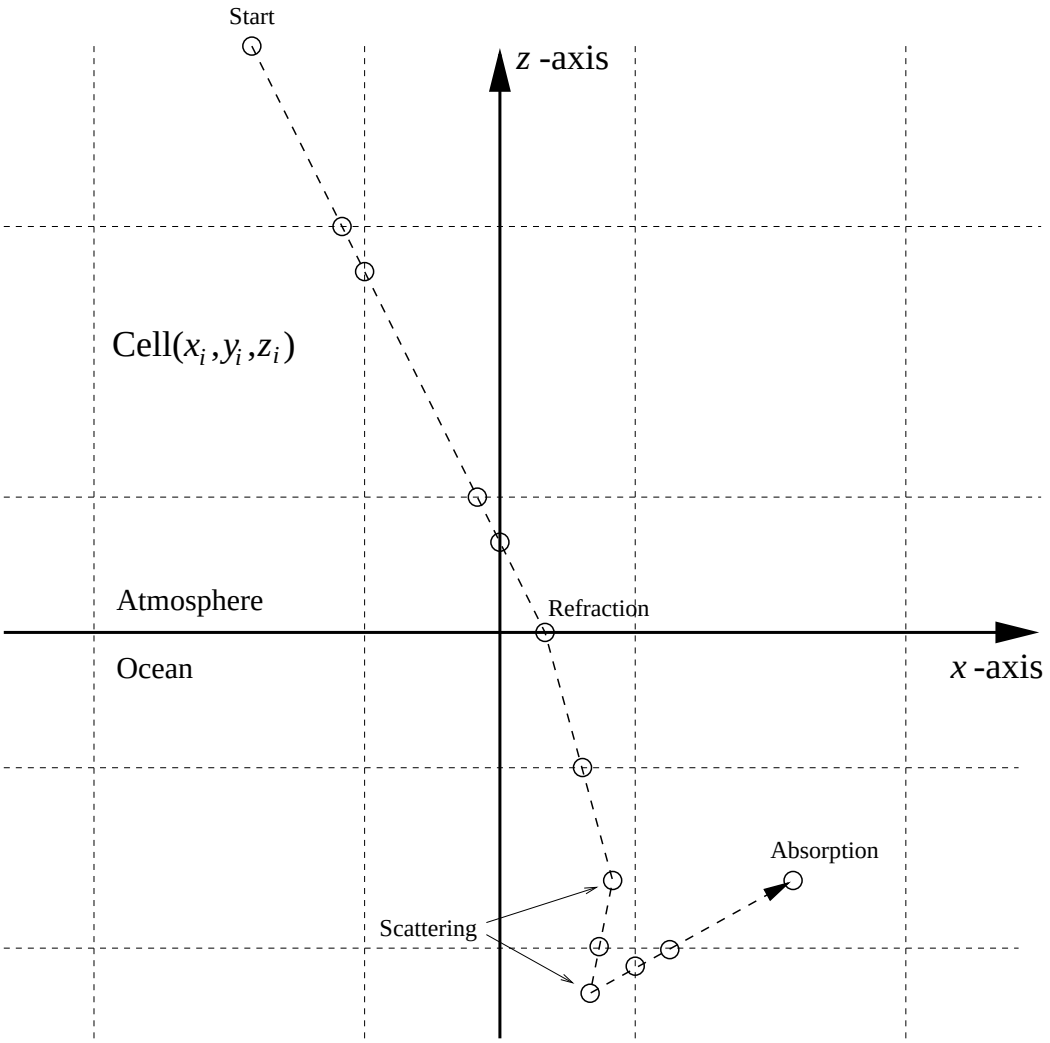

Figure 3.1: One photon travels from the point 'start' to the point 'absorption'. The intersection points between the cells are marked with circles, and so are the points of refraction, scattering, and absorption. This figure shows the structure of a 2D routine. The Monte Carlo program, however, is a 3D routine but it follows the same principles.

absorbed. When the photon hits a cell interface at which the index of refraction changes, a probability routine is called to decide whether the photon is reflected or refracted, the routine also decides the new direction of the photon.

Solar light is unpolarized. This implies that when a photon hits a cell interface at which the index of refraction changes, the reflectance R is given by $R = \frac{1}{2}(R^{TE} + R^{TM})$, where R^{TE} is the reflectance for light polarized with the electric field perpendicular to the plane of incidence and R^{TM} is the reflectance for light

polarized with the electric field parallel to the plane of incidence [18, 19]. Thus, we get

$$R = \frac{1}{2}\left(\frac{\sin^2(\theta_i - \theta_t)}{\sin^2(\theta_i + \theta_t)} + \frac{\tan^2(\theta_i - \theta_t)}{\tan^2(\theta_i + \theta_t)}\right)$$

where θ_i is the angle of the incidence and θ_t is the refracted angle found by using Snell's law. A random number decides whether the photon is reflected back to the current cell or is transmitted into the next cell with another index of refraction. Then the routine continues to calculate the path of the photon. To compute irradiances we need a routine to detect the photons. In this program the detectors are horizontal and located at the bottom of each cell. The detectors distinguish between photons traveling upwards and downwards and determine both the irradiance and the scalar irradiance. The logical structure, shown in fig. 3.2, describes the life of a photon from it enters the atmosphere until it is absorbed or returned to space. A more detailed explanation of the boxes in fig. 3.2 is given in appendix A.1.

3.2 Probability density functions

In many situations there are different possible outcomes in the MC routine. The outcome of a certain situation might be expressed with a *probability density function* $p(x)$ where x lies in any given interval $[a,b]$ and might be arbitrary distributed within this interval. The function $p(x)$ denotes the probability for the outcome to be x in exactly this situation. As explained earlier, the MC routine generates random numbers that are uniformly distributed in the interval [0,1]. To obtain a random number in the correct interval $[a,b]$ and with correct distribution $p(x)$ we need to transform a random number $\rho \in [0,1]$ generated by the computer, to a random number $x \in [a,b]$. One way to achieve this transformation is to use the *inverse method* [20, 21]. This method relies on the fact that a random variable of any distribution can be expressed as a function of another random variable that is uniformly distributed between zero and one. To use this method the probability function $p(x)$ must be normalized and nonzero everywhere within its domain of definition. Then its corresponding cumulative function $P(x)$ will be monotonically increasing from zero to one and therefore invertible. $P(x)$ is given by

$$P(x) = \int_{-\infty}^{x} p(x')dx'. \tag{3.1}$$

$P(x)$ is itself a random variable, distributed uniformly between zero and one. Therefore a random number x with distribution $p(x)$ might be found by selecting a uniform random number ρ and solving the following equation

$$\rho = P(x) \Rightarrow x = P^{-1}(\rho).$$

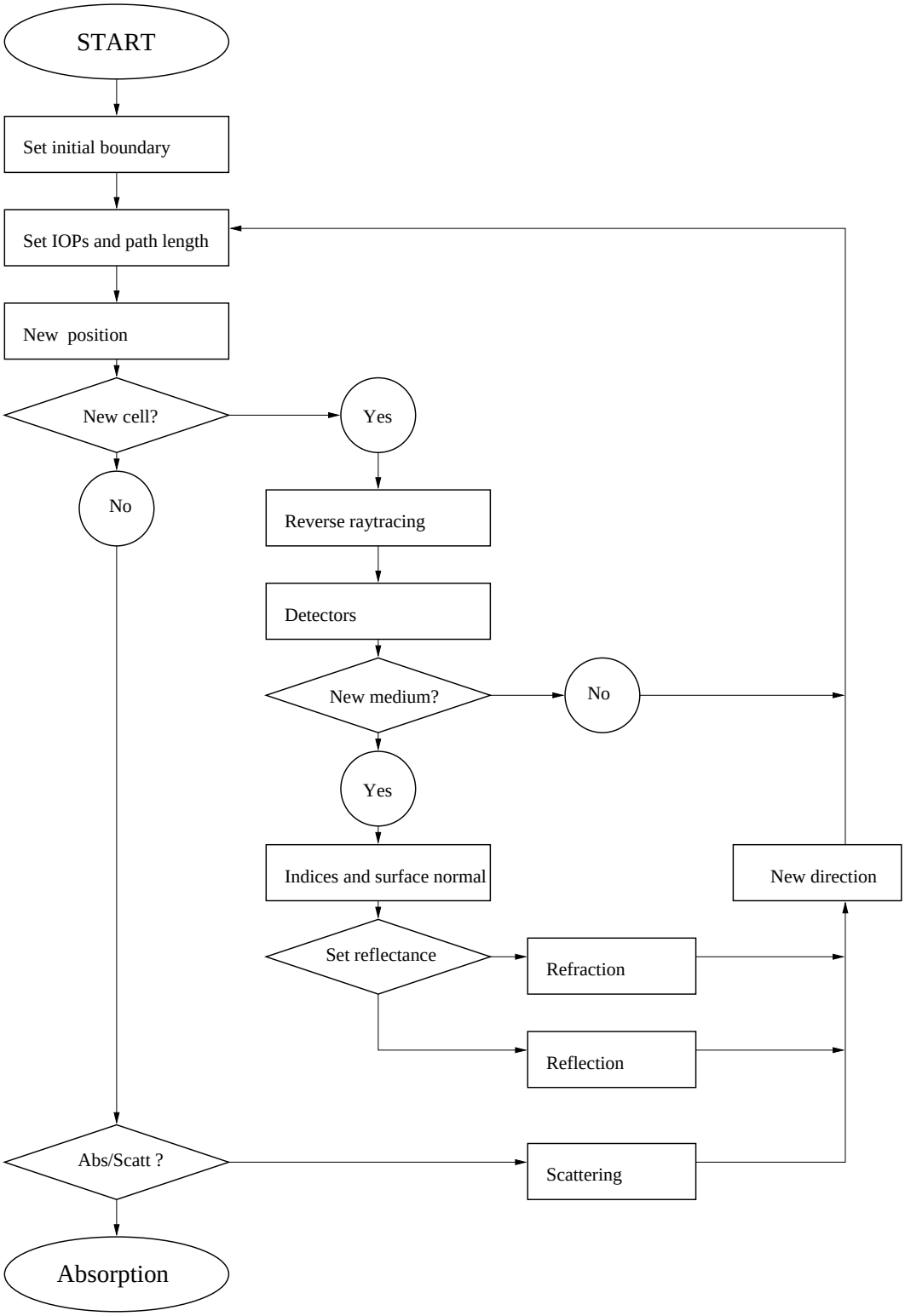

Figure 3.2: Flow chart of the Monte Carlo program. Every photon follows this path from it is launched at the top of the atmosphere until it is absorbed somewhere in the atmosphere or in the ocean or it escapes back to space.

The required condition to use this method is that the probability function $p(x')$ in Eq. (3.1) is invertible; otherwise this method is not suitable.

3.2.1 Path length

Light traveling in a medium that contains absorbers or scatterers will be attenuated according to the extinction law in Eq. (1.8). When we normalize this function, we find that $\Phi^i = c$, which gives

$$\Phi_{normalized} = ce^{-cs}.$$

The corresponding cumulative function becomes

$$P(s) = \int_0^s ce^{-cs'}\, ds' = 1 - e^{-cs}$$

which leads to

$$s = -\frac{\ln(1-\rho)}{c} \tag{3.2}$$

where $P(s)$ has been replaced by ρ. If ρ is a random number uniformly distributed between zero and one, so is $(1-\rho)$. Therefore it follows from Eq. (3.2) that

$$s = -\frac{\ln(\rho)}{c} \tag{3.3}$$

where s is the path length of a photon in a medium with attenuation coefficient c as a function of a random number $\rho \in [0,1]$. Note that s is the path length in any direction, so that the the optical depth is $cs/\cos\theta = cz$.

3.2.2 Roughness of the sea surface

When a plane electromagnetic wave is refracted and reflected at a plane interface, the direction of the reflected and refracted waves are given by the reflection law and Snell's law, i. e.

$$\theta_i = \theta_r \text{ and } \phi_i = \phi_r$$

and

$$n_1 \sin\theta_i = n_2 \sin\theta_t \text{ and } \phi_i = \phi_t$$

where θ_i, θ_r, and θ_t are the angles of the incident, reflected, and transmitted wave vectors relative to the interface normal, respectively, ϕ_i, ϕ_r, and ϕ_t are the azimuth angles for the incident, reflected, and transmitted wave vectors, respectively, and n_1 and n_2 are the indices of refraction of the two media, see fig. 3.3. Since the surface of the ocean is not plane, but rough, it is necessary,

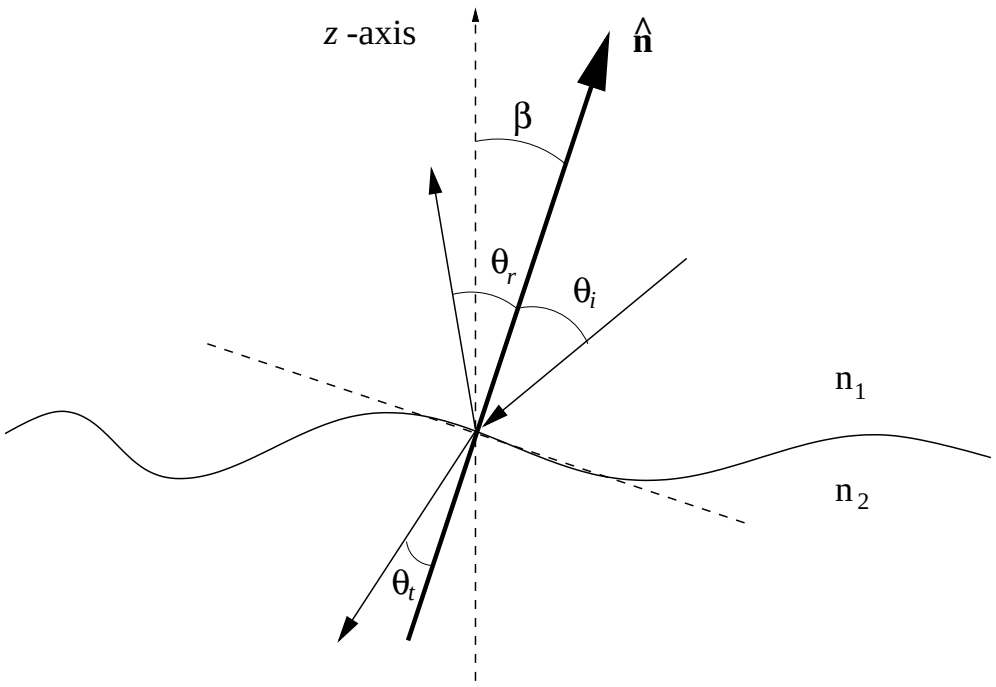

Figure 3.3: Normal vector $\hat{\mathbf{n}}$ of a rough sea surface.

when running a Monte Carlo routine, to find a probability function for the normal vector $\hat{\mathbf{n}}$ of the surface. The components of the normal vector $\hat{\mathbf{n}}$ may be written

$$n_x = \cos\alpha \sin\beta, \;\; n_y = \sin\alpha \sin\beta, \;\; n_z = \cos\beta \tag{3.4}$$

where α is the azimuth angle. It is uniformly distributed in the interval from 0 to 2π, so that

$$\alpha \;=\; 2\pi\rho_1 \tag{3.5}$$

where ρ_1 is a random number in the interval [0,1]. β is the angle between $\hat{\mathbf{n}}$ and the vertical direction which is along the z axis in the global coordinate system in fig. 3.3. The tilt angle β is determined from the probability density function given by Cox and Munk [22], i. e.

$$p(\beta) \;=\; e^{\frac{-\tan^2\beta}{\sigma^2}} \tan\beta \sec^2\beta \tag{3.6}$$

where

$$\sigma \;=\; \sqrt{0.003 + 0.00512V} \tag{3.7}$$

is the rms slope of the ocean surface with V being the wind speed in any direction. When we normalize Eq. (3.6), the cumulative function $P(\beta)$ becomes

$$P(\beta) \;=\; \frac{2}{\sigma^2} \int_0^{\beta} e^{\frac{-\tan^2\beta'}{\sigma^2}} \tan\beta' \sec^2\beta' \, d\beta'. \tag{3.8}$$

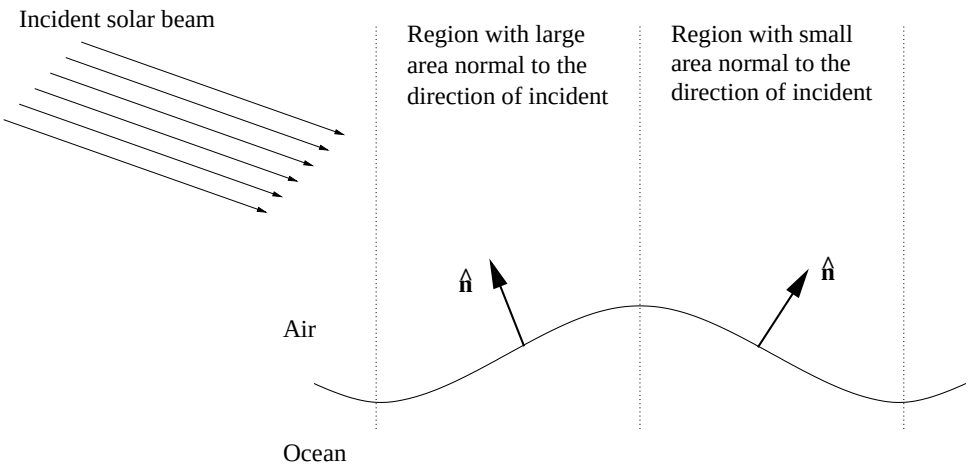

Figure 3.4: Distribution of photons over one water wave period.

By the substitution $u = -(\tan^2 \beta')/\sigma^2$, we obtain from Eq. (3.8)

$$P(\beta) = -\int_0^{-\frac{\tan^2\beta}{\sigma^2}} e^u \, du = 1 - e^{-\frac{\tan^2\beta}{\sigma^2}}$$

which gives

$$\beta = \tan^{-1}\left(\sqrt{-\sigma^2 \ln(1-\rho_2)}\right) = \tan^{-1}\left(\sqrt{-\sigma^2 \ln \rho_3}\right). \tag{3.9}$$

In Eq. (3.9) the cumulative function $P(\beta)$ is replaced with the random number ρ_2. The last equation follows from the fact that when ρ_2 is a random number uniformly distributed in the range from 0 to 1, so is $\rho_3 = 1 - \rho_2$. Thus, the direction of the normal vector $\hat{\mathbf{n}}$ of a rough sea surface is given by Eqs. (3.4), (3.5), and (3.9). Note that if the wind speed $V = 0$, there will still be surface facets. To obtain a plane surface with Cox and Munk's formula σ must be zero, or eiuvalently $V \approx -0.59$ (see Eqs. (3.7) and (3.9)).

When a collection of photons hits the water surface from an oblique angle the distribution of photons over a wave period is not uniform. As shown in fig. 3.4, the photon density is higher on the side of the wave where the normal vector $\hat{\mathbf{n}}$ is tilted towards the direction of the incoming photons. The development of a function for the photon distribution over a wave period, with the amplitude of the wave and the angle of incidence as arguments, will require complicated mathematics. An adequate approximation is to let all photons hit that quadrant in which both the x component and the y component of the normal vector have opposite signs compared to the signs of the x component and the y component of the incident solar beam, see fig. 3.5. In this approximation we simply assume

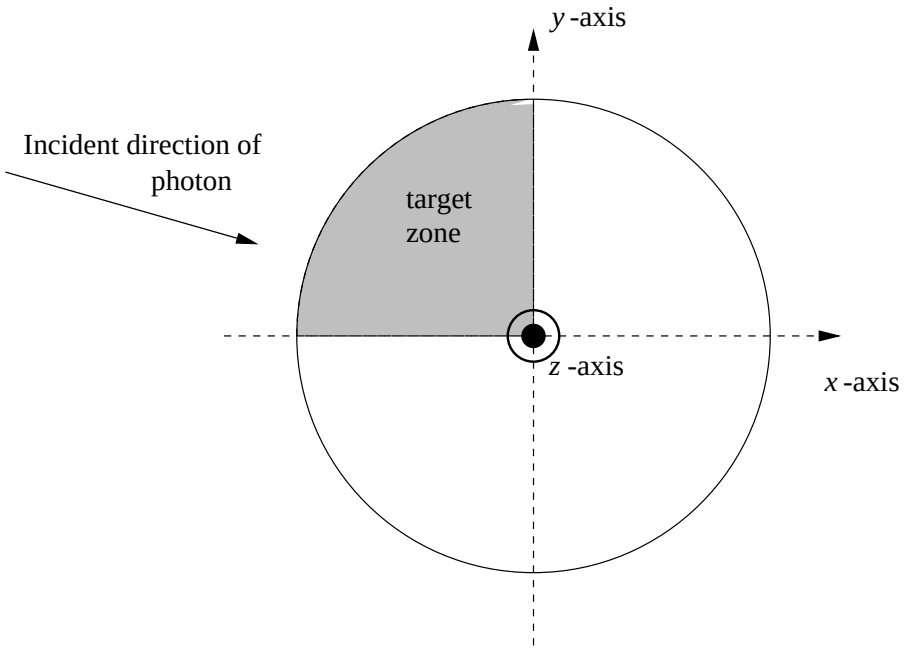

Figure 3.5: If the wave surface were circular, the photons would hit the wave surface within the gray target zone.

that the three other quadrants lie completely in the shade. This assumption also prevents any multiple reflections between facets which could occur when the zenith angle and the facet slope are large. However, the probability for this event to happen is very small and the tests results of Jin and Simpson [23] indicate that the error caused by ignoring this effect is less than 1% for a zenith angle of 70°.

3.2.3 Henyey-Greenstein scattering function

As mentioned in section 1.1.1, we use the Henyey-Greenstein phase function given in Eq. (1.13) in Monte Carlo simulations of scattering on algae and other particles. Inserting this equation into Eq. (1.12), we get

$$4\pi \;=\; 2\pi \int_0^{\pi} \frac{1-g^2}{(1+g^2-2g\cos\theta)^{3/2}}\,\sin\theta\,d\theta. \tag{3.10}$$

It is necessary to set the left hand side of Eq. (3.10) equal to 4π, since the photons are scattered over all solid angles. Substituting $\cos\theta = x'$ and $\sin\theta\; d\theta = -dx'$, and transforming the integration boundaries $\cos 0 = 1$ and $\cos\pi = -1$, we obtain

$$1 \;=\; -\frac{1}{2}\int_1^{-1} \frac{1-g^2}{(1+g^2-2gx')^{3/2}}\,dx'. \tag{3.11}$$

After switching the integration limits and the sign, we replace the upper limit of integration by x, so that the left hand side of Eq. (3.11) becomes equal to $P(x) \in [0, 1]$. Hence we obtain the normalized cumulative function

$$P(x) = \frac{1}{2} \int_{-1}^{x} \frac{1 - g^2}{(1 + g^2 - 2gx')^{3/2}} \, dx'$$

which we need for the simulations. Performing the integration, we get

$$P(x) = \frac{1 - g^2}{2g} \left(\frac{1}{\sqrt{1 + g^2 - 2gx}} - \frac{1}{1 + g} \right).$$

The inverted function is

$$x = \frac{1 + g^2}{2g} - \frac{(1 - g^2)^2}{2g(2g\rho + 1 - g)^2} \tag{3.12}$$

where $P(x)$ has been replaced by the random number ρ. This result is also given by Groenhuis et al. [24] and Lotsberg [25].

3.2.4 Rayleigh scattering function

For scattering on molecules in the atmosphere and in the water we use the Rayleigh scattering phase function given in Eq. (1.16). Again we combine this equation with Eq. (1.12) and get

$$4\pi = 2\pi \frac{3}{3 + p} \int_{0}^{\pi} (1 + p \cos^2 \theta) \sin \theta \, d\theta.$$

Using the same substitution as for the Henyey-Greenstein scattering function ($\cos \theta = x'$ and $\sin \theta \, d\theta = -dx'$), we get

$$1 = \frac{3}{2(3 + p)} \int_{-1}^{1} (1 + px'^2) \, dx'.$$

Again we replace the upper integration limit by x and the left hand side by $P(x)$ and get

$$\begin{aligned} P(x) &= \frac{3}{2(3 + p)} \int_{-1}^{x} (1 + px'^2) \, dx' \\ &= \frac{3}{2(3 + p)} \left(x + \frac{px^3}{3} + 1 + \frac{p}{3} \right). \end{aligned}$$

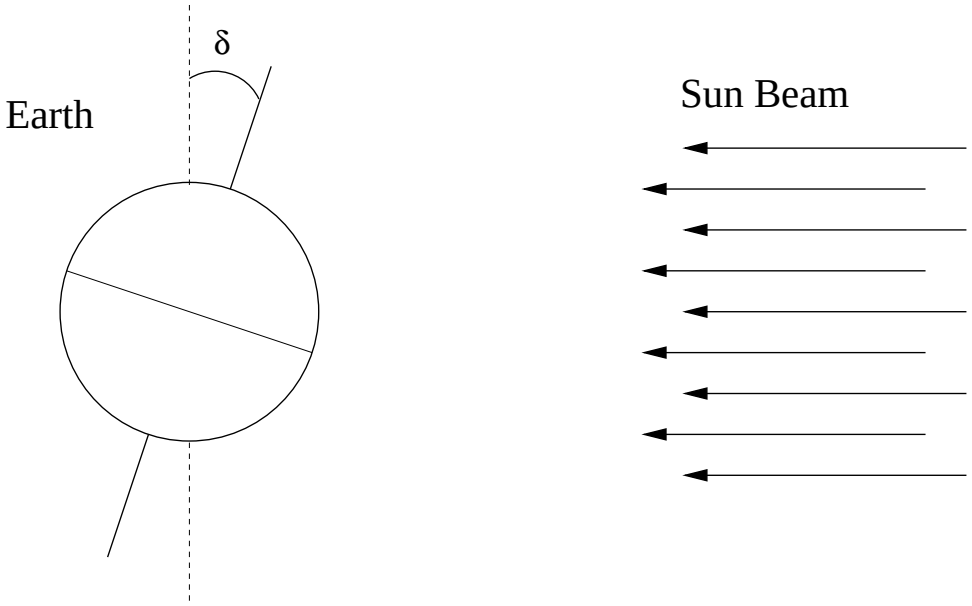

Figure 3.6: Definition of the solar declination δ.

Finally, we replace $P(x)$ by the random number ρ to obtain

$$px^3 + 3x + (3+p)(1-2\rho) \;=\; 0. \tag{3.13}$$

Eq. (3.13) is a polynomial of the third degree in x, and we choose to solve it numerical by using *the secant method* [26]. This method has an order of convergence of approximately 1.6[1] and usually finds the root to an accuracy of 10^{-6} within 5 iterations. For each random number $\rho \in [0,1]$ there is a corresponding polar scattering angle $\theta = \arccos x$.

3.3 The solar zenith angle

One important input to atmospheric and marine optics is the zenith angle θ_0 of the direct solar beam. The zenith angle varies from $\pi/2$ (or its maximum value in the polar regions in the summer) to its minimum value and increases symmetrically to $\pi/2$ (or its maximum value). The variation of the zenith angle during a day depends on the latitude and the solar declination δ. The declination is the angle the axis of the Earth is tilted towards the sun. It is negative for the case in which the axis of the Earth is tilted away from the sun, see fig. 3.6. The

[1]A iterative method has the order of convergence p if $\lim_{i\to\infty} \frac{E_{i+1}}{(E_i)^p} = C$, where C is a constant and E_i is the error after the ith iteration. So a good iterative method has a large order of convergence.

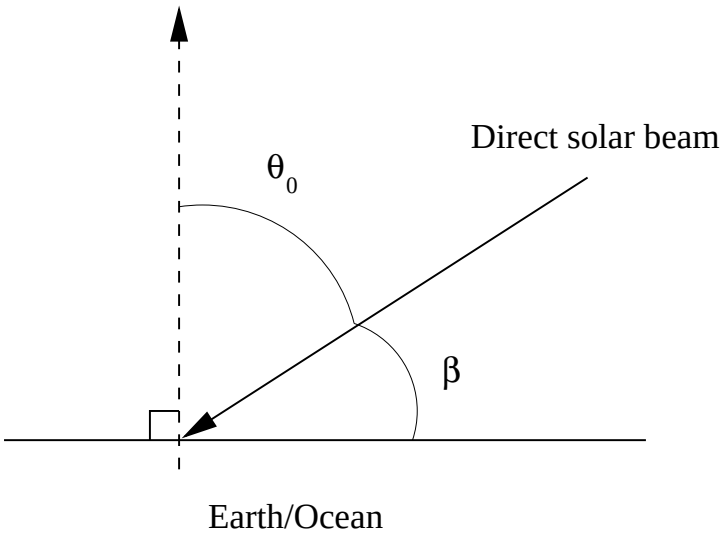

Figure 3.7: Relation between zenith angle θ_0 and solar elevation β.

extreme values of the declination is $\pm 23°27'$. The declination for a given day of the year is given by Kirk [27],

$$\begin{aligned} \delta &= (0.39637 - 22.9133\cos\psi + 4.02543\sin\psi \\ &\quad -0.3872\cos 2\psi + 0.052\sin 2\psi)2\pi/360. \end{aligned} \tag{3.14}$$

Here $\psi = 2\pi\, d\,/365$ is the date expressed as an angle with d being the day number ranging from 0 to 364. Both δ and ψ in Eq. (3.14) are expressed in radians. The zenith angle θ_0 at a given latitude γ and date ψ is a function of the local time t expressed as an angle τ given by $\tau = 2\pi\, t/24$. Thus

$$\begin{aligned} \cos\theta_0 &= \sin\gamma\sin\delta - \cos\gamma\cos\delta\cos\tau \\ &= c_1 - c_2\cos\tau. \end{aligned} \tag{3.15}$$

The solar elevation β is complementary to the zenith angle θ_0, i. e. $\theta_0 + \beta = \pi/2$. Hence $\sin\beta = \cos\theta_0$, see fig 3.7. Eq. (3.15) shows that the cosine of the zenith angle has a sinusoidal variation with time. In fig. 3.8 the cosine of the zenith angle and the solar elevation are plotted for the longest summer day and the shortest winter day at the latitude of 60°.

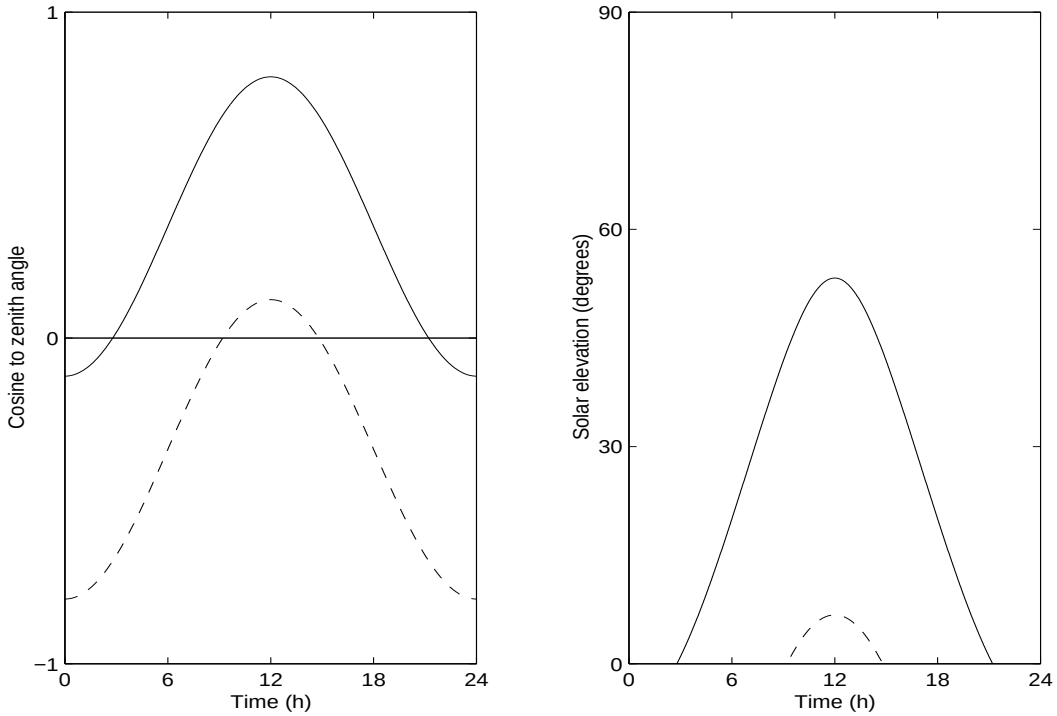

Figure 3.8: Left: Cosine of the zenith angle $\cos\theta_0$ (or sinus of the solar elevation $\sin\beta$) plotted against a 24 hour period at a latitude of 60°. The solid line corresponds to the longest summer day while the dashed line corresponds to the shortest winter day. The values of $\cos\theta_0$ are also plotted during the hours of darkness. The negative values correspond to angles at which the sun is below the horizon. Right: The corresponding solar elevations β plotted only for hours of day light.

Chapter 4

Results

To be able to draw conclusions based on results from the MC routine it is necessary to test it. In this chapter we test it against known results from the literature and against results from the DISORT routine.

4.1 Single finite slab

As a simple test of the routine we may consider a single slab with uniform isotropic scattering. This case was calculated analytically by van de Hulst [28]. Given the optical depth τ and the single scattering albedo ω_0 of the slab and assuming an energy flow of 10,000 units falling normally on the surface of the slab it is easy to test results from MC and DISORT code against corresponding tabulated values given by van de Hulst [28]. The results are shown in Table. 4.1 for different values of τ and ω_0. As we can see, the error of the DISORT routine is always less than 0.1% and the error of the MC routine is within the range of 0.5% relative to the results achieved by van de Hulst. Note that the local error grows as the single scattering albedo ω_0 gets larger.

4.2 Simple atmosphere ocean system

Next we apply the MC routine to a one-dimensional geometry in order to get results that may be compared directly with results from the one-dimensional DISORT routine. Since the DISORT routine does not include any roughness of the sea surface, we must use the same conditions in the Monte Carlo model. In the first test case we use a chlorophyll concentration in the ocean of 0.02 mg/m^3. The chlorophyll is uniformly distributed from the surface to the bottom. We

Optical depth $\tau = 1.6$, single scattering albedo $\omega_0 = 0.2$

	v. d. Hulst	DISORT	Error (%)	MC	Error (%)
Reflected	344	344	0.0	344	0.0
Absorbed	7,447	-	-	7,447	0.0
Transmitted	2,209	2,209	0.0	2,209	0.0

Optical depth $\tau = 1.6$, single scattering albedo $\omega_0 = 1.0$

	v. d. Hulst	DISORT	Error (%)	MC	Error (%)
Reflected	4,587	4,590	0.07	4,579	0.09
Absorbed	0	-	-	0	0.0
Transmitted	5,413	5,417	0.07	5,421	0.15

Optical depth $\tau = 2$, single scattering albedo $\omega_0 = 0.9$

	v. d. Hulst	DISORT	Error (%)	MC	Error (%)
Reflected	3,616	3,616	0.0	3,620	0.11
Absorbed	2,819	-	-	2,806	-0.46
Transmitted(dir)	1,353	1,353	0.0	1,354	0.07
Transmitted(dif)	2,212	2,212	0.0	2,220	0.36
Transmitted(sum)	3,565	3,565	0.0	3,574	0.25

Optical thickness $\tau = 2.5$, single scattering albedo $\omega_0 = 1.0$

	v. d. Hulst	DISORT	Error (%)	Monte Carlo	Error (%)
Reflected	5,760	5,761	0.02	5,751	0.16
Absorbed	0	-	-	0	0.0
Transmitted	4,240	4,240	0.0	4,249	0.21

Table 4.1: Energy flow through a slab. The MC code was run with 10^8 photons and the DISORT code was run with 16 streams. The error for MC or DISORT is the relative error compared to the results found by van de Hulst.

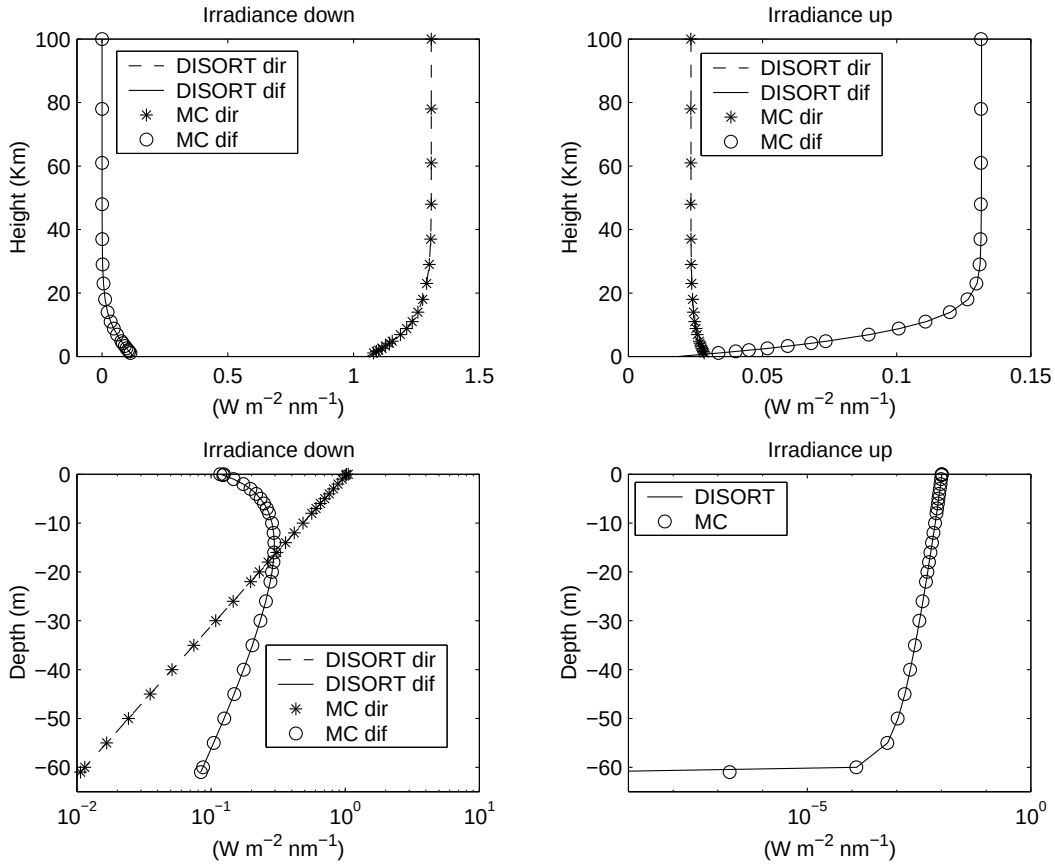

Figure 4.1: Irradiance in the atmosphere (upper panels) and in the ocean (lower panels) computed by the DISORT routine (solid and dashed lines) and the MC routine (circles and stars). The graphs show both the direct and the diffuse irradiance.

assume that there is only Henyey-Greenstein scattering in the ocean and isotropic scattering in the atmosphere. This is not realistic, but makes nevertheless a good case for comparing results from the MC routine with results from the DISORT routine. Based on the chlorophyll concentration, one can compute the absorption and scattering coefficients a and b and the asymmetry factor g for the Henyey-Greenstein scattering function. Exactly the same input is used for the MC and DISORT routines. Thus, we expect identical results from the two routines. The atmosphere is set to a height of 100 km and the ocean to a depth of 61 m, with a black bottom. The zenith angle is set to be 45°, and the indices of refraction $n_{atm} = 1$ and $n_{ocn} = 1.33$. Results for the irradiance are plotted in fig. 4.1, and results for the scalar irradiance are plotted in fig. 4.2. The relative deviation

$$100 \times \frac{(MC - DISORT)}{DISORT}$$

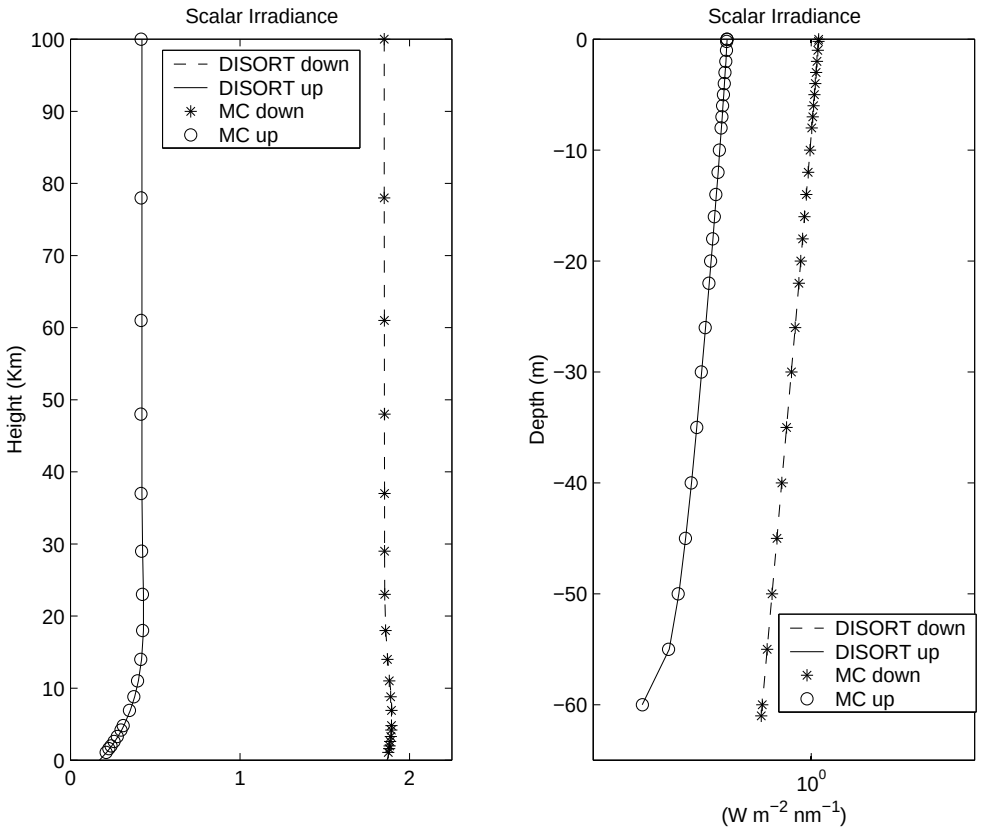

Figure 4.2: Scalar irradiance in the atmosphere (left) and in the ocean (right) computed by the DISORT routine (solid and dashed lines) and the MC routine (circles and stars).

is plotted in figs. 4.3 and 4.4. The MC code was run with 10^8 photons, while the DISORT code was run with 32 streams. For the downward irradiances the disagreement is less than 1% almost everywhere, while it is less than 2% for the upward irradiances. It make sense that the relative disagreement is larger in the upward direction because there are less photons traveling upwards, and hence any absolute disagreement will have a larger relative value in this case. Even though we try to make all conditions identical for the two models there are some differences that we cannot avoid. We have shown that the MC code uses two different scattering phase functions (Henyey-Greenstein and Rayleigh) and that the scattering angle is found by the inverse method (Eqs. (3.12 and 3.13)). The DISORT code, however, expresses the scattering phase function in terms of Legendre polynomials. We have seen that the phase function for Rayleigh scattering can be perfectly expressed with three polynomials, but for Henyey-Greenstein scattering we need an infinite number of polynomials to obtain a perfect description of the phase function. The HG phase function in the DISORT code is therefore

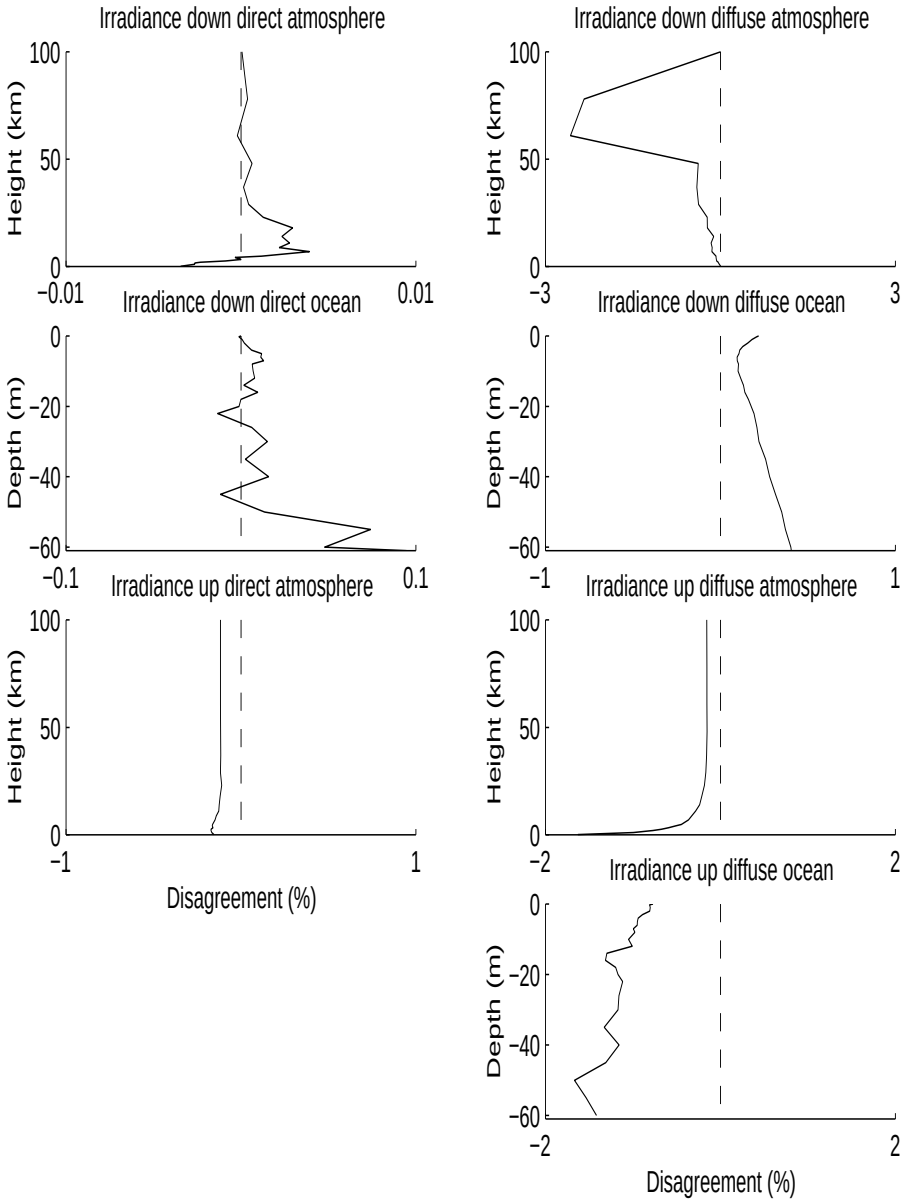

Figure 4.3: Disagreement between the MC and DISORT routines for irradiances. Upper row: Irradiance in the downward direction in the atmosphere, direct beam (left) and diffuse light (right). Second row from above: Irradiance in the downward direction in the ocean, direct beam (left) and diffuse light (right). Third row from above: Irradiance in the upward direction in the atmosphere, direct beam (left) and diffuse light (right). Bottom row: Irradiance in the upward direction in the ocean, diffuse light only.

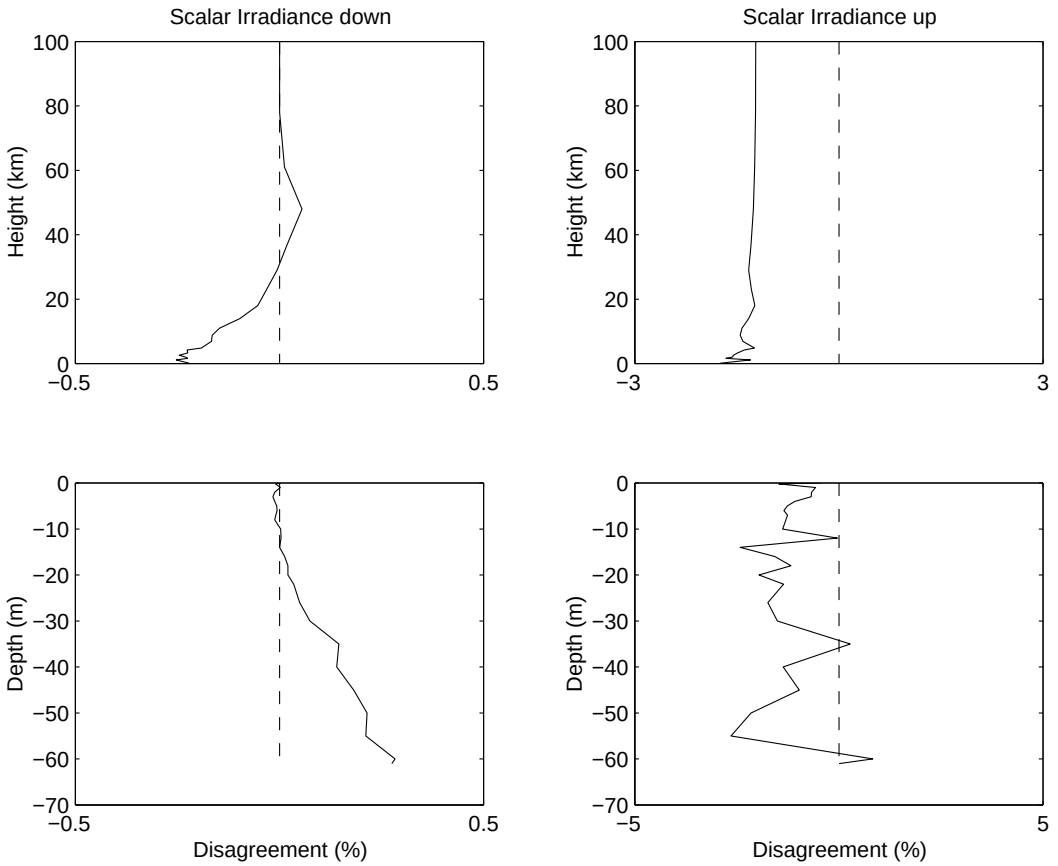

Figure 4.4: Disagreement between the MC and DISORT routines for the scalar irradiance. Upper left: Scalar irradiance downward in the atmosphere. Upper right: Scalar irradiance upward in the atmosphere. Lower left: Scalar irradiance downward in the ocean. Lower right: Scalar irradiance upward in the ocean.

approximated by a finite number of polynomials. If the asymmetry factor is close to one, we need a large number of Legendre polynomials to express the HG phase function with acceptable accuracy, see fig. 6.1 in Thomas and Stamnes [1]. The number of phase moments that are used in the DISORT code is limited by the number of streams that is used. Fig. 4.5 shows the significance of the number of streams in the DISORT code. In the figure the disagreement in the diffuse upward irradiance in the atmosphere between the two codes is plotted against the altitude. This diffuse irradiance is chosen as an example since the disagreement here is bigger than for the other irradiances. As the number of streams increases from 2 to 32 the disagreement between the MC code and the DISORT code decreases considerably. At the sea level the 2 stream solution of DISORT gives a disagreement of 52.4% while the 32 stream solution only gives a disagreement of

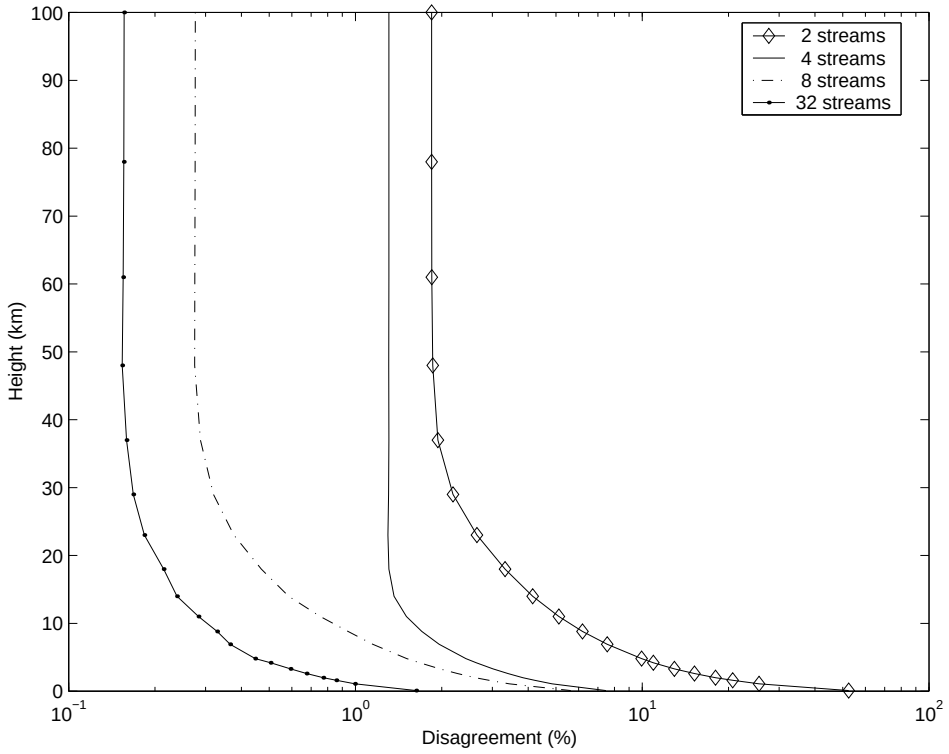

Figure 4.5: The absolute value of the disagreement between the MC and DISORT routine for upward diffuse irradiance in the atmosphere. We see how the disagreement is reduced as the DISORT code is run with a larger number of streams.

1.63%. The corresponding disagreements at the top of the atmosphere (100 km) are 1.84% and 0.16%, respectively. It turns out that the DISORT routine for a coupled atmosphere-ocean system converges when 16 streams are used in the program.

4.2.1 Effect of surface facets

In the example above we used a plane water surface in the MC routine to run the code with exactly the same interface conditions as the DISORT code. However, one of the advantages of the MC code is that it is possible to study also effects of surface waves. We will now examine how the disagreement between the two codes grows as surface waves are included. The previous example was repeated with the effects of surface waves included in accordance with the Cox and Munk formula (Eq. (3.6)). The wind speed in the formula was set to $V = 0, 6, 12\ ms^{-1}$.

For comparison we choose three altitude levels in the coupled atmosphere-ocean system, one at the top of the atmosphere (TOA), another right above the

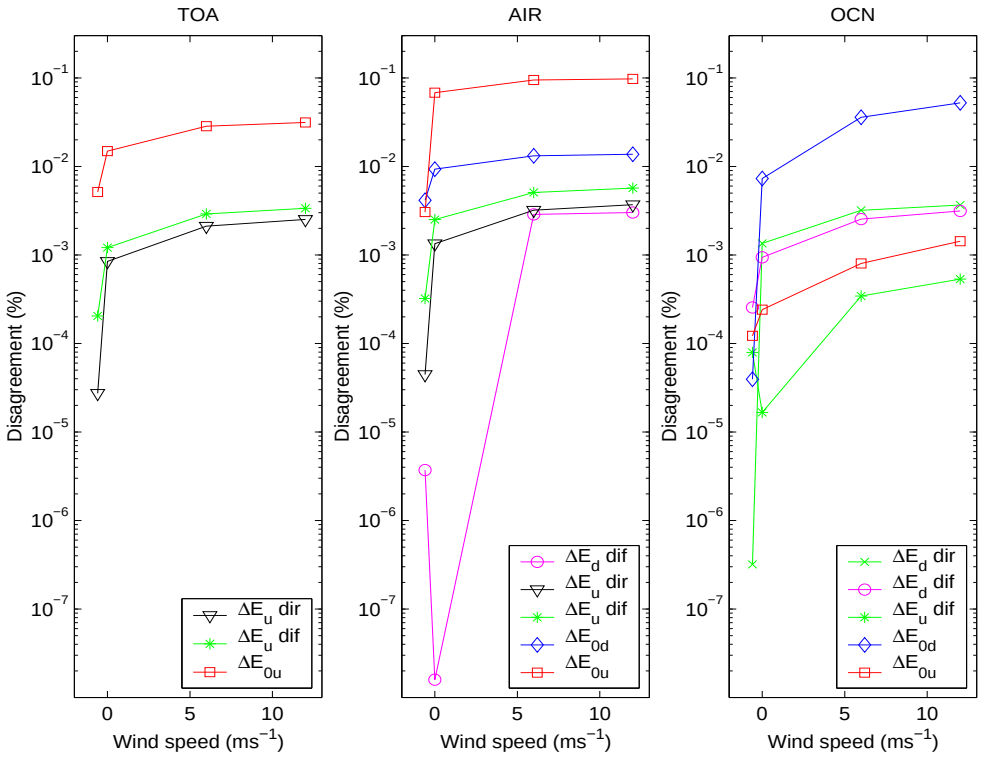

Figure 4.6: The disagreement between MC and DISORT grows as surface facets are included in the MC model. The values to the left in each figure are for the case with no surface waves, the next values are for a wind speed of 0 ms^{-1}, 6 ms^{-1}, and 12 ms^{-1}, respectively.

water surface (AIR) and a third right beneath the water surface (OCN). The difference between results from the MC and DISORT codes for each irradiance is defined as follows.

$\Delta E_d dir$ Difference for the direct downward irradiances.

$\Delta E_d dif$ Difference for the diffuse downward irradiances.

$\Delta E_u dir$ Difference for the direct upward irradiances.

$\Delta E_u dif$ Difference for the diffuse upward irradiances.

ΔE_{0d} Difference for the scalar downward irradiances.

ΔE_{0u} Difference for the scalar upward irradiances.

In fig. 4.6 we see how the differences ΔE_i increase as the wind speed increases. Note that the left most values are set to the artificial wind speed $V = -0.5859\, ms^{-1}$

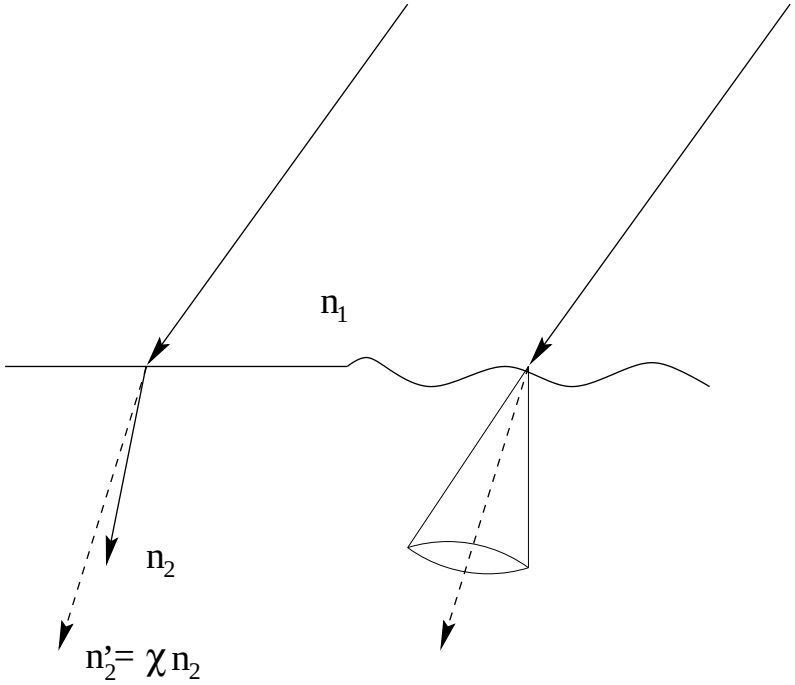

Figure 4.7: By changing the index of refraction of the ocean in the DISORT routine we achieve better agreement with the MC routine when the wind speed is nonvanishing.

which gives $\sigma^2 = 0$ in Cox and Munk's formula Eq. (3.7) and hence a plane surface. All units are in $[Wm^{-2}]$.

Even though the DISORT code cannot handle surface waves, it is possible to modify the index of refraction so that the results get closer to those of the MC code with surface waves included. The roughness of the surface makes the average angle of incidence smaller than it would be in the case of a plane surface (fig. 3.3). Hence, the angle between the z-axis and the average direction of the photons after refraction is larger in the case of a rough surface. One way to account for this difference is to change the index of refraction in the DISORT code so that the refracted beam has the same direction as the average direction of the photons in the MC code, see fig. 4.7. By using Snell's law, we find

$$\begin{aligned} n_2' &= \chi n_2 \\ \chi &= \frac{n_1 \sin\theta_0}{n_2 \sin(\arccos\overline{\mu}')} \end{aligned} \tag{4.1}$$

where $\overline{\mu}'$ is the average cosine of the polar angle just beneath the surface. In the example where the wind speed was set to 12 ms^{-1} the MC code gives $\overline{\mu} = 0.819$ and $\chi = 0.93$ for $n_2 = 1.33$ and $\theta_0 = 45°$. Fig. 4.8 and fig. 4.9 show the relative difference for two cases with surface roughness corresponding to a wind speed of

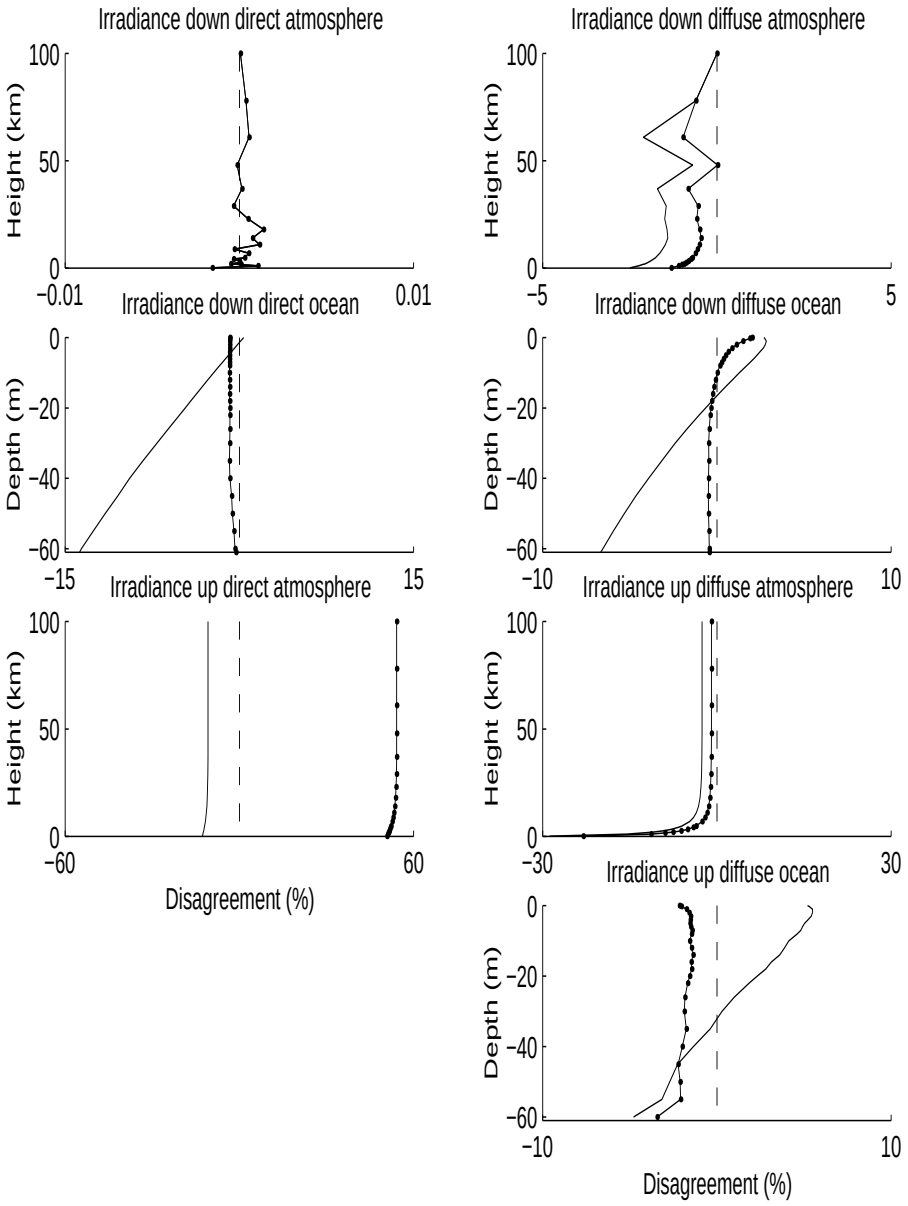

Figure 4.8: Disagreement between the MC and DISORT codes for the irradiances. The MC code is run with a wind speed of 12 ms^{-1}. The DISORT code is unchanged for the solid line and modified with index of refraction for the line with dots. Upper row: Irradiance in the downward direction in the atmosphere, direct beam (left) and diffuse light (right). Second row from above: Irradiance in the downward direction in the ocean, direct beam (left) and diffuse light (right). Third row form above: Irradiance in the upward direction in the atmosphere, direct beam (left) and diffuse light (right). Bottom row: Irradiance in the upward direction in the ocean, diffuse light.

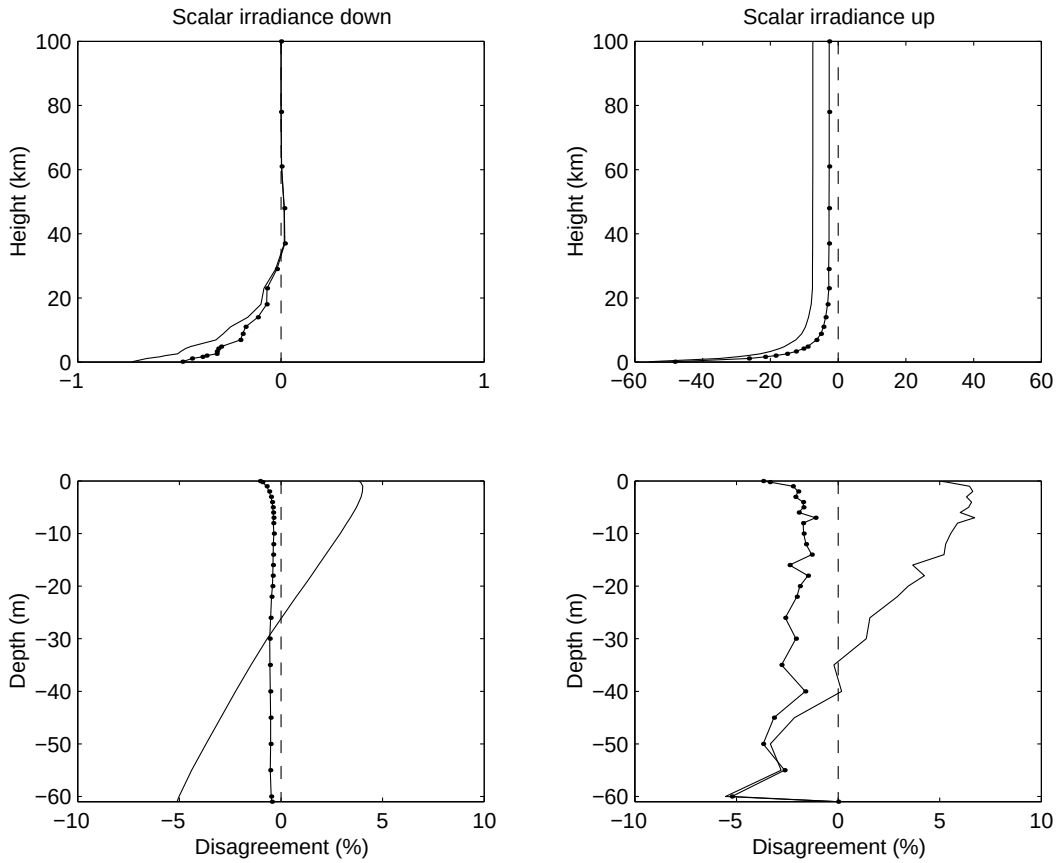

Figure 4.9: Disagreement between the MC and the DISORT codes for the scalar irradiances. the MC code was run with a wind speed of $12 ms^{-1}$. The DISORT code is unchanged for the solid line, whereas the index of refraction is modified for the line with dots. Upper left: Scalar irradiance downward in the atmosphere. Upper right: Scalar irradiance upward in the atmosphere. Lower left: Scalar irradiance downward in the ocean. Lower right: Scalar irradiance upward in the ocean.

$V = 12\ ms^{-1}$. In the first case (solid line) the refractive index in the DISORT code is unchanged, while in the second case (solid line with dots) the refractive index in the DISORT code is given by $n_2' = \chi\ n_2$ in accordance with Eq. (4.1). As we see, this refractive index change improves all results except those for the direct upward irradiance in the atmosphere. Especially in the deeper layer of the ocean this modification gives a significantly better result. Fig. 4.10 shows how χ depends on the wind speed V and the zenith angle θ_0. Considering the discrete values from the MC code (squares), we assume that χ can be approximately expressed

$$\chi(V, \theta_0) \approx aV^2 + b\theta_0^2 + cV + d\theta_0 + e.$$

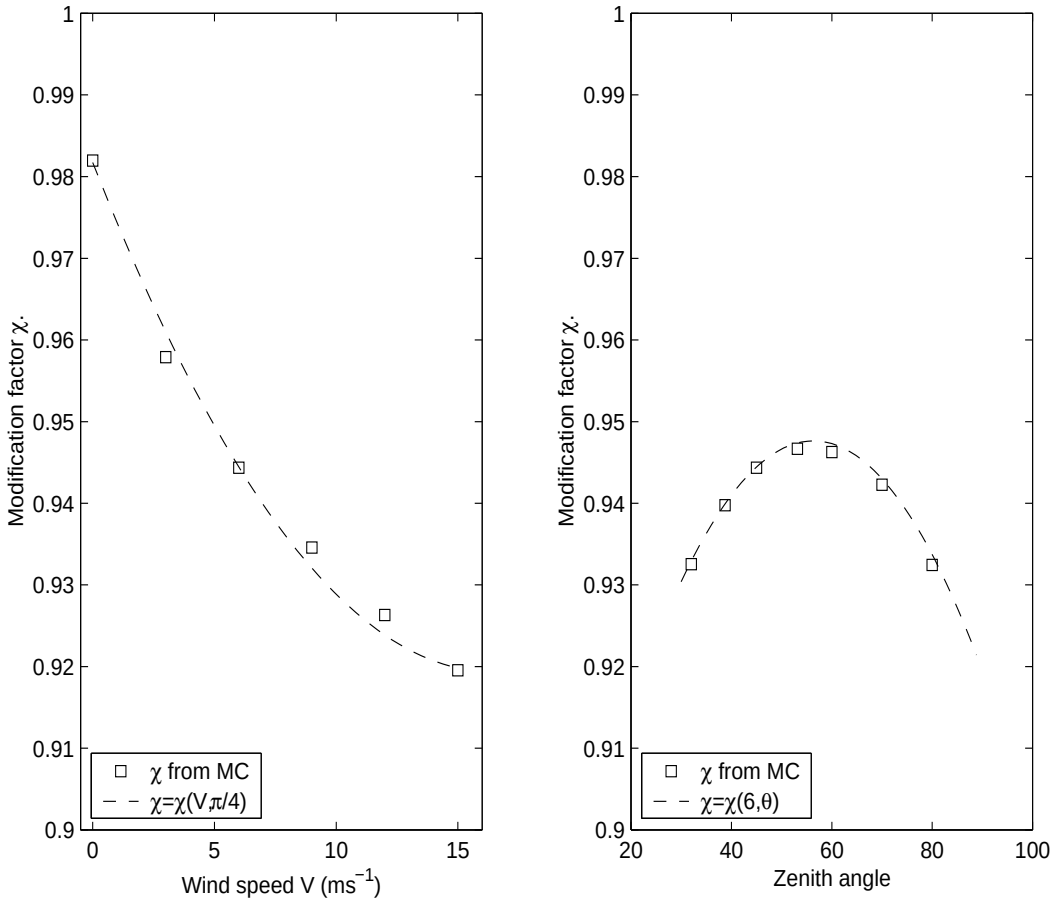

Figure 4.10: The modification factor χ as a function of the wind speed V and the zenith angle θ_0. Left: The zenith angle is fixed at $\theta_0 = 45°$. Right: The wind speed is fixed at $V = 6\ ms^{-1}$.

To find the coefficients we may use a least-squares approximation. Then we find

$$\begin{aligned}\chi(V,\theta_0) \;\approx\; & 2.3192\cdot 10^{-4}V^2 - 2.48694\cdot 10^{-5}\theta_0^2 \\ & -7.60397\cdot 10^{-3}V + 2.80213\cdot 10^{-3}\theta_0 + 0.905982 \qquad (4.2)\end{aligned}$$

for values of V and θ_0 in the intervals $V \in [0, 15]$ and $\theta_0 \in [35°, 80°]$. In this approximation the index of refraction was modified so as to obtain a correct average direction for the refracted photons in the ocean. No attempt were made to correct the average direction of the reflected light or to correct the ratio between the transmitted and the reflected energy. We would get a better approximation if we correct the average directions of both the transmitted and the reflected light. These directions are found from the results from the MC code with different input for the zenith angle and wind speed. We may approximate these directions as a polynomial function of the wind speed and the zenith angle. By using a

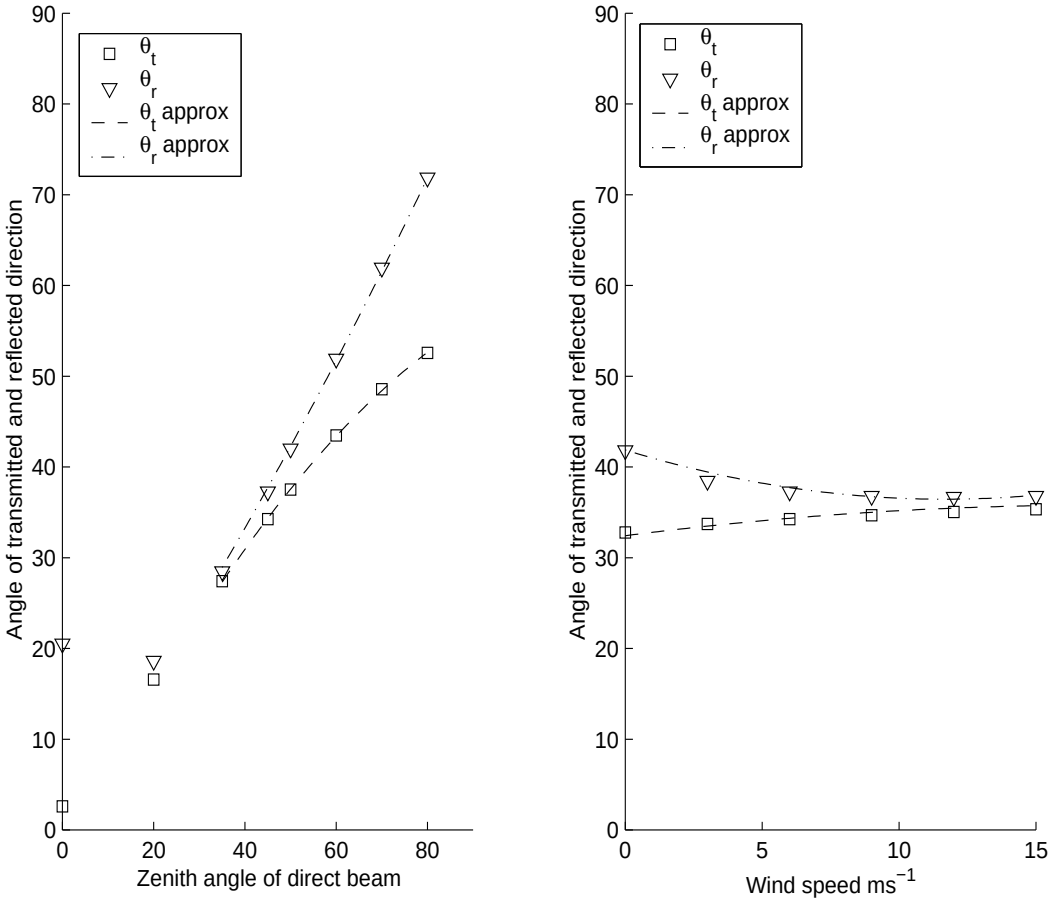

Figure 4.11: Approximation for the average transmitted and reflected direction in the case of a rough surface. The average directions have been approximated in the $V\theta_0$-plane. Left: True and approximate values for a fixed wind speed $V = 6\ ms^{-1}$. Right: True and approximate values for a fixed zenith angle $\theta_0 = 45°$.

least-squares approximation, we then find

$$\begin{aligned} \overline{\theta}_t &\approx -1.10985 \cdot 10^{-2} V^2 - 4.02809 \cdot 10^{-3} \theta_0^2 \\ &\quad +0.387023\, V + 1.02599\, \theta_0 - 5.5891 \qquad (4.3) \\ \overline{\theta}_r &\approx 3.98771 \cdot 10^{-2} V^2 + 2.09377 \cdot 10^{-3} \theta_0^2 \\ &\quad -0.930259\, V + 0.713428\, \theta_0 + 5.53015 \qquad (4.4) \end{aligned}$$

for values of V and θ_0 in the intervals $V \in [0, 15]$ and $\theta_0 \in [35°, 80°]$, see fig. 4.11. It turned out to be difficult to find good polynomial approximations when the zenith angle is less than 35°. To include these approximations in the DISORT routine is not so simple as the modification of the index of refraction considered earlier. It requires a number of changes in the code and related book keeping.

4.2.2 Calculating AOPs

In this section an example of the AOPs is calculated from the results obtained with the MC code. The input IOPs are calculated based on a chlorophyll content of 0.35 mg/m^3 in all layers. The zenith angle is 0° or 80° in the atmosphere and the surface was either without waves at all or had a roughness caused by a wind speed of 7.5 ms^{-1}. The case was tested for the four combinations of the zenith angle and the surface waves. Remember that the cases in which there are no surface waves is *not* the same as using a wind speed of 0 ms^{-1} in the formula developed by Cox and Munk, see Eq. (3.6). The diffuse attenuation coefficient K_d is evaluated by solving Eq. (1.23) for K_d. Thus, from

$$E_d = E_d^i e^{-K_d z}$$

we obtain

$$K_d = -\frac{1}{z} \ln \frac{E_d}{E_d^i} \tag{4.5}$$

where E_d is the total downward irradiance. If we replace the irradiances in Eq. (4.5) by the irradiances at two different depths, we get

$$K_d(z_i) = -\frac{1}{z_{i+1} - z_i} \ln \frac{E_d(z_{i+1})}{E_d(z_i)}.$$

The reflectance is $R = E_u/E_d$ according to Eq. (1.17). The results for K_d and R are shown in fig. 4.12 for zenith angles of $\theta_0 = 0°$ and $\theta_0 = 80°$. We see that when $\theta_0 = 0°$ there is only a slight difference between the case with a plane sea surface (the solid line) and the case with a rough sea surface (the triangles). On the other hand the difference caused by the roughness of the sea surface is significant for the cases in which the zenith angle is 80° (the dashed curve and the squares).

Once we have calculated the diffuse attenuation coefficients K_d and K_E, it is easy to check if the results from the MC code satisfies Gershun's relationship $K_E E_{tot} = aE_0$, derived in section 1.1.3. This is plotted in fig. 4.13, where the solid line represents the left-hand side of the equation and the triangles represents the right-hand side. When light travels through a homogeneous medium, the diffuse attenuation coefficient depends on the single scattering albedo. This dependence is shown in fig. 4.14. As the single scattering albedo increases from 0 to 1, K_d/a increases from $(\cos\theta_t)^{-1}$, where θ_t is the angle of refraction into the ocean. How much K_d/a increases depends on the scattering function used in the medium. This is the rewritten Gershun's law (Eq. (1.27)).

The next tests for the MC code involve a more complex system. Thus, the next three examples contain both Rayleigh scattering and HG scattering, and the irradiances both in the atmosphere and ocean are plotted against the optical depth in the same figure. In all the three cases the height of the atmosphere is 50 km and the depth of the ocean is 2,000 m. In fig. 4.15 the irradiances are

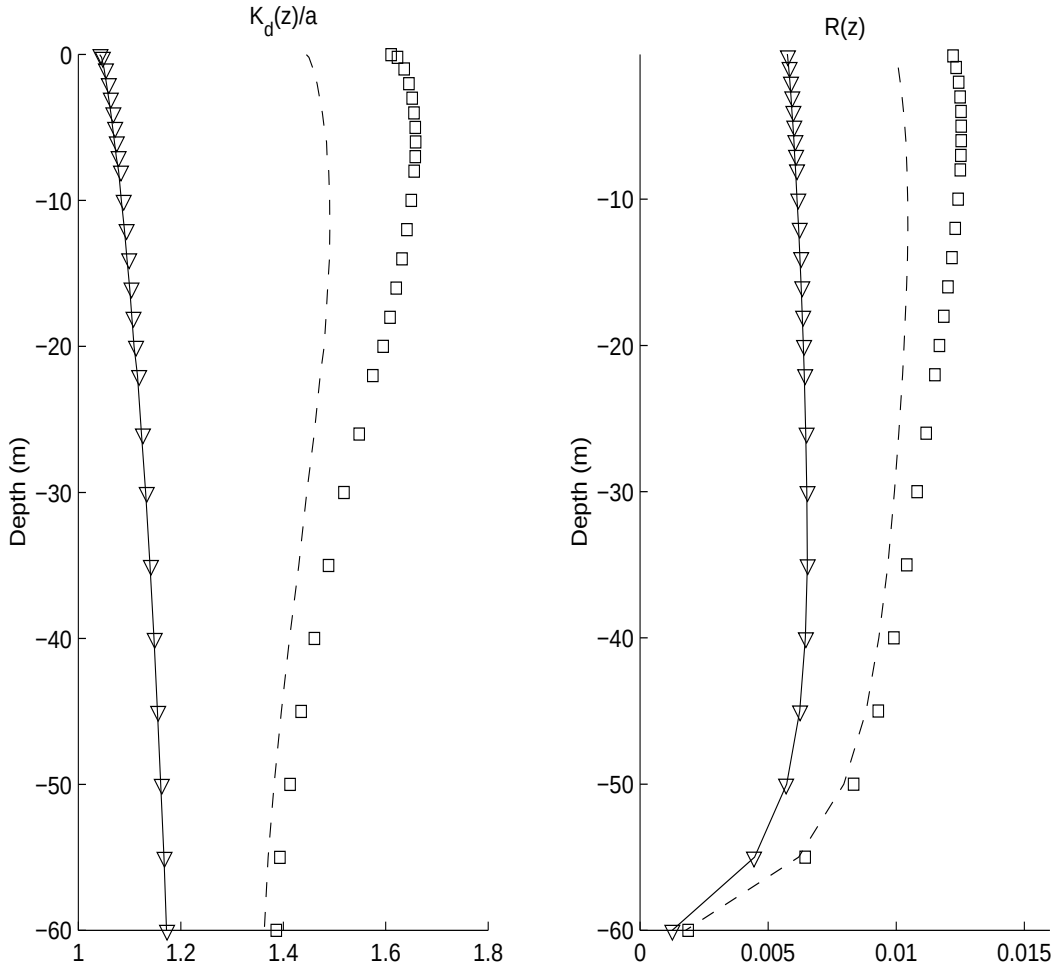

Figure 4.12: The apparent optical properties $K_d(z)$ and $R(z)$ for four cases. The solar zenith angle is $\theta = 0°$ for the the solid line and the triangles, and it is $\theta = 80°$ for the dashed line and the squares. The ocean surface was plane for the solid line and dashed line, but was rough for the triangles and the squares.

plotted from the TOA to a depth of 230 m, which corresponds to an optical depth varying from $\tau = 0$ to $\tau \approx$ -5.58. In the atmosphere both Rayleigh scattering on molecules and HG scattering on aerosols are included. The ocean is assumed to consist of pure water, hence, only Rayleigh scattering occurs. From fig. 4.16 we see that the disagreement between the MC and DISORT codes is, with only one exception, within 1% everywhere. The exception is at the TOA where there is a considerable disagreement for the downward diffuse irradiance due to different boundary conditions in the MC and DISORT codes. Thus, this error should be neglected. Note that the value of the downward diffuse irradiance should be zero at the TOA. In the next case, (fig. 4.17) fifteen layers of first-year ice are included

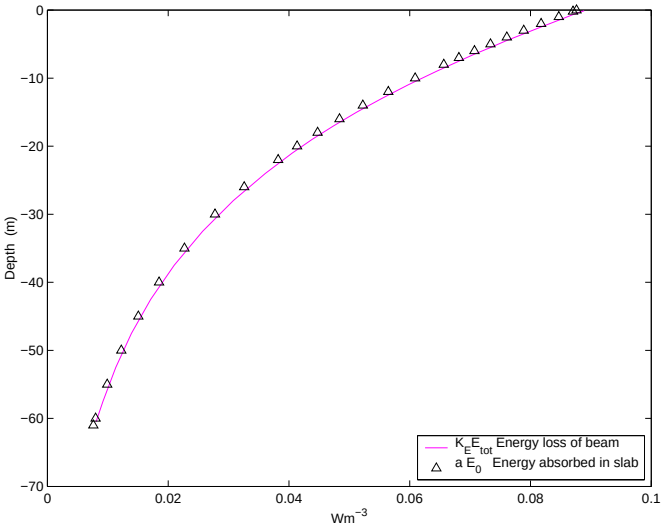

Figure 4.13: The results from the MC code satisfy Gershun's relationship Eq. (1.26) at all depths in the ocean. The line is the left hand side of the equation while the triangles are the right hand side.

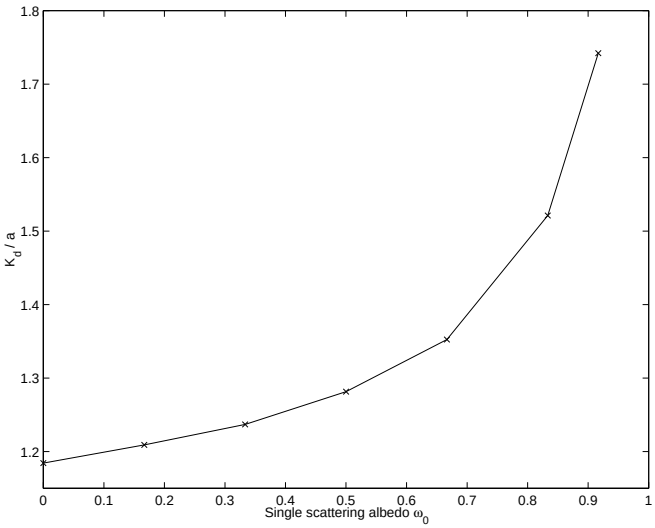

Figure 4.14: Relation between the downward diffuse attenuation coefficient K_d and the single scattering albedo ω_0. The zenith angle in the atmosphere is $\theta_0 = 45°$, the corresponding angle of refraction in the ocean is from Snell's law $\theta_t \approx 32.4°$. Note that for the case in which $\omega_0 = 0$ we should expect to find $K_d/a = (\cos\theta_t)^{-1} \approx 1.18$ (Eq. (1.27)). The graph shows that this result is obtained from the MC model.

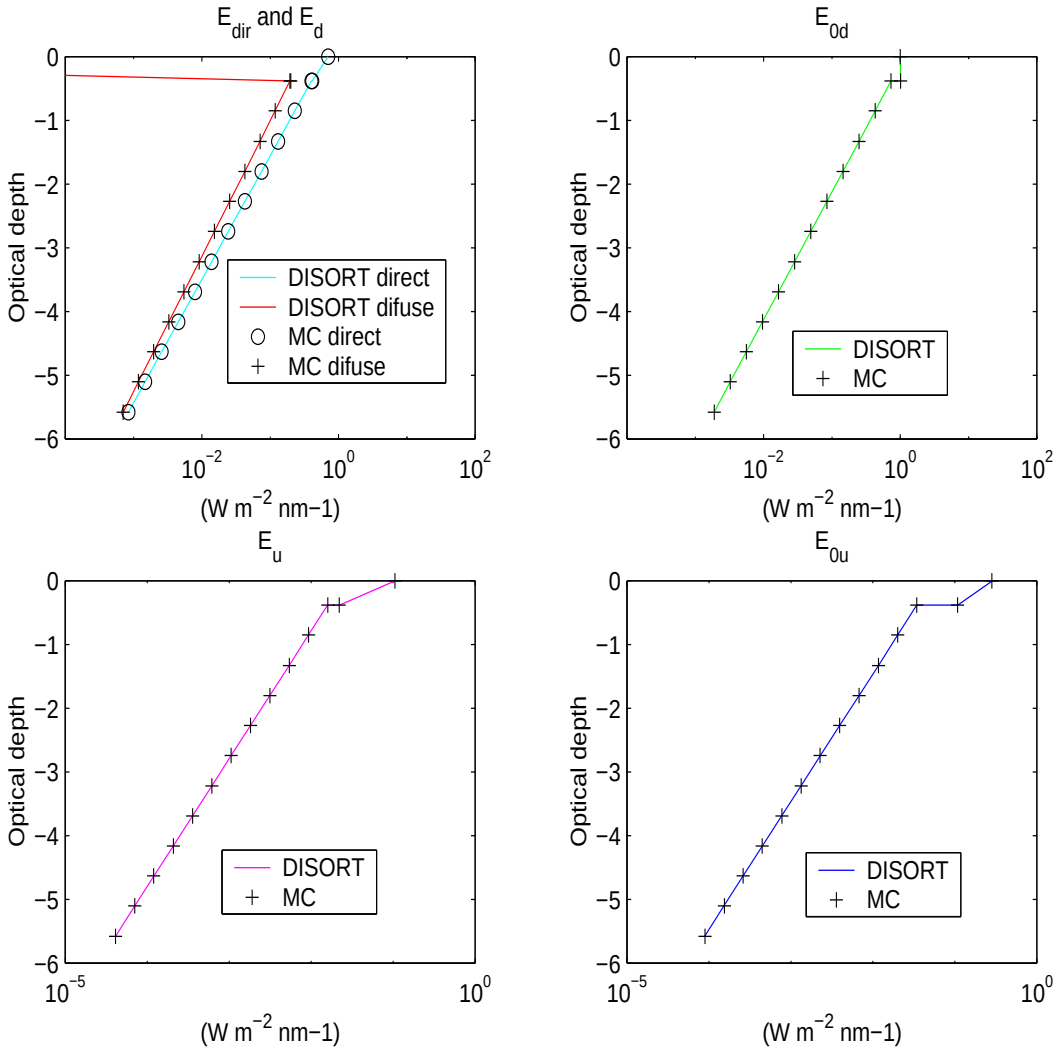

Figure 4.15: Irradiances in the atmosphere and in the ocean plotted against optical depth for an atmosphere-ocean system. The model includes Rayleigh scattering from molecules and HG scattering from aerosols in the atmosphere, as well as Rayleigh scattering from water particles in the ocean.

in the model. The ice is located between 0 m and -1 m in the ocean. Except for the ice layer this case is similar to the previous one. The vertical range of the plots is again from a height of 50 km to a depth of -230 m, but since the ice has a very high scattering coefficient, varying in the range $b \sim 60\ m^{-1} - 800\ m^{-1}$, the optical depth of the atmosphere-ice-ocean system becomes ~350. In the ice there is only HG scattering from brine pockets and air bubbles. The disagreement between the MC and DISORT codes is plotted in fig. 4.18 and is less than 15% everywhere except for the direct beam. The large error for the direct beam is due

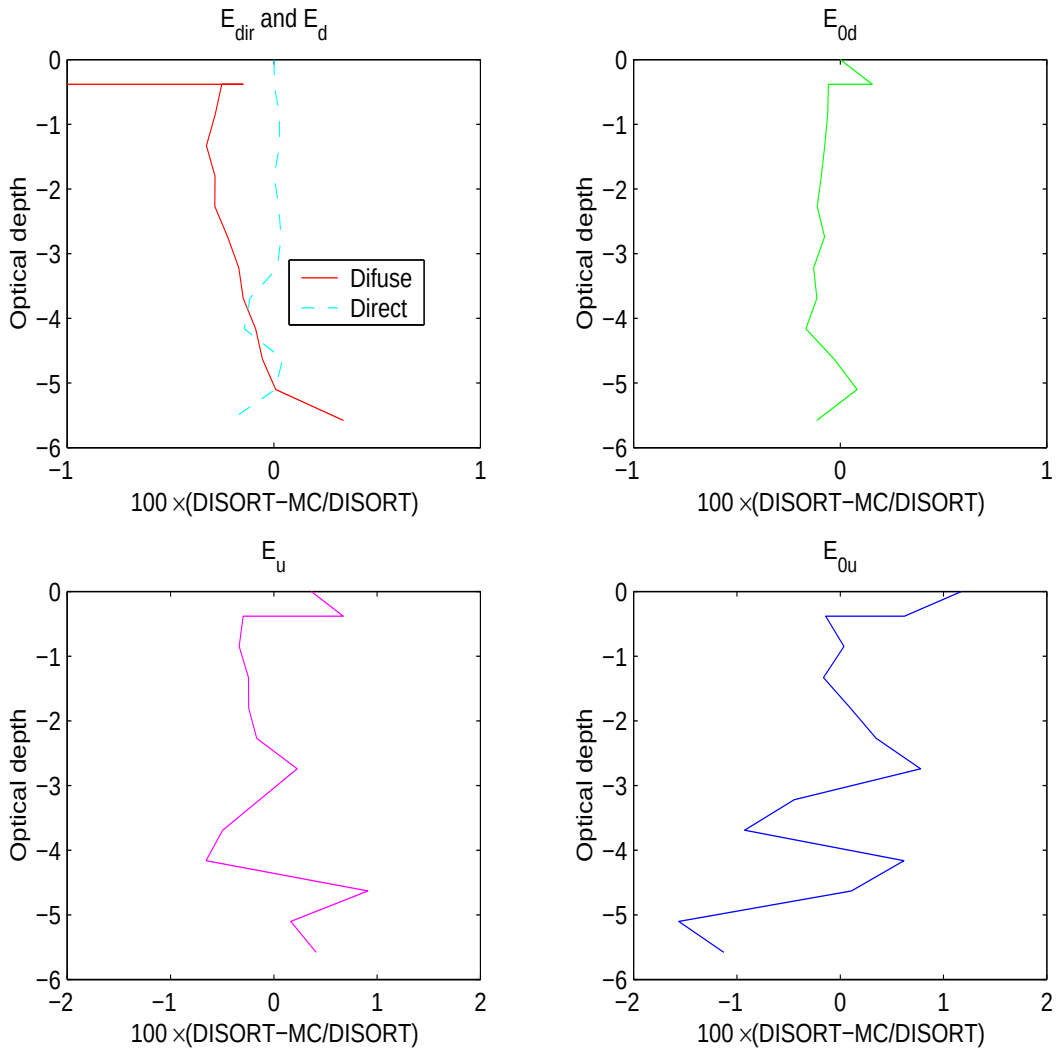

Figure 4.16: Disagreement between the MC and DISORT simulations in fig. 4.15.

to the huge attenuation coefficient c in the ice which causes total extinction of the direct beam in the MC code when the number of generated photons is finite. Thus, we should not worry about this error. Even though the scattering coefficient b is very large in the sea ice, the absorption coefficient is of the same order of magnitude as for sea water. Hence the single scattering albedo is extremely large for sea ice, i. e. $\omega_0 > 0.999$. This makes the system more complex and explains why the disagreement is larger for the case which includes sea ice. Similarly Table. 4.1 confirms that the disagreement increases when the single scattering albedo becomes close to one. The HG scattering in the sea ice is dominated by forward scattering, which means that the asymmetry factor g is close to one. That indicates that a limited number of phase moments could be responsible for

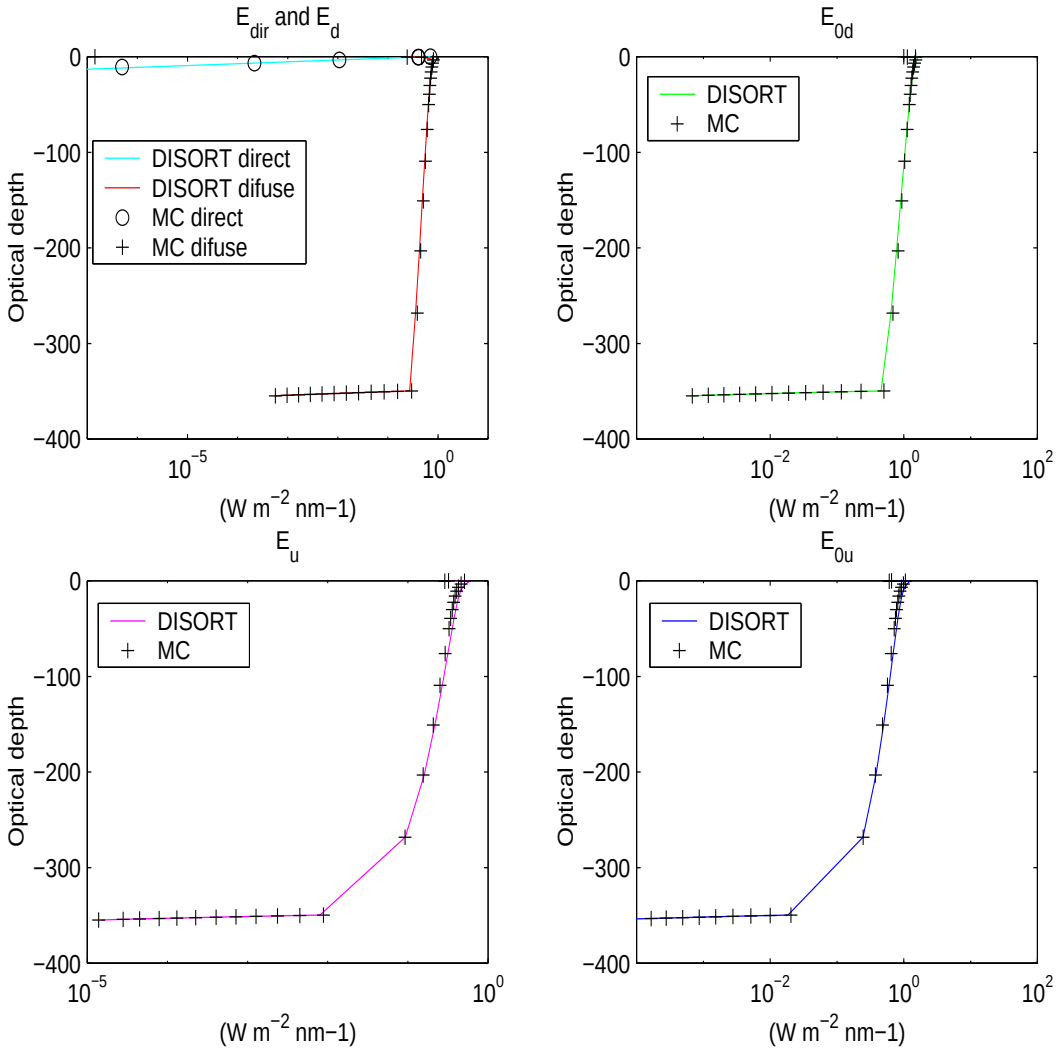

Figure 4.17: Irradiances in the atmosphere and in the ocean plotted against optical depth for an atmosphere-ice-ocean system. The model includes Rayleigh scattering from molecules and HG scattering from aerosols in the atmosphere, HG scattering in the ice layer, and Rayleigh scattering from water particles in the ocean.

some of the disagreement in the this case.

In the third case the ice is removed, but the upper layers of the ocean is assumed to contain a concentration of chlorophyll. Thus, there is both Rayleigh scattering and HG scattering in the atmosphere and also both Rayleigh scattering and HG scattering in the upper layers of the ocean down to an optical depth of $\tau \approx 3.6$. Beneath this depth there is only Rayleigh scattering on molecules in the ocean. In fig. 4.19 the irradiance is plotted form 50 km above the ocean down to

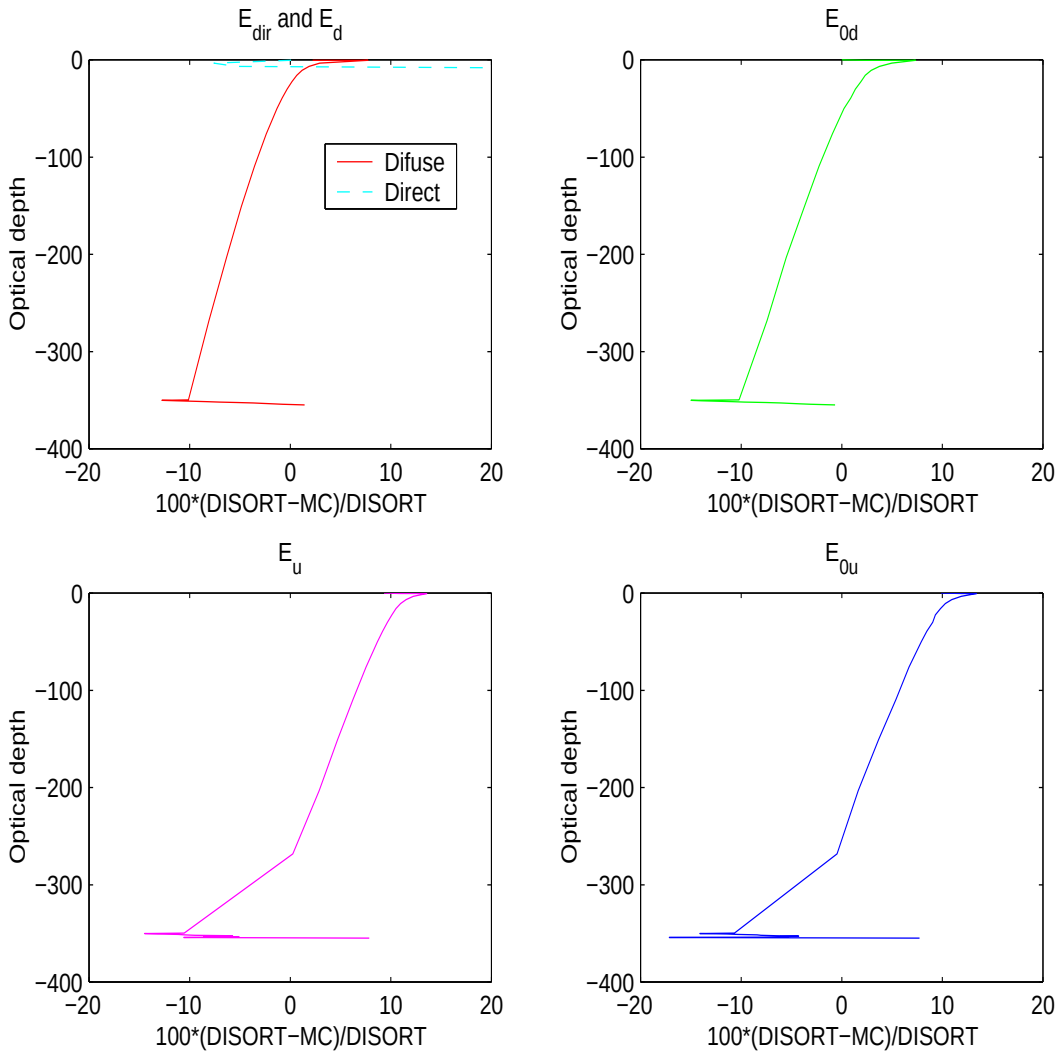

Figure 4.18: Disagreement between the MC and DISORT codes simulations in fig. 4.17.

a depth of 46 m ($\tau \approx -4.5$). From fig. 4.20 we can see that the local disagreement between the DISORT and MC codes is still within 1%.

4.3 3D atmosphere ocean system

In the previous examples we obtained the results for cases in which there is a 1D stratification of an atmosphere-sea ice-ocean system. As mentioned previously the advantage of the MC code is that it also can handle cases in which there is a 3D variation of the optical properties. One problem we meet when we separate

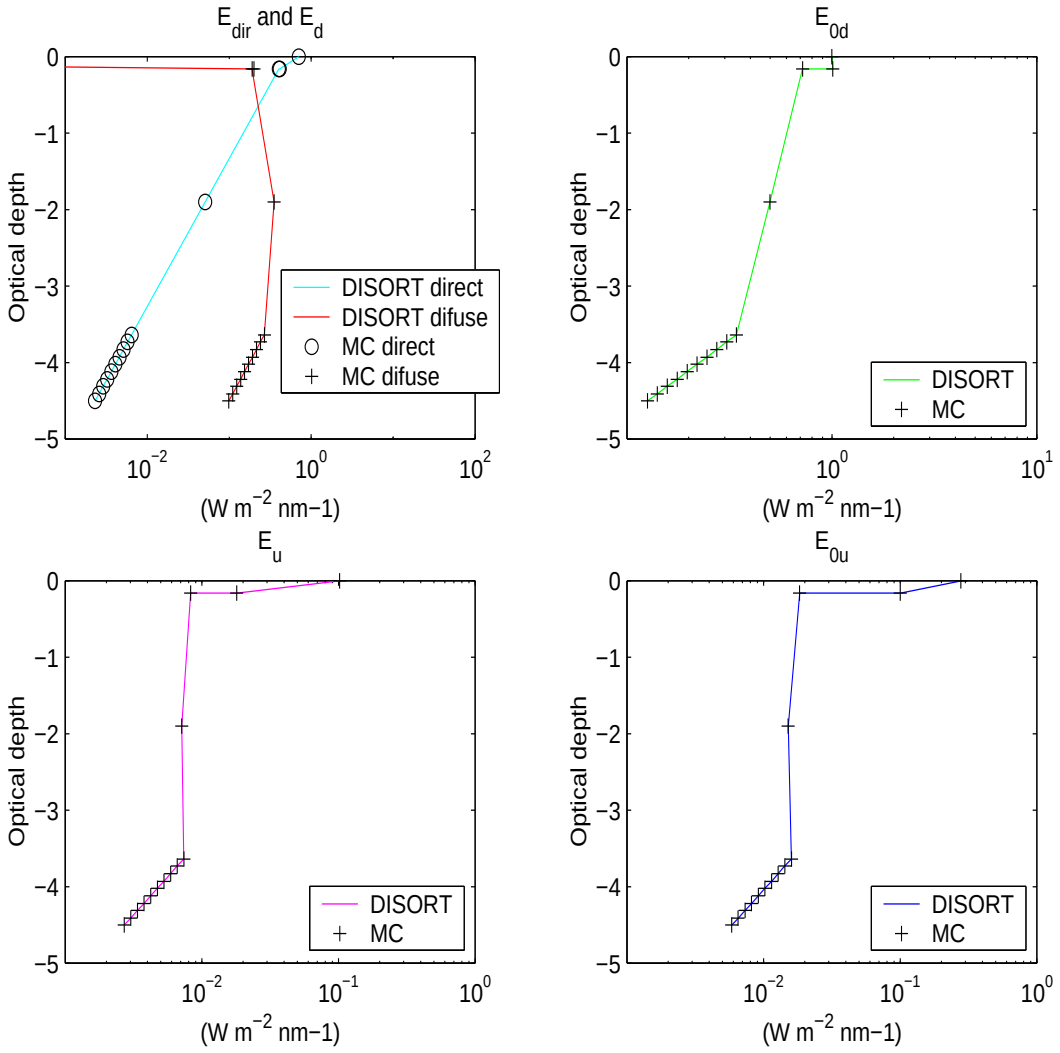

Figure 4.19: Irradiances in the atmosphere and in the ocean plotted against optical depth for an atmosphere-ocean system. The model includes Rayleigh scattering from molecules and HG scattering from aerosols in the atmosphere, as well as Rayleigh scattering from the water particles in the ocean. In addition to the Rayleigh scattering in the ocean there is also included HG scattering from chlorophyll in the first three ocean layers only.

the atmosphere-ocean system into cells as shown in fig. 3.1, is that the optical thickness of the ocean is much greater than the optical thickness of the atmosphere. This problem have we solved by multiply the absorption and scattering coefficients in the atmosphere by 1000 and also by dividing the altitude by the same number. The optical thickness in the atmosphere is then not too far from the optical thickness in the ocean.

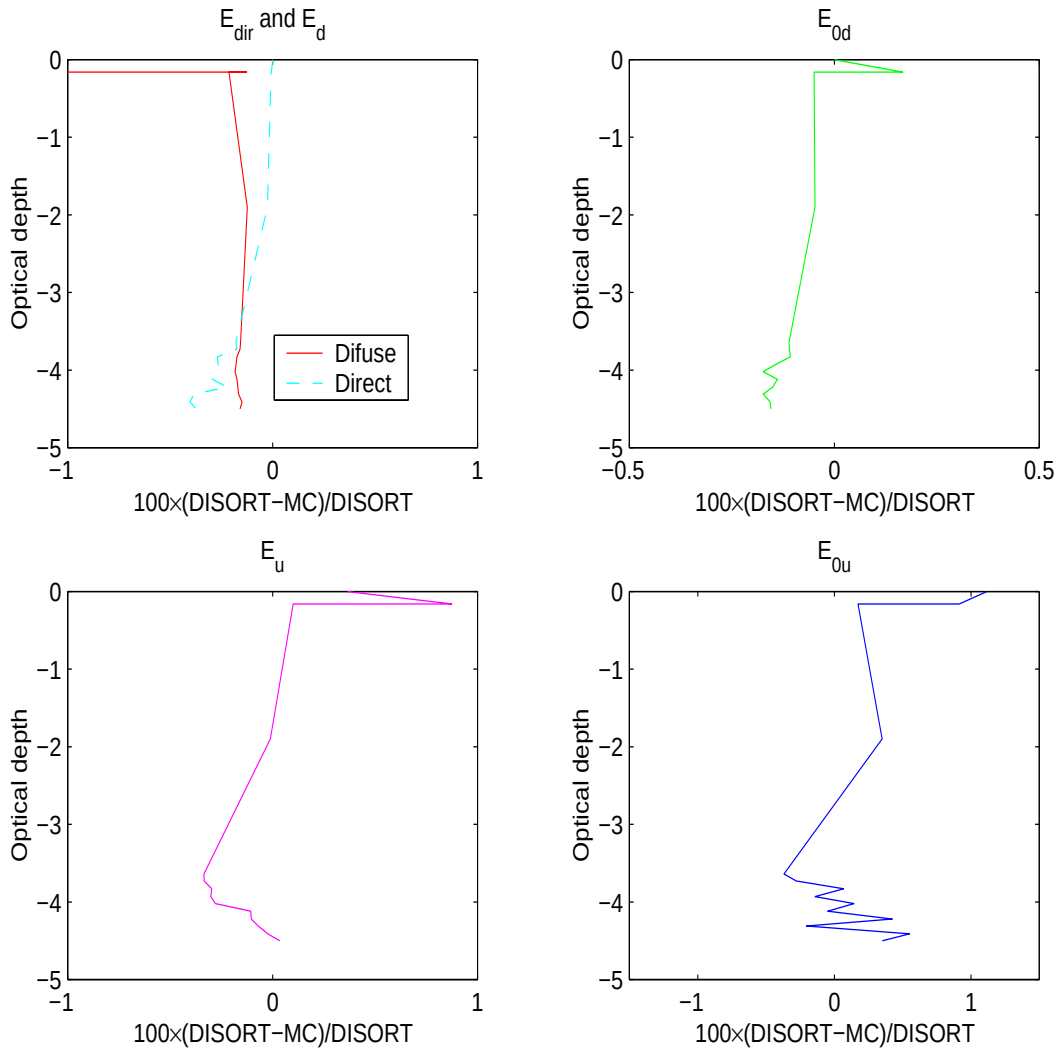

Figure 4.20: Disagreement between the MC and DISORT codes in simulations in fig. 4.19.

4.3.1 Ocean partly covered with ice

In this section we will examine the situation in which the ocean is partly covered by a layer of ice. In fig. 4.21 the geometry for this case is illustrated. On the left hand side of the ice edge the model is similar to the one used in fig. 4.15 and on the right hand side of the ice edge the model is similar to the one used in fig. 4.17. For the incident light we still use a zenith angle of $\theta_0 = 45°$, and we let the azimuth angle vary from 0° to 180° in steps of 45°. The irradiances are plotted in figs. 4.22 - 4.27, where the ice layer is situated on the positive horizontal axis (the x-axis) with a depth ranging from 0 m to -1 m. The azimuth

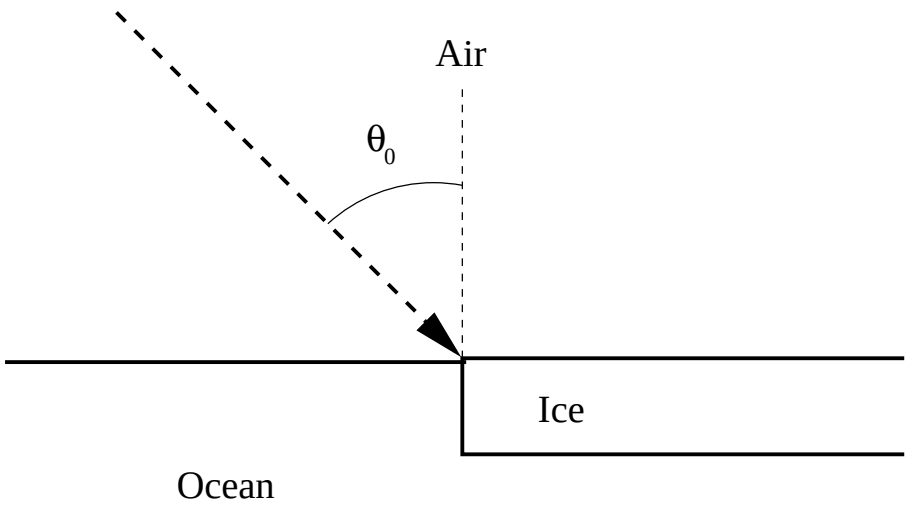

Figure 4.21: Geometry for the case in which the ocean is partly covered by ice.

angle is measured from the x-axis. Note that the unit in the atmosphere is km while it is m in the ocean. In fig. 4.22 there is a plane sea surface, while there are included surface waves from a wind speed of 6 ms^{-1} in figs. 4.23 - 4.27. Hence, the surface facets represent the only difference between fig. 4.22 and fig. 4.23. For the direct irradiance we can see how the ice edge causes a shadow. There is a slight difference between figs. 4.22 and 4.23 where the only difference is the presence of surface facets, but the structure of the contour lines is not considerable changed.

For all azimuth angles we can see that the combination of the direct beam and the diffuse light causes a focusing spot in the ocean. The center of this spot is located at a depth between 0.5 m and 1.0 m and next to the ice edge in the horizontal direction. The high scattering coefficient b in the ice causes the light to be widely spread out of the ice, also in the horizontal direction into the ocean. Therefore, the diffuse light creates a light field that is added to the direct solar beam. Hence, the irradiance at this focus is higher than it would be in the absence of the ice edge. Note that neither the direct beam nor the diffuse light creates this spot alone. It is the sum of these two light fields that creates it. In fig. 4.28 (which is identical to the lower left panel in fig. 4.23) we have zoomed in on this phenomenon. The radiation from the sea ice is spread out and causes a focusing spot. The effect can be observed down to a depth of approximately 5-6 m and also 3-4 m away from the ice in the horizontal direction (not shown in fig. 4.28).

The scattered light from the sea ice gives the largest contribution to the irradiance in the upward direction. Both the direct reflected beam and the diffuse light from the ocean are considerably less than the diffuse light from the ice.

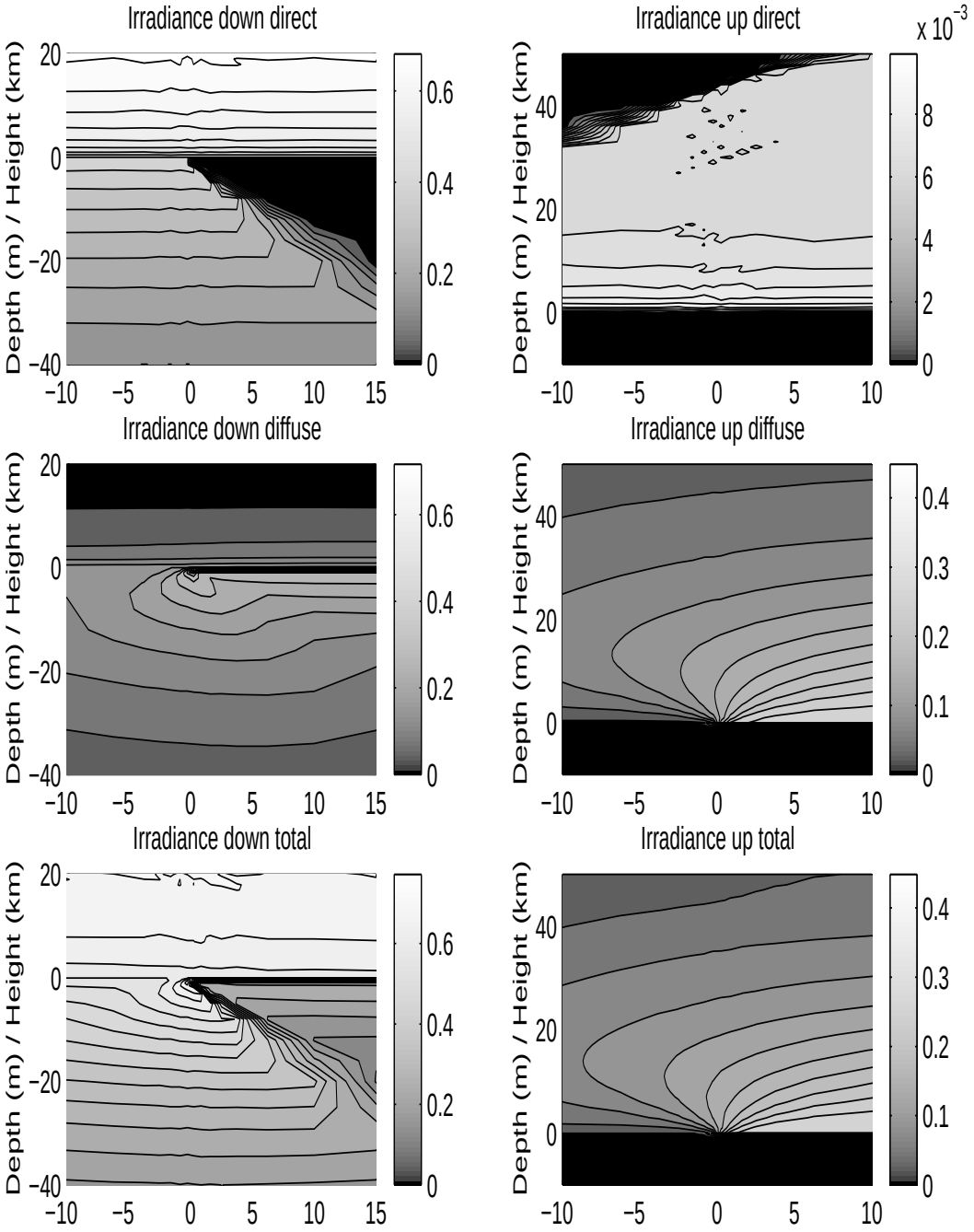

Figure 4.22: MC simulation of irradiances for the case in which the ocean is partly covered by ice. There are no surface facets on the ocean in this case. The azimuth angle is 0° and the zenith angle is 45°.

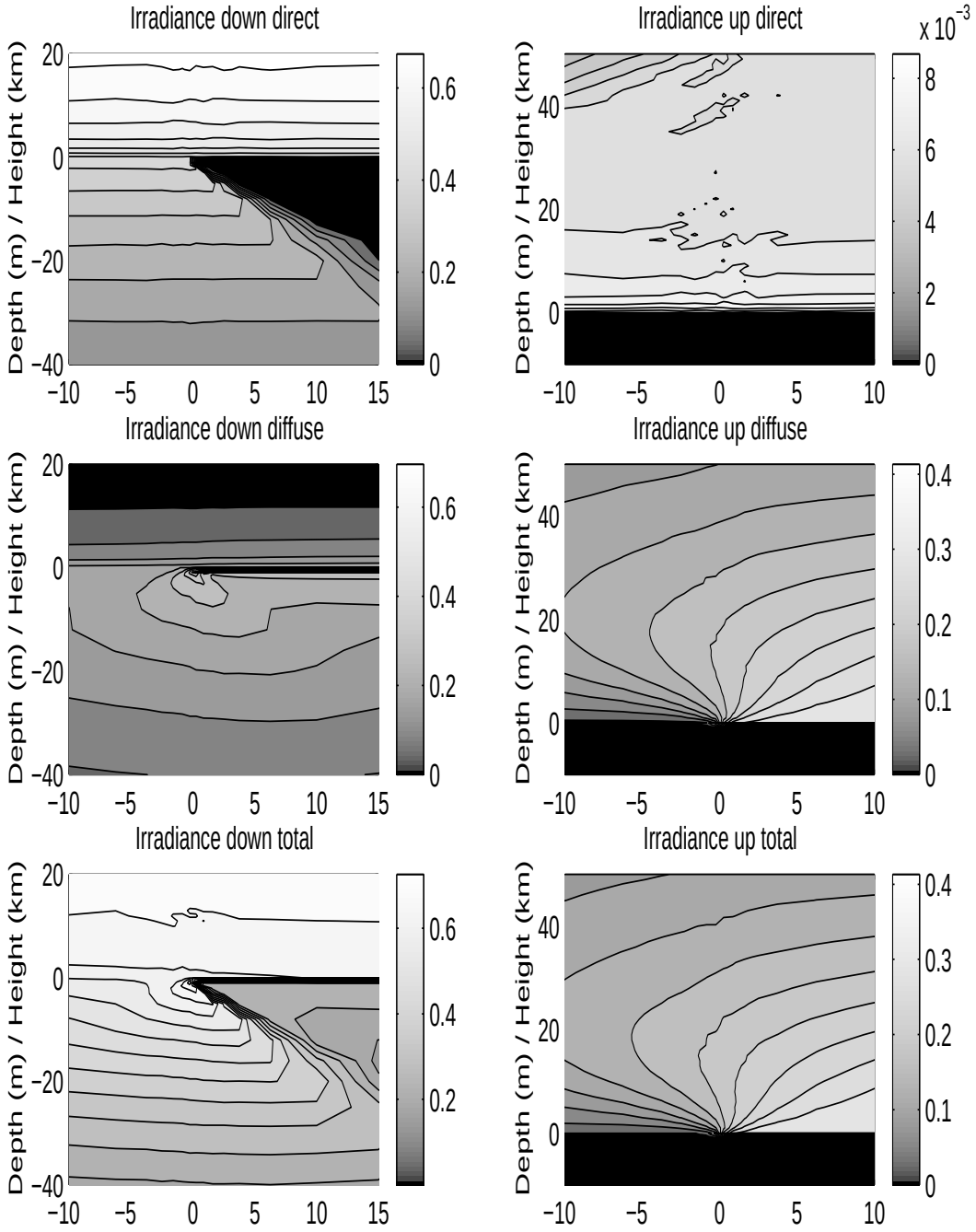

Figure 4.23: MC simulations of irradiances for the case in which the ocean is partly covered by ice. A surface roughness of the ocean due to a wind speed of 6 ms^{-1} is included. The azimuth angle is 0° and the zenith angle is 45°.

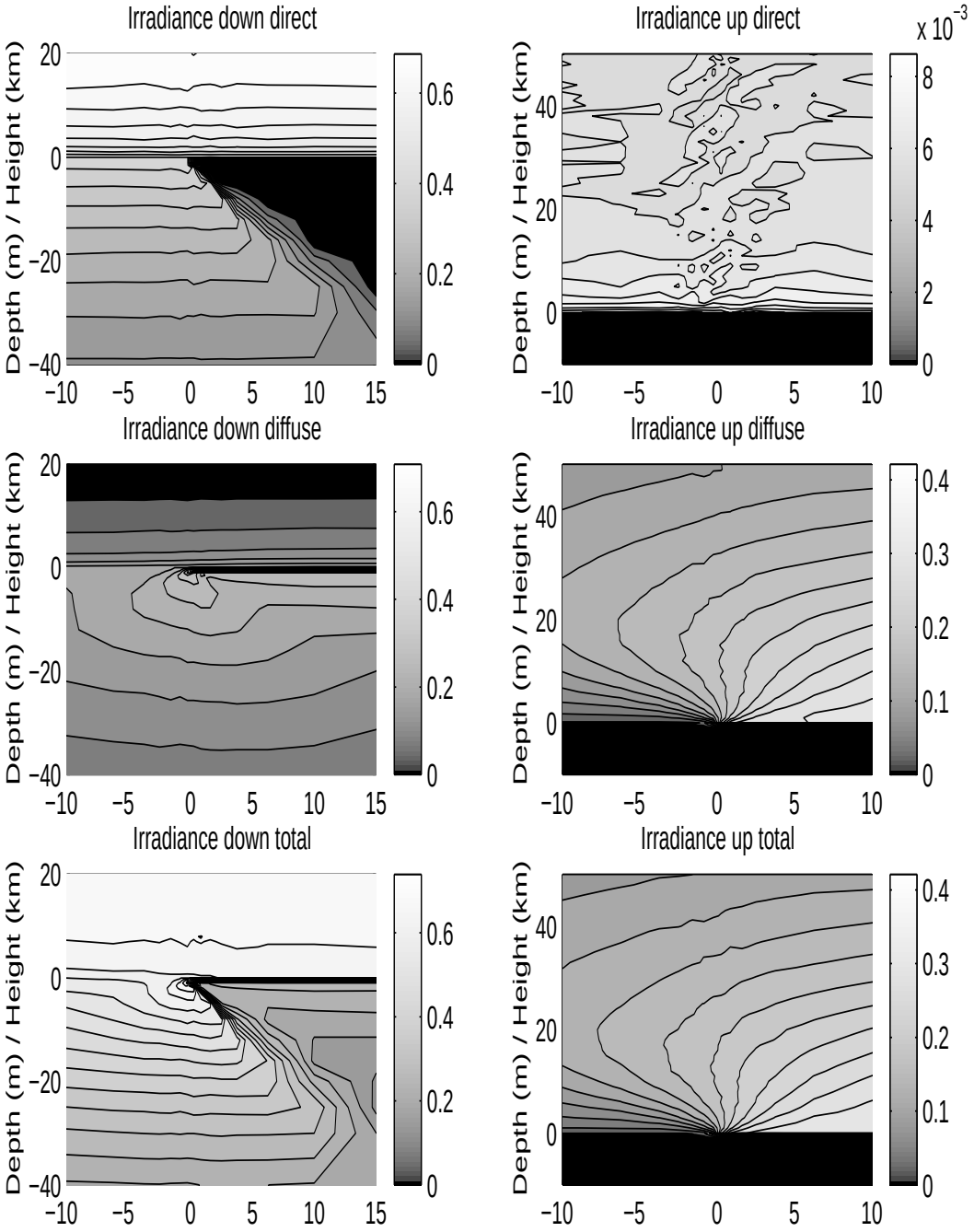

Figure 4.24: MC simulations of irradiances for the case in which the ocean is partly covered by ice. A surface roughness of the ocean due to a wind speed of 6 ms^{-1} is included. The azimuth angle is 45° and the zenith angle is 45°.

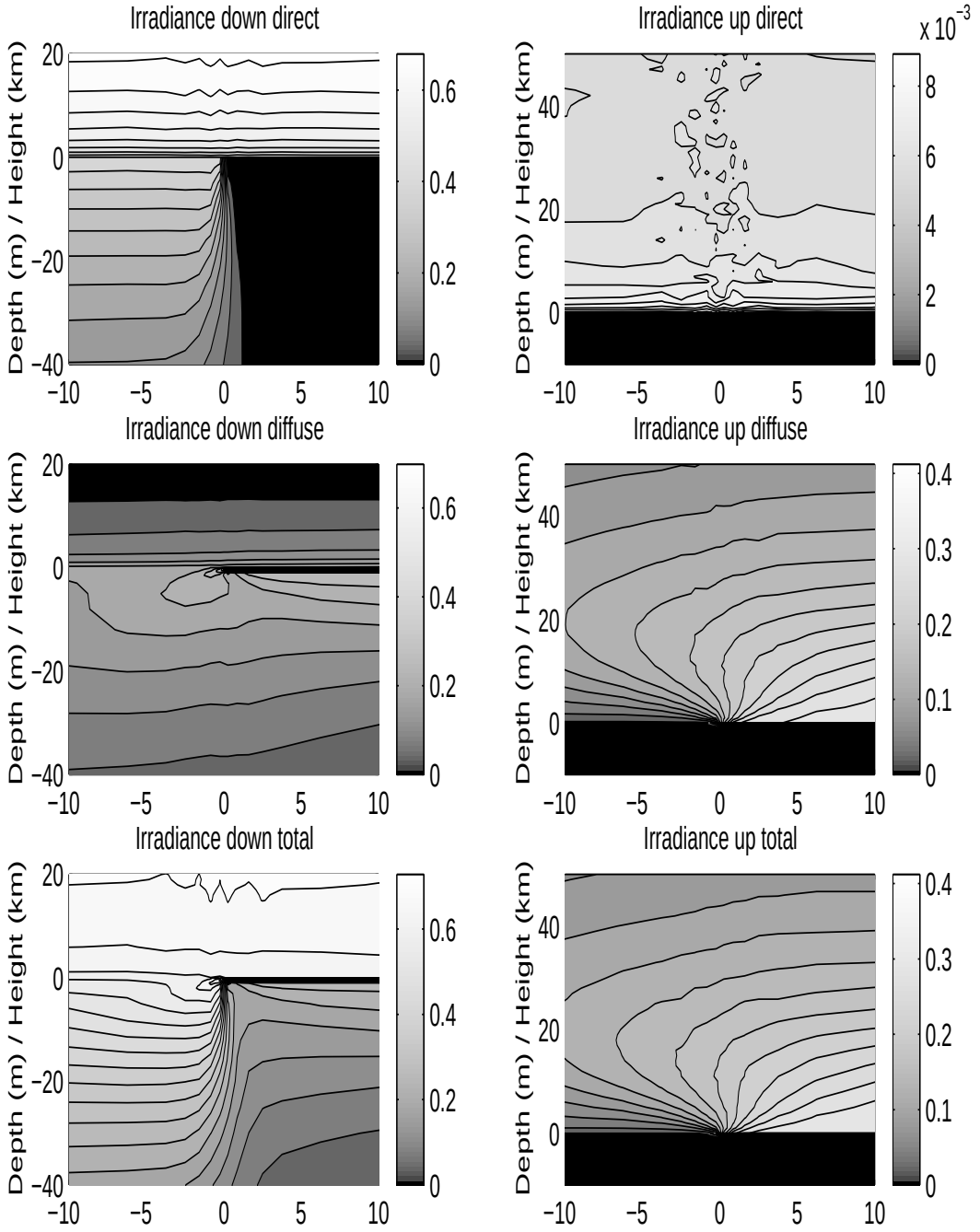

Figure 4.25: MC simulations of irradiances for the case in which the ocean is partly covered by ice. A surface roughness of the ocean due to a wind speed of 6 ms^{-1} is included. The azimuth angle is 90° and the zenith angle is 45°.

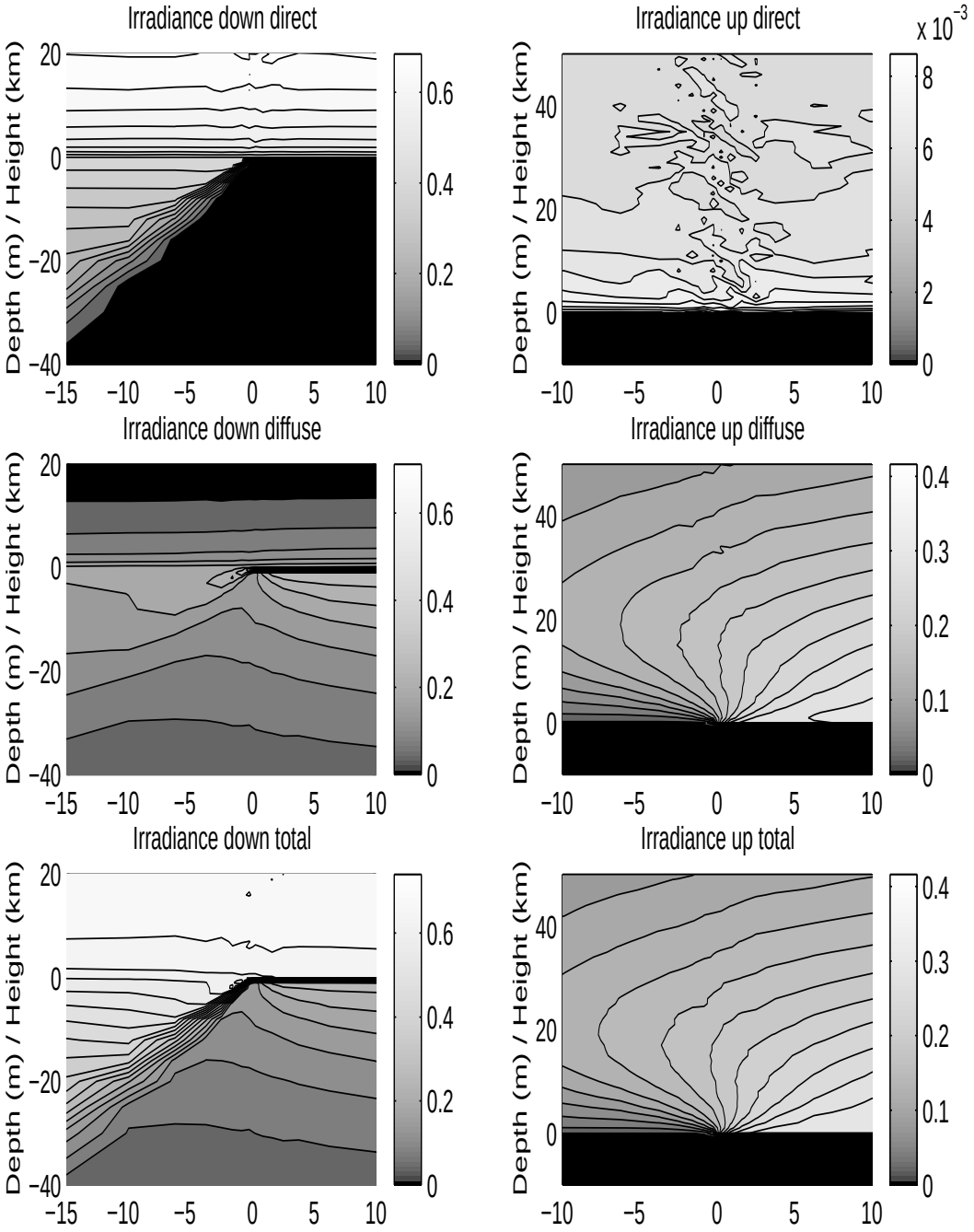

Figure 4.26: MC simulations of irradiances for the case in which the ocean is partly covered by ice. A surface roughness of the ocean due to a wind speed of 6 ms^{-1} is included. The azimuth angle is 135° and the zenith angle is 45°.

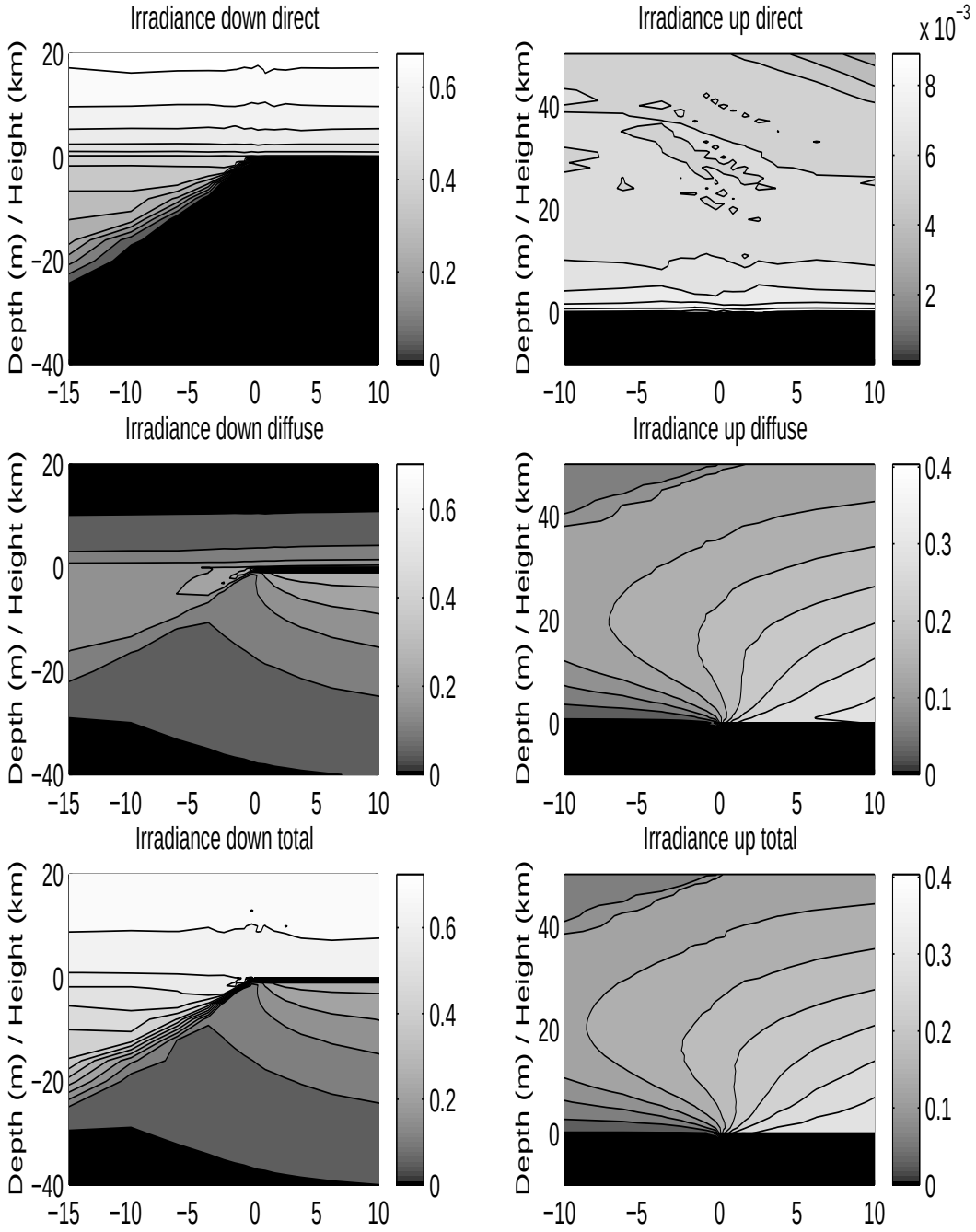

Figure 4.27: MC simulations of irradiances for the case in which the ocean is partly covered by ice. A surface roughness of the ocean due to a wind speed of 6 ms^{-1} is included. The azimuth angle is 180° and the zenith angle is 45°.

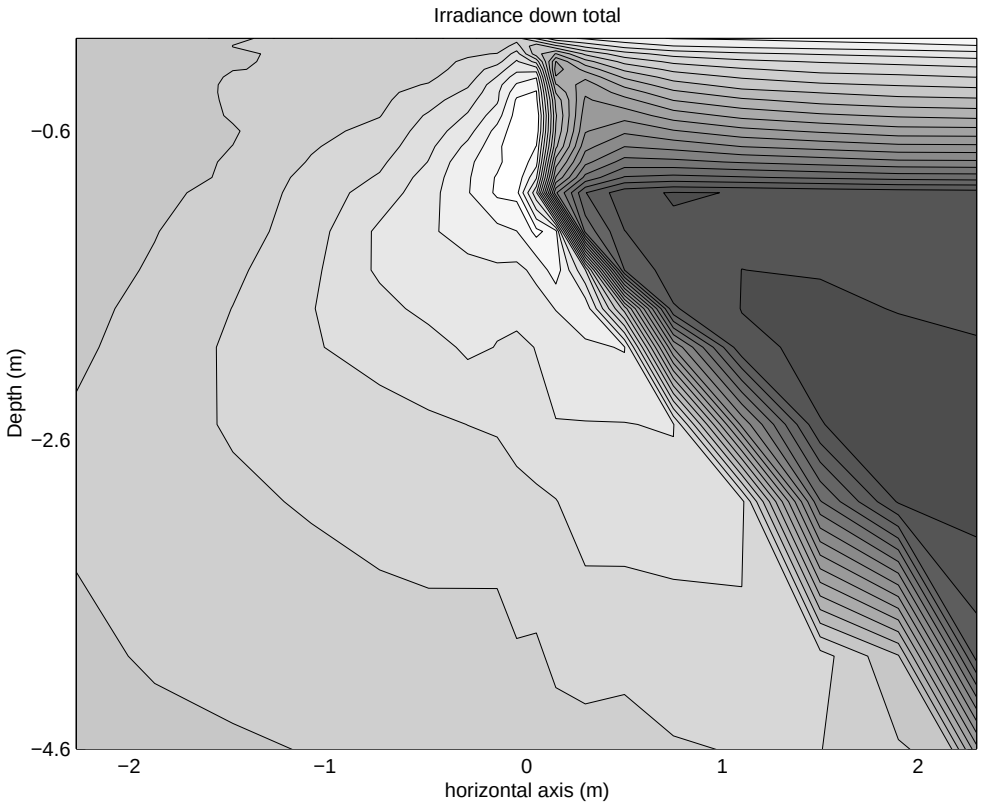

Figure 4.28: MC simulations of the total downward irradiance for the case in which the ocean is partly covered by ice. A surface roughness of the ocean due to a wind speed of 6 ms^{-1} is included. The azimuth angle is 0° and the zenith angle is 45°.

4.3.2 Shadow from a boat

Since our 3D MC code allows us to consider a complicated topography we now do simulations for a situation in which an opaque object is put on the sea surface. The object reaches 2 m both above and below the water surface. It is 2 m wide (along the x-axis) and 8 m long (along the y-axis out of the plane of the figure). The purpose of putting this object on the water is to create a shadowing effect that is similar to the one we could expect if there was a boat lying on the water. It is interesting to examine what influence a boat has on the distribution of the irradiance in the ocean below. When the irradiance is measured in the ocean, it is usually done from a boat and even if the measurements are done on the side of the boat that faces the sun, the presence of the boat might have a significant effect on the measured irradiance. In fig. 4.29 the irradiance is plotted in the water around the boat. As expected the direct light is only changed in the shadow zone of the boat. The diffuse light, however, also gives less irradiance in

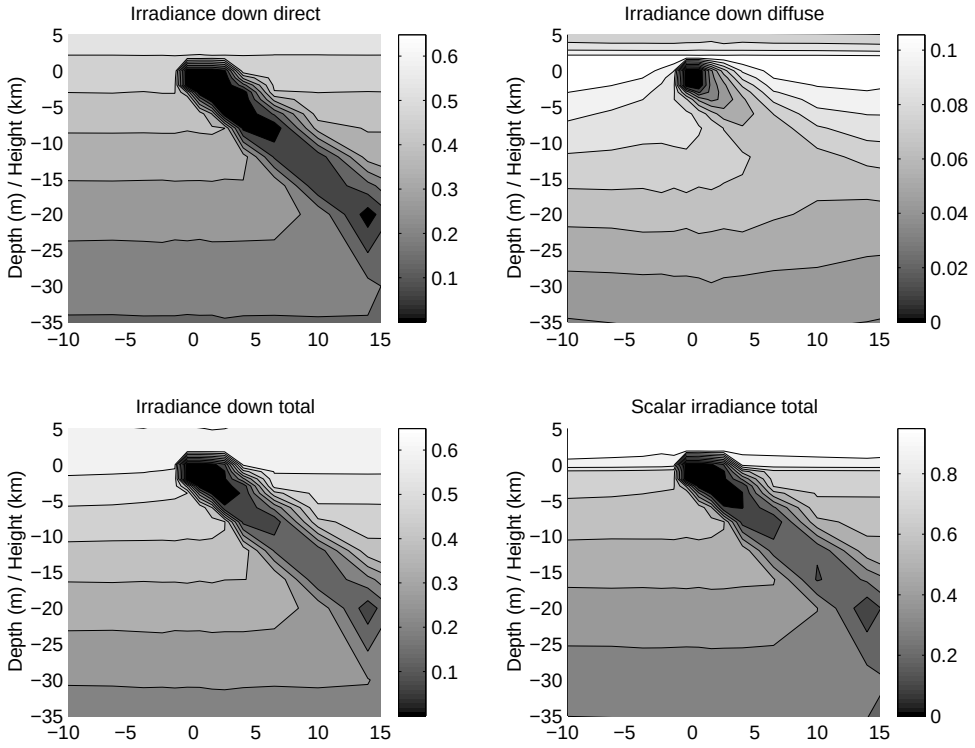

Figure 4.29: MC simulations of irradiances for the case in which a boat causes a shadow in the water. Surface roughness on the ocean due to a wind speed of 6 ms^{-1} is included. The zenith angle is 45° and the azimuth angle is 0°.

the area next to the geometrical shadow zone. This effect is significant also on the sun facing side of the boat. In this example the direct light is approximately five times larger than the diffuse contribution. Hence, the influence of the diffuse light on the total scalar irradiance is small but measurable. One should keep in mind that how much a boat will reduce the irradiance in an area surrounding it depends both on the magnitude of the scattering coefficient b and the scattering function β. In this case the IOPs were taken to be the same as in fig. 4.15 where there is only Rayleigh scattering in the ocean. In examples with other scattering functions and scattering coefficients we should not expect the same results.

4.3.3 Error sources

As mentioned previously, the 3D MC model separate the the ocean and the atmosphere into cells and the code calculates the irradiances on the bottom surface of each cell. When we calculate the irradiance in one cell, we assume that the photons are uniformly distributed over the bottom so we can use the approximation

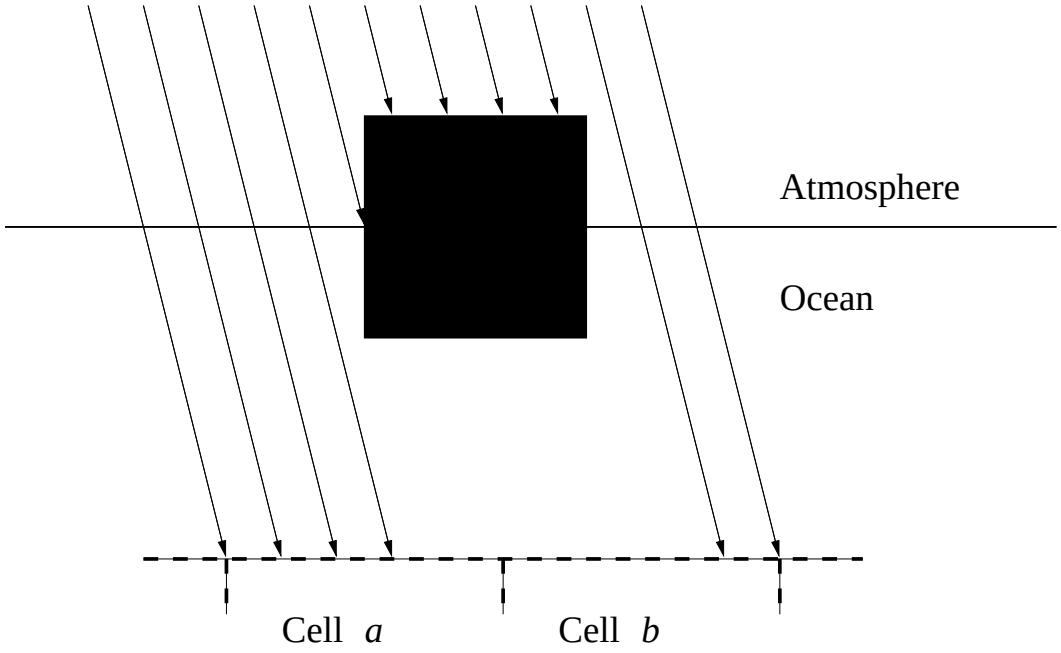

Figure 4.30: Illustration of a 3D MC case with a boat lying on the water surface. The irradiance on the detecting surfaces cell a and cell b is not uniform which we assume it is.

(Eq. (1.6))

$$E = \frac{d\Phi}{dA} \approx \frac{\Phi}{A}.$$

For cases in which we have an ocean that is partly covered with ice or there is a boat lying on the water, we should be careful when using this approximation. As shown in fig. 4.30, the photon distribution may be far from uniform on a detecting surface in a 3D case, and hence the final outcome may contain errors. The source of this problem is that the size of the detector is too big compared to the size of the included 3D topography. This problem could easily be solved by making the size of each cell smaller. However, this improvement of the resolution has the vital drawback that the code will require a considerably larger CPU time. The user of the program should therefore consider necessary requirements both with respect to precision and CPU time, and adapt the program accordingly.

When we take a closer look at the boat case in fig. 4.29, we discover the assumption in Eq. (1.6) is not satisfied valid. In the printed figures from MatLab we can see an "island" with reduced irradiance compared to the surrounding area. This "island" is located approximately at a depth of 20 m in the geometrical shadow zone. Especially for the direct irradiance it is obvious that it should not first decrease and then increase afterwards. The reason why this "island" appears is that the cells are too wide along the x axis, and in this case the size grows as

we get far from the boat along the x axis.

As mentioned previously, fig. 4.28 is the same case as the lower left panel in fig. 4.23. The only difference is that in the latter figure the cell grids have a finer resolution centered around the ice edge. This provides us with more detailed contour lines in the actual area. In this case the areas of the cells are even smaller around 0 m on the x-axis. When the areas are smaller fewer photons get detected on these areas. Hence the calculated irradiance is more sensitive to the distribution of photons among the areas. This causes the contour lines to be less smooth on the small areas than they are elsewhere. To achieve smooth lines everywhere we could employ more photons in the model. Then there would be enough photons to get an even distribution among all areas. However, this case took approximately 48 hours to estimate on a supercomputer, so to this point we accept the result as they are.

Chapter 5

Conclusions

5.1 1D code

The MC code and the DISORT code are two different ways of approaching the problem of radiative transfer in a vertically stratified coupled atmosphere-sea ice-ocean system with no variations of the optical properties in the horizontal direction. For this one-dimensional case we have obtained an almost perfect agreement between these two methods when the boundary conditions are the same. Hence, we can conclude that both methods provide a correct solution to the problem.

For cases only include a coupled atmosphere-ocean system, these two models show a local deviation of less than 2% almost everywhere in the system for all irradiances. If an ice layer with extremely high single scattering albedo and optical thickness is included the local deviation between the models grows to approximately 10%. Hence, the large scattering coefficient in the ice makes the case more complex for these simulations and the results become less precise.

One advantage of the DISORT method is that it is very efficient and that it does not require a super computer to solve a multilayer problem. The MC code on the other hand puts very heavy demands on the CPU time. The MC code should nevertheless not be considered to be superfluous. Even for a 1D case the MC code has unique features that give useful contributions to the issue of radiative transfer in the atmosphere and in the ocean. The MC code may handle surface facets on the ocean due to wind, which is more realistic than a plane ocean surface. We have also seen how this information can contribute to improve the DISORT code. The simplest improvement was obtained by modifying the index of refraction in the ocean (Eq. (4.2)). This method improves the results from the DISORT code. But we should note the exception the direct upward irradiance in the atmosphere where the absolute difference between the DISORT code and the MC code becomes even larger when this modification is used. This is a very simple method to compensate for the lack of surface waves in the DISORT routine. Only one input value needs to be changed, the rest of the code is not

affected by this modification.

Another interesting way of accounting for surface waves is to calculate the average direction of the refraction angle $\overline{\theta}_t$ and the reflection angle $\overline{\theta}_r$ for the solar beam on refraction and reflection by a rough sea surface. By using MC simulations, we can calculate these directions as functions of the wind speed and the zenith angle. In Eq. (4.3) and Eq. (4.4) we have predicted approximate functions describing $\overline{\theta}_t$ and $\overline{\theta}_r$. To put these modifications into the DISORT code requires a number of changes in the source code. In this thesis we have not performed these changes. It is left as future work in the topic of radiative transfer in the atmosphere and the ocean.

The surface facets on the ocean due to wind have a significant influence on the apparent optical properties AOPs. The results from the MC code have shown how the diffuse attenuation coefficient K_d and the reflectance R change when surface waves are included. Also, we have seen that the surface waves have a more significant effect on the AOPs when the zenith angle θ_0 is large.

Since the MC code and the DISORT code have different advantages and drawbacks they should be considered to be complementary models rather than competing models in the issue of 1D radiative transport in the atmosphere and in the ocean.

5.2 3D code

The one-dimensional 1D MC code can easily be expand to handle three-dimensional 3D topography. The only changes required are that the system is separated into boxes rather than layers and that the routines for detecting the photons applies to each of these boxes. The path of a traveling photon are calculated in exactly the same way as before. Hence, the 3D model gives the same result as the 1D model as long as the IOPs do not have any horizontal variations. The 3D model, however, requires considerable more CPU time than the 1D model. There are two reasons why the CPU time grows for the 3D model. One is that more calculations are required for every single photon when it travels through the system. The other is that a higher number of photons need to be used in the 3D model to obtain acceptable accuracy.

We have also seen how the size of the cells might cause errors in the plotted contour diagrams. When the cells are too big compared to the topography, the approximation in Eq. (1.6) is no longer valid and there might appear errors in the results. Keeping this weakness of the 3D model in mind, we should be very careful when we choose the dimensions of the cells. However, the 3D model will provide very accurate results as long as the cells are small compared to distances over which the local topography does not vary significantly.

When cells of very different sizes are present in the model, one should note that calculations of the irradiance in the smallest cells will require a higher number of

photons employed to converge compared to the larger cells.

In the study of the ocean partly covered by ice we can see how the diffuse irradiance from the ice layer and the direct irradiance in the ocean creates a focusing spot in the ocean right next to the ice.

5.3 Future work

Our MC model for radiative transport in the coupled atmosphere-snow-sea ice-ocean system (CASSIO) has been found to give reasonably good results compared to the DISORT routine. Still we have only touched the surface of the topic of radiative transfer in the atmosphere and ocean and our model could be improved in many different ways. Here we shall mention some of them.

- Calculation of radiance both for 1D and 3D cases.
- Improve the DISORT routine with the results from the CASSIO-MC routine.
- Make the cells of different shapes to simulate topography and let the detectors be tilted.
- Investigate effects of reflection from bottom or shore.
- Let a Gaussian beam enter the atmosphere.
- Investigate polarization effects.
- Compare model with experimental results.

The first point of this list should not be too difficult to include. To detect the radiance we need both the direction and the position of the photons. In the 1D model as well as in the 3D model both position and direction of every photon is given in three dimensions. Hence, all one needs to do is to expand the code with some new subroutines for detecting the photons.

In this thesis we have suggested a way of improving the DISORT code to include the effect from surface facets (Eq. (4.3) and Eq. (4.4)). To be able to draw any final conclusions of how this will improve the results from the DISORT code, we have to perform the changes in the DISORT code and compare the new results with the results from the MC code where surface facets are included.

The separation of the media into cells allows the IOPs to vary in all directions. However, so far the walls of the cells are all lying in the horizontal xy-plane, in the vertical xz-plane, or in the vertical yz-plane. The model would be more flexible if we managed to improve it to handle oblique cell walls as well. This improvment will also make it possible to let the detectors for the irradiances be tilted. The

Monte Carlo approach developed by Miesch et al. [29] handles an Earth surface that is not horizontal.

In the simulations performed in this thesis, we have assumed a black bottom. The model should also be tested for cases with some reflection from the bottom and cases with combination of sea surface and shore ground, e. g. the irradiance in a fjord area.

In the 3D case it would also be interesting to see how a Gaussian beam would travel and be spread in a coupled atmosphere ocean system.

When light interacts with the sea surface or undergoes by Rayleigh scattering, the polarization of the light is of great importance. The MC code does not handle any polarization effects. It could be useful to investigate how polarization effect influence the results.

Finally, but may be most important, we mention that the model should be tested against experimental results. The results so far only confirm that there is good agreement between two theoretical models. Our goal is to develop a model that predicts the results we expect to measure in the nature.

Appendix A

The Monte Carlo program

A.1 Explanation of the Monte Carlo structure

Here follows a detailed explanation of the structure of the Monte Carlo program (fig. A.1) discussed in section 3.1

Set initial boundary: Set the initial position and direction of the photon before it starts its journey through the coupled atmosphere-sea ice-ocean system.

Set IOPs and path length: The program sets the IOPs for the cell in which the photon is traveling. The properties to be set are the absorption coefficient a, the scattering coefficient b, the Henyey-Greenstein asymmetry factor g, the Rayleigh polarization factor p, the ratio of Rayleigh scattering events to all scattering events η, and medium n.

New position: An incident photon has a given position (x,y,z) and a given direction of propagation $(\Omega_x, \Omega_y, \Omega_z)$. Next we must decide how far the photon will travel before an extinction event occurs. The path length pl in the given direction is found from Eq. (3.3), i. e.

$$pl = -\frac{\ln \rho}{c_n}$$

where $c_n = a_n + b_n$ is the extinction coefficient for the nth cell, and ρ is a random number. Now the new position and cell for the photon is evaluated from its start position, propagation direction, and path length.

New cell? The position of the photon may now be within the same cell as previously or it may be within a new cell.

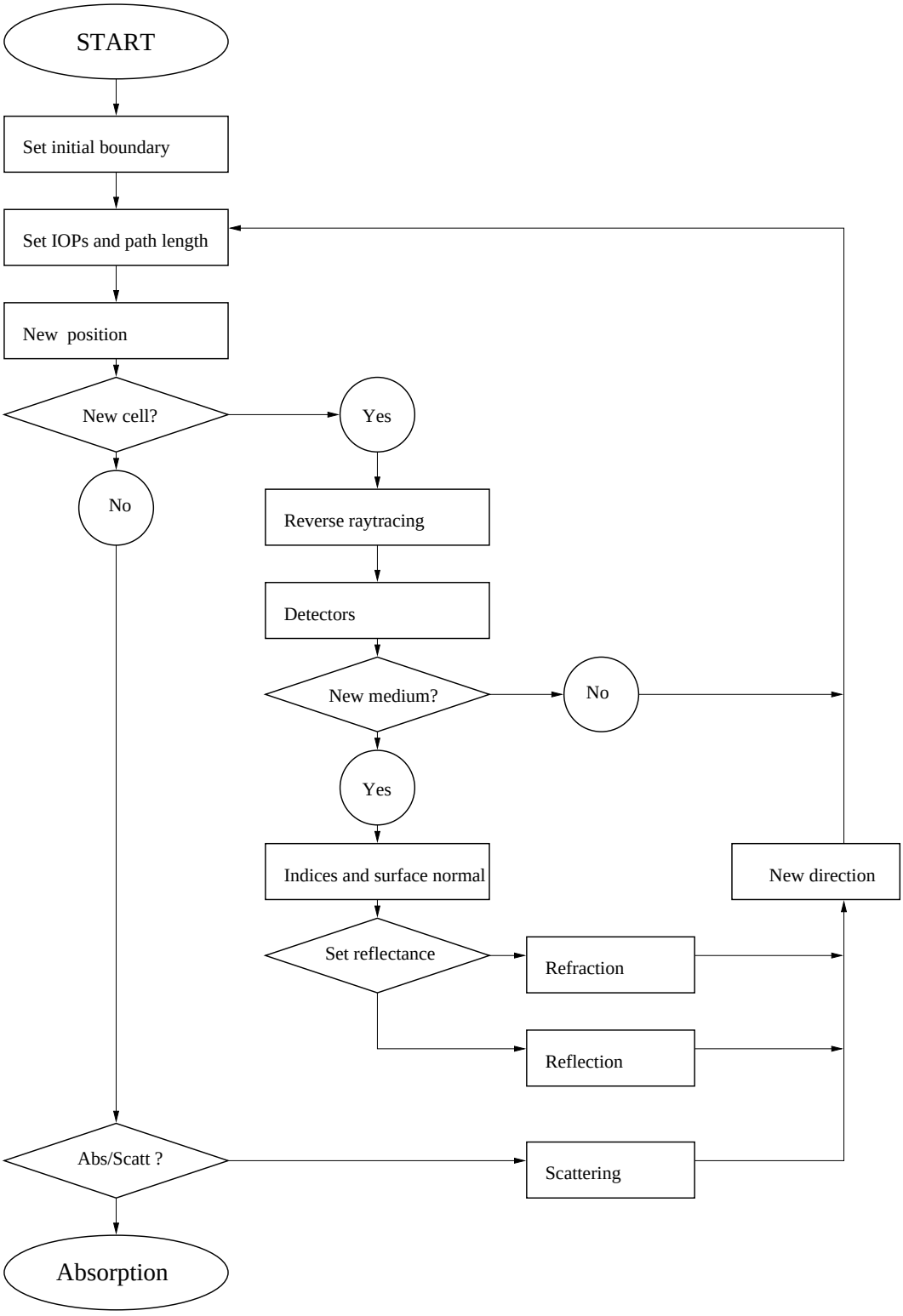

Figure A.1: Flow chart of the Monte Carlo program. Every photon follows this path from it is launched at the top of the atmosphere until it is absorbed somewhere in the atmosphere or in the ocean or it escapes back to space.

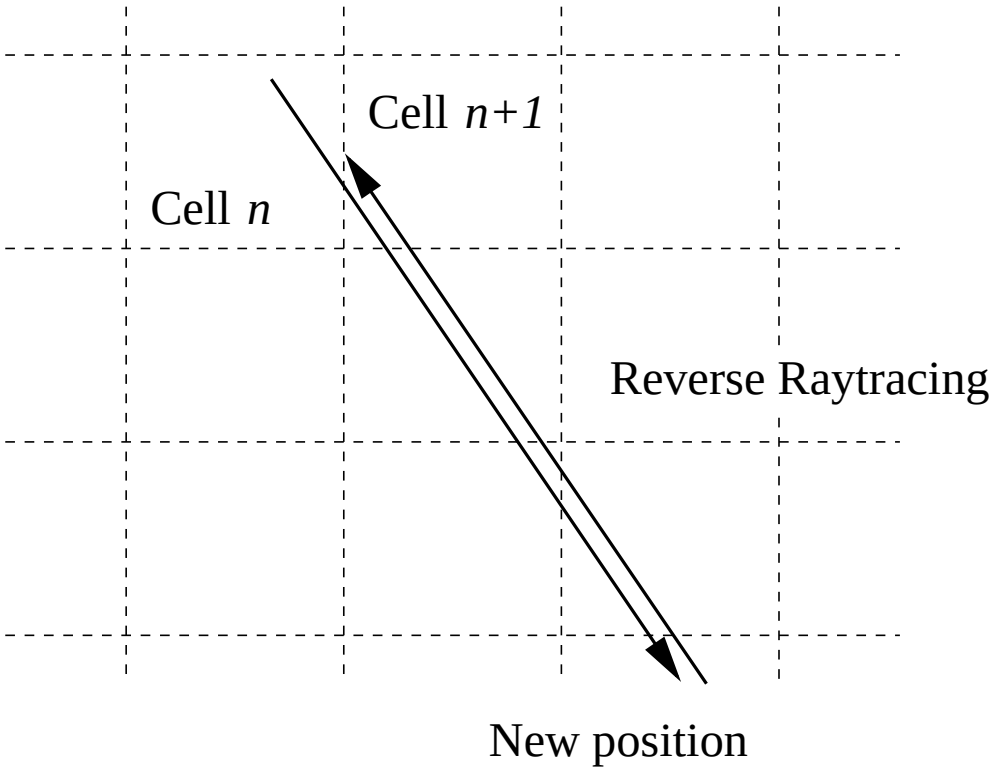

Figure A.2: A photon travels to a new position and is traced back to the point where it left the previous cell.

Reverse raytracing: When the photon has entered a new cell it is necessary to trace it back to the point where it left the previous cell. Now we must find out of how much of the initial path length *pl* that is "consumed". We call the remaining part *plrest*. Since the photon now enters a new medium, we have to change the remaining path length according to

$$pl = plrest \frac{c_n}{c_{n+1}}$$

when we continue through next cell (fig. A.2).

Detectors: If the photon leaves one cell through the bottom surface or the top surface, a detector routine will count the photon for calculation of the irradiance.

New medium? Check if the new cell has the same index of refraction as the previous one.

Indices and surface normal If not, a routine evaluates the indices of refraction for the two media and the normal vector of the intersection surface.

Set reflectance: Find the probability for the photon to be reflected and transmitted.

Refraction: The photon is refracted into the new medium.

Reflection: The photon is reflected back to the old medium.

Abs/Scatt The single scattering albedo ω_0 decides whether the photon is absorbed or scattered.

Scattering: The photon is scattered.

New direction: After the photon has been refracted, reflected or scattered it will continue to propagate in a new direction.

Bibliography

[1] G. E. Thomas and K. Stamnes. *Radiative Transfer in the Atmosphere and Ocean.* Cambridge University Press, 1999.

[2] C. D. Mobley. *Light and Water.* Cambridge University Press, 1994.

[3] C. D. Mobley, B. Gentili, H. R. Gordon, Z. Jin, G. W. Kattawar, A. Morel, P. Reinersman, K. Stamnes, and R. H. Stavn. Comparison of numerical models for computing underwater light fields. *Appl. Opt.*, 32:7484–7504, 1993.

[4] R. W. Spinrad, K. L. Carder, and M. J. Perry. *Ocean Optics.* Oxford University Press and Clarendon Press, 1994.

[5] L. C. Henyey and J. L. Greenstein. Diffuse radiation in the galaxy. *Astrophys. J.*, 93:70–83, 1941.

[6] L. Rayleigh. *Phil.Mag*, 41:107–120,274–279,447–454, 1871.

[7] L. Rayleigh. *Proc. Roy. Soc*, 97,98:435–450,57–64, 1920.

[8] A. Morel and B. Gentili. Diffuse reflectance of oceanic waters: its dependence on sun angle as influenced by the molecular scattering contribution. *Appl. Opt.*, 30:4427–4437, 1991.

[9] G. Mie. "beiträge zur optik trüber medien speziell kollodialer metallösungen,". *Ann. Phys.*, 25:377–445, 1908.

[10] C. D. Mobley, G. F. Cota, T. C Grenfell, R. A. Maffione, W. S. Pegau, and D. K. Perovich. Modeling light propagation in sea ice. *IEEE Transaction on geoscience and remote sensing*, 36:1743–1749, 1998.

[11] D. K. Perovich, J. Longacre, D. G. Barber, R. A. Maffione, G. F. Cota, C. D. Mobley, A. J. Gow, R. G.Onstott, T. C. Grenfell, W. S. Pegau, M. Landry, and C. Roesler. Field observations of electromagnetic properties of first-year sea ice. *IEEE Transaction on geoscience and remote sensing*, 36:1705–1715, 1998.

[12] S. Gerland, J. G. Winther, J. B. Ørland, and B. V. Ivanov. Physical properties, spectral reflectance and thickness development of first year fast ice in kongsfjorden, svalbard. *Polar research*, 18:275–282, 1999.

[13] A. Morel. Optical properties of pure water and pure sea water. In N. G. Jerlov and E. S. Nielsen, editors, *Optical aspects of oceanography*, pages 1–24. Academic press, New York, 1974.

[14] A. Morel. Lecture notes, fys 266. Fysisk institutt, Universitetet i Bergen, 2001.

[15] Z. Jin and K. Stamnes. Radiative transfer in nonuniformly refracting layered media: atmosphere-ocean system. *Appl. Opt.*, 33:431–442, 1994.

[16] Ø. Frette, S. R. Erga, J. J. Stamnes, and K. Stamnes. Optical remote sensing of waters with vertical structure. *Appl. Opt.*, 40:1478–1487, 2001.

[17] W. H. Press, S. A. Teukolsky, W. T. Vetterling, and B. P. Flannery. *Numerical Recepies in C*. Cambridge University Press, 1992.

[18] J. J. Stamnes. Lecture notes fys 263, fysikalsk optikk. Fysisk institutt, Universitetet i Bergen, 1999.

[19] M. Born and E. Wolf. *Principles of Optics*. Cambridge University Press, 1980.

[20] T. Frøystein. Gamma-ray flow imaging. Master's thesis, Department of Physics, University of Bergen, 1992.

[21] Computational Science Education Project. Introduction to monte carlo methods. Published on world wide web: http://csep1.phy.ornl.gov/mc/mc.html.

[22] C. Cox and W. Munk. Measurement of the roughness of the sea surface from photographs of the sun's glitter. *Journal of the optical society of America*, 44:838–850, 1954.

[23] Z. Jin and J. J. Simpson. Bidirectional anisotropic reflectance of snow and sea ice in avhrr channel 1 and 2 spectral regions-part i: Theoretical analysis. *IEEE Transactions on geoscience and remote sensing*, 37:543–554, 1999.

[24] R. A. J. Groenhuis, H. A. Ferwerda, and J. J. Ten Bosch. Scattering and absorption of turbid materials determined from reflected measurements. *Appl. Opt.*, 22:2456–2462, 1983.

[25] J. K. Lotsberg. Experiments and field measurement in marine optics. Master's thesis, Department of Physics, University of Bergen, 2000.

[26] C. F. Gerald and P. O. Wheatly. *Applied Numerical Analysis*. Addison-Wesly Publishing Company, 1994.

[27] J. T. O. Kirk. *Light and Photosynthesis in Aquatic Ecosystems*. Cambridge University Press, 1994.

[28] H. C van de Hulst. *Multiple light scattering - Tables, Formulas and Applications*. Academic Press, 1980.

[29] C. Miesch, X. Briottet, Y. H. Kerr, and F. Cabot. Monte carlo approach for solving the radiative transfer equation over mountains and heterogeneous areas. *Appl. Opt.*, 38:7419–7430, 1999.